Instrument development and characterization of atmospheric aerosol physical properties through airborne measurement

Thesis by
Jian Wang

In Partial Fulfillment of the Requirements
for the Degree of
Doctor of Philosophy

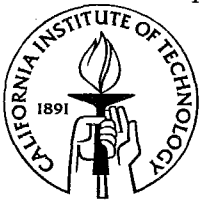

California Institute of Technology
Pasadena, California

2003

(Defended June 12, 2002)

Acknowledgements

It is with my deepest appreciation that I acknowledge both my advisors, John Seinfeld and Rick Flagan, for their research guidance, inspiration, and support over the years. I appreciate their faith in me and patience throughout my research. The true value of all I learned from John and Rick during my stay at Caltech goes far beyond what is presented here. I would also like to thank the two other members of my thesis committee, Prof. Yuk Yung and Prof. Paul Wennberg, for their interest in my thesis work.

Without the help and support I received from those within and outside the group, I never could have accomplished what I did. I'd like to express my appreciation to Don, Pat, Jim, Greg, and Denis for their help on my work and sacrificing their own research time to answer my numerous (some of them were quite stupid) questions. I am grateful to Tim, Jose, Brian, Roya, Tomtor, and David for helping me in the lab and making life in the lab and field enjoyable. I would also like to thank Thanos for helping me with ISORROPIA and computer software, and Bill and Julia for many valuable discussions on my research.

Since much of my research involved aircraft sampling, I am indebted to those at CIRPAS that helped make the field project both enjoyable and productive. Haf worked long and hard to ensure the staggering number of instruments were working and the scientific objectives were met. I am thankful for Nava, Reggi, and Dennis for their work to integrate my instrument and make sure flights went smoothly.

I am grateful to many members of technical staff within and outside Caltech. I would like to thank Tom Dunn for his help with electronics, Mike Roy, Marty Gould, and Mike Vondrus for their support on constructing the DMA system.

And finally, I would like to express my gratitude to my family, my parents, brother, and my lovely wife, Rong. Throughout my graduate study, Rong is always the one making sacrifices, whether it was commuting to USC every day, or working around

my crazy schedule when I was building and testing my instrument. It is her love and support that make this work possible, and I'll always be grateful for that.

Instrument development and characterization of atmospheric aerosol physical properties through airborne measurement

by

Jian Wang

In Partial Fulfillment of the
Requirements for the Degree of
Doctor of Philosophy

Abstract

Atmospheric aerosol has significant impact on climate. It influences radiative transfer by scattering and absorbing sunlight and by changing the microphysical structure, lifetime, and amount of the clouds. Due to its short lifetime, the spatial and temporal distributions of tropospheric aerosol are highly inhomogeneous. Aircraft have proven to be an effective platform in characterizing the atmospheric aerosol. To maximize the potential and to reduce the artifacts associated with aircraft sampling, both improvements in existing instruments and developments of new instruments are required.

To increase the speed of submicron aerosol size distribution measurements, a mixing condensation nucleus counter (MCNC) has been developed. By carefully designing the mixing chamber and condenser, the response time of the MCNC was significantly reduced. Our experiments demonstrate that a differential mobility analyzer (DMA) coupled with the developed MCNC can measure complete aerosol size distributions in as little as 2 seconds.

The effects of bends and elbows on the diffusional losses of particle in nanome-

ter range were studied. The results show that the effect of bends and elbows on particle diffusion loss is significant, and for Reynolds number smaller than 250, the enhancement of diffusion losses due to bends and elbows is sensitive to both the relative orientations of the bends and elbows and the lengths of straight tubing between them. Because of this sensitivity, direct calibration or simulation is required to assess nanoparticle penetration efficiencies for any flow system containing bends or elbows at low Reynolds number. When the Reynolds number exceeds 250, the enhancement is insensitive to the actual flow configurations. Experimental results are presented, which can be used for design of aerosol flow systems at Reynolds number larger than 250.

To minimize the airborne sampling bias, an advanced differential mobility analyzer (DMA) system for measuring submicron aerosol size distribution at ambient relative humidity, with special attention to implementation on aircraft, has been developed. The system includes an active RH controller, a cylindrical differential mobility analyzer (CDMA), and a condensation nucleus counter. A cascade controller consisting of two PID modules maintains the RH inside the CDMA at ambient RH by actively adding or removing water vapor from the air stream. The flows are controlled with feedback PID controllers, which compensate for the variation of pressure as the aircraft changes altitude. This system was integrated into the CIRPAS Twin Otter aircraft and used to measure ambient size distributions during the Aerosol Characterization Experiment-Asia (ACE-Asia), carried out from March to May, 2001, in Japan.

During the ACE-Asia experiment, the above DMA system, together with an aerodynamic particle sizer (APS), was used to characterize aerosol size distributions in East Asia during 19 flights on board of CIRPAS Twin Otter aircraft. Besides providing the aerosol size characteristics, the data were combined with chemical composition and aerosol mixing state measurements to predict the vertical profile of aerosol extinction, which was compared with those derived from simultaneous direct measurements

of aerosol optical depth by the NASA 14-channel sunphotometer. Agreement between the predicted and derived aerosol extinction varies for different scenarios, but the discrepancies were generally within the calculated uncertainties.

Contents

List of Figures

List of Tables

Chapter 1

Introduction

Aerosol is a very important, but only partially understood, component in the atmosphere. Aerosol scatters the solar radiation back to the space, which leads to a net reduction of Earth energy budget, and consequently the cooling of the atmosphere on both regional and global scales (direct effect). Aerosol can also affect climate by changing the microphysical structure, lifetime, and amount of clouds (indirect effect). Despite recent progresses, the aerosol direct and indirect effects remain the most uncertain components in the climate system. Besides its climatic effects, aerosols are linked to visibility degradation and health risk, such as respiratory distress.

To predict and mitigate the effects of aerosol, further studies are required to improve our understanding of the spatial and temporal distributions, as well as the sources and governing processes, of atmospheric aerosols. Unlike greenhouse gases, such as CO_2 and methane, the lifetime of tropospheric aerosol is on the order of a week. As a result, the temporal and spatial distributions of tropospheric aerosol are highly nonuniform and variable, which can only be characterized through long-term and widespread measurements. Furthermore, in contrast to gas phase species which can be uniquely described by their concentrations, a complete description of aerosol requires the details of size, shape, physical state (solid, liquid, or both), mixing state, chemical composition, and concentration. Of these properties, the concentrations and sizes of particles are particularly important in assessing the properties and impacts of an aerosol population. A variety of instruments are available for characterizing the size and concentration of particles. These instruments, which are based on different principles and cover various size ranges, are often combined to size particle from a few nanometers to several tens of micrometers.

Aircrafts have proven to be effective platforms, and have increasingly been employed for sampling atmospheric aerosol in recent years. Airborne sampling enables a reasonably large spatial domain to be probed, and enables characterization of the 3-dimensional distribution and vertical profile of aerosol properties that elude tradi-

tional ground and ship based measurements. However, aircraft-based measurements have inherent limitations. In addition to constraints on instrument size, weight, and power, measurements must be made rapidly while taking into account the changing pressure, temperature, and relative humidity. Airborne measurements also suffer from biases that result from modifications occurring in the sampling system that brings atmospheric particles to the instruments. For size distribution measurements, modifications arise from both the aircraft sampling inlet and the difference between the ambient relative humidity (RH) and that inside the instrument itself. The difference between RHs results from a combination of ram heating and heat exchange between the air stream and the duct surrounding it. For hygroscopic particles, this RH change can lead to a significant bias in size measurement.

Chapter 2 presents the development of a fast response mixing condensation nucleus counter (MCNC), which was designed to increase the spatial and time resolution of airborne measurements of submicron aerosol size distributions. Size characterization of particles smaller than approximate 0.5 μm is best accomplished using differential mobility analyzer (DMA) systems. The time required for conventional DMA systems to measure size distributions in the submicron range is about 45 seconds. Faster measurements often result in severely smeared signals rendering inversion of the data to determine size distributions impossible. The main obstacle to faster measurements is the long mixing-induced response time of the commercial condensation nucleus counters that are used as detectors in DMA systems. By carefully designing the mixing chamber and downstream condenser, the response time of the MCNC can be significantly reduced. Our experiments demonstrate that a differential mobility analyzer (DMA) coupled with our MCNC can measure complete aerosol size distributions in as little as 2 seconds. This technique will significantly increase the time resolution of submicron aerosol distribution measurements and is ideal for airborne measurements. In addition to its fast response, the MCNC also detects nanoparticles with higher efficiency than commercial, high flow rate condensation nucleus counters.

The Chapter 3 describes the investigation of the enhanced diffusional losses when aerosol passes through bends and elbows. While bends and elbows have long been known to cause impaction losses of supermicron particles, the effects of bends and elbows on the diffusional losses have not been studied. The study described in Chapter 2 showed that the presence of bends or elbows can significantly increase the diffusional losses of particles in nanometer range. Elbows and bends produce secondary flows that moves the flow from the center of the tubing, where the particle concentration is highest, to the tubing wall. This increases the radial particle concentration gradient near the wall, leading to enhanced diffusional losses both inside and downstream of the bend or elbow. The enhanced diffusional losses were determined experimentally for general flow configurations.

To minimize airborne sampling biases, the first airborne DMA system that measures aerosol size distributions at ambient relative humidity has been developed. The DMA system employs an active RH controller that adds or removes water vapor from the aerosol sample to compensate the RH change resulting from ram heating and heat transfer between the aerosol sample and the duct surrounding it. This system was integrated into the CIRPAS Twin Otter aircraft and used to measure ambient size distributions during the ACE-Asia experiment, which was carried out from March to May, 2001, in Japan.

A fundamental question that underlies prediction of aerosol climatic effects is how accurately aerosol radiative properties can be predicted based on measured in situ microphysical and chemical properties. If it can be demonstrated that columnar aerosol extinction and other radiative properties (e.g., absorption, angular distribution of scattering) can be accurately predicted given the knowledge of atmospheric aerosol size and composition, then models that predict these properties can be confidently used to predict climatic effects of aerosols. This so-called radiative closure is attempted in Chapter 5 using data obtained during the ACE-Asia campaign. The aerosol extinctions predicted from in situ aerosol size distribution and chemical com-

position measurements on-board Twin Otter are compared to those derived from simultaneous sunphotometer measurements. Detailed sensitivity analysis is performed to access the degree of closure, and also provide the suggestion of future instrument developments for better characterization of atmospheric aerosol.

Chapter 2

Fast Mixing Condensation Nucleus Counter: Application to Rapid Scanning Differential Mobility Analyzer Measurements

Reference: Wang J., V.F. McNeill, D.R. Collins, and R.C. Flagan, Fast mixing condensation nucleus counter: application to rapid scanning differential mobility analyzer measurements, *Aerosol Sci. Technol.*, 36 (6): 678-689, 2002

Abstract

Condensation nucleus counters exhibit slower time response than expected due to mixing effects within the detector. This mixing produces an exponential distribution of delay times with a characteristic mixing time τ_m that ranges from 0.1 s to 0.9 s for commonly used instruments, and limits their usefulness for measuring rapidly changing aerosols. Moreover, when used as detectors in the scanning electrical mobility spectrometer (SEMS; also known as scanning mobility particle sizer, SMPS), CNCs limit the speed with which size distribution measurements can be made. In order to overcome this limitation, a new, fast-response mixing CNC (MCNC) has been developed and characterized. The time response of this new detector and TSI Models 3025 and 3010 CNCs has been measured using a spark source to generate an aerosol pulse. The mixing induced response smearing of this new detector, τ_m, of this instrument 0.058 s, significantly shorter than either of the other instruments tested. Its lower detection limit is about 5 nm diameter. The high aerosol flow rate of the MCNC (0.65 l min^{-1}), fast time response, and low detection limit make it an ideal detector for SEMS/SMPS measurements. Using this MCNC as a detector for the SEMS, size distribution measurements over the 5 nm to 140 nm range have been made in 3 s with minimal distortion. The size distribution of a coagulation aerosol was effectively recovered by deconvolution with scans as short as 1 s. Uncertainties in the 1 s scans result, in part, from electronics problems in the scanning DMA.

2.1 Introduction

The use of an instrument for measurements other than those for which it was originally designed often reveals previously undetected features of its performance. Thus, particle detection with the continuous flow condensation nucleus counter (CNC) in scanning differential mobility analyzer measurements [79] showed that the detector response was slower than the commonly used counting time bins would suggest. Russell et al. (1995) [57] observed that the particle size distributions measured during scans of increasing voltage (up-scans) did not match those acquired during decreasing voltage scans (down-scans). The up-scans produced tails on the large particle end of the size distribution, while the down-scans produced small-particle tails. Russell et al. (1995) [57] attributed this bias to a distribution of residence times within the CNC. Some particles pass directly through from the flow entrance to the detector, while other particles remain in recirculation zones within the counter for varying times. Russell modeled the flow in the CNC as a plug flow region in series with mixed region. Particles all require the same time, called the plumbing time, τ_p, to pass through the plug flow region, but randomly exit the mixed region producing a distribution of delay times. Assuming that region to be perfectly mixed, i.e., a so-called continuously stirred tank reactor CSTR, the fraction of the particles remaining in that region after residing in it for time t decays exponentially, i.e.,

$$P(t) = \exp\left(-\frac{t}{\tau_m}\right). \tag{2.1}$$

Since this distribution of delay times is caused by mixing within the CNC, we call τ_m the mixing time.

Quant et al. (1992) [54] measured the response times of different CNCs by using a three-way valve to switch from an aerosol flow to a clean gas flow. The TSI Model 3010 had a plumbing delay of approximately 1.2 s; this delay time is somewhat variable

since it depends on the length of tubing between the DMA outlet and the entrance to the CNC. They measured a mixing time of 0.9 s. In contrast, the plumbing delay time of the TSI Model 3025 ultrafine CNC (UCNC) was 0.5 s, while the mixing time was 0.1 s in the high flow rate mode of operation. In the UCNC's low flow operating mode, the two times were 1.7 s and 1 s, respectively.

If precisely known, one can readily take the fixed plumbing delay times into account in data analysis [79], but the distribution of mixing induced delays have profound effects on the use of the CNC. The scanning electrical mobility spectrometer (SEMS; also called the scanning mobility particle sizer, SPMS) records particle counts into a series of counting bins of duration, τ_c. The exponential distribution of delay times allows particles to reach the detector over a period that extend to several times the mixing time. The probability that a particle will be attributed to the proper time bin is $P(\tau_c)$. Only for a counting bin duration greater than the mixing time can the particles be unambiguously attributed to appropriate bins. Thus, the mixing time and the number of counting bins employed impose a practical lower bound on the scan time for the SEMS. The SEMS equipped with the TSI 3010 CNC as a detector can make scans over the full dynamic range of the DMA at a 10:1 ratio of sheath to aerosol flows with little distortion of the size distribution in about 300 s. When shorter scans are used, the counts are smeared into later bins than the simple, plug-flow model would suggest. With data inversion to correct for this smearing, scans as short as 30 to 45 s are routinely employed, but faster size distribution measurements become impractical. The faster response of the TSI Model 3025 enables measurements about 10 times faster, although the very small aerosol flow rate through that counter makes it practical as a SEMS detector only for aerosols with extremely high number concentrations, particularly at the low end of the particle size distribution where the charging efficiency is low. To acquire statistically significant particle counts using the TSI 3025 CNC, one must count particles in each mobility channel for a long time, either through a slow scan, or by summing the counts acquired during a num-

ber of scans. The latter approach is generally preferable if the size distribution being measured varies significantly during the interval required to acquire statistically significant particle counts since it enables measurement of a reasonable approximation of a time-averaged particle size distribution, but a fast response detector that counts particles in a larger volume of sampled aerosol would enable such transients to be quantified.

The mixing time also affects other uses of the CNCs where time is of the essence. Rapid transients in aerosol systems due either to dynamic response, e.g., diesel engine particle emissions, or high speed traversing through different air masses, commonly a problem in airborne measurements. Efforts to probe particle transport through eddy flux correlation measurements are complicated by the relatively slow CNC response, even when the numbers of particles counted in successive time bins suggest that fast measurements are being made. Inferences of rapidly varying concentrations of ultrafine particles by taking the difference between the number concentrations measured with instruments with different time response may also be compromised.

The SEMS/SMPS is routinely used to make measurements with scans so short that some smearing occurs. Some of the effects of the finite time response can be corrected by data inversion. Russell et al. (1995) [57] modeled the time-smearing of counts in the CNC as resulting from a combination of a plug flow region in series with a perfectly stirred volume to produce a transfer function for the scanning DMA. That analysis was, however, based on a model of the DMA transfer function that did not capture the effects of diffusion on the transfer function width at small particle sizes. Moreover, the solution was extremely complex. Recently, Collins et al. (2002) [16] developed a much simpler, and faster, deconvolution algorithm that enables "desmearing" of the data in near real time and that also allows one to account for the diffusion broadening of the DMA transfer function. With this deconvolution, the TSI 3010 CNC is routinely used to make SEMS measurement with scans as short as 45 s. This temporal deconvolution could be applied to other applications of the CNC as well.

In principle, the fixed plumbing delay can be taken fully into account in SEMS data analysis, but long plumbing times introduce uncertainty into the particle size determination. Unless τ_p is precisely known, particles can be attributed to the wrong time bins. One can measure flow rates with a precision of order one percent, although uncertainties are often much larger than this. Error propagation analysis shows that the fractional uncertainty in the plumbing time σ_p is related to the uncertainty σ_Q in the volumetric flow rate Q by

$$\frac{\sigma_p}{\tau_p} = \frac{\sigma_Q}{Q}. \tag{2.2}$$

The uncertainty in the channel attribution thus becomes

$$\sigma_i = \frac{\sigma_Q}{Q}\frac{\tau_p}{\tau_c}. \tag{2.3}$$

Thus, uncertainties in the flow rates through the CNC translate directly into uncertainties in channel attribution. To optimize SEMS performance, one must, therefore, minimize both the mixing time and the plumbing delay time.

In this paper, we describe our efforts to accelerate size distribution measurements through development of a fast response condensation nucleus counter. We shall show that condensation nucleus counter can be made to operate efficiently with much smaller response times than achieved in previous instruments while maintaining the high aerosol flow rate that is needed if the CNC is to be used as a detector for DMA-based size distribution measurements. A very simple, rapid-response mixing CNC is demonstrated and characterized. This instrument has been designed explicitly to achieve fast response while maintaining sensitivity to particles in the nanometer size range. We have reduced both the mixing time and the mean residence time with this detector. Using this detector, scanning DMA measurements can be made in as little as 3 s with minimal smearing, and as little as 1 s if some smearing and the associated data inversion can be tolerated.

2.2 CNC Response Time Limits

The condensation nucleus counter detects particles by condensing a vapor on the particles to grow them to large enough size that they can be counted optically. This measurement involves four steps: (*i*) production of sufficient quantities of vapor; (*ii*) creation of the supersaturation necessary to activate the particles; (*iii*) maintenance of the particles in the supersaturated state long enough to grow to detectable size; and (*iv*) detection of the grown particles. The time required for a condensation nucleus counter to respond to changes in the aerosol concentration is constrained by the sum of the relevant times. The TSI 3010 CNC has a longer plumbing delay than the TSI Model 3025 ultrafine CNC (UCNC) because the aerosol is passed through the saturator in the former instrument, while it is fed directly to the condenser where it meets a separately saturated flow in the latter, eliminating any time delay associated with step (*i*). In addition to reducing the mean residence time within the instrument, introducing the vapor by passing particle-free air through the saturator eliminates the mixing of aerosol within the saturator that leads to the large mixing time of the former instrument. The straightforward acceleration of the measurement in the Stolzenburg and McMurry (1991) [68] design for the UCNC, on which the TSI instrument is based, is essential for a fast response instrument, so we shall not further consider the former design or the passage of aerosol through the saturator.

The minimum response time of the CNC is the time required to grow the particles to detectable size once the necessary supersaturation is established. Mixing and plumbing delays may add further delays. To estimate this time, we consider the growth with the saturator operated at the usual operating CNC temperature of 37°C and with butanol as the working fluid. Particles will activate and grow in the condenser if they are larger than the critical size of

$$D_p^* = \frac{4\sigma v_l}{RT \ln S}, \tag{2.4}$$

where σ and v_l are the surface tension and the molar volume of the condensed liquid, respectively. The growth of a particle of diameter D_p in the presence of a supersaturated vapor is described by Seinfeld and Pandis (1998) [64],

$$\frac{dD_p}{dt} = 2\pi D_p \mathcal{D}'_v (c_{v,\infty} - c_{v,s}) \tag{2.5}$$

where the vapor mole fraction in the gas $c_{v\infty}$ can be expressed in terms of the saturation vapor pressure at the gas temperature and the saturation ratio, $S = p_v/p_{sat}$, i.e., $c_{v\infty} = p_{sat}(T_\infty)S/RT$. The effective vapor diffusivity $D'_v = D_v/\beta(2\lambda/D_p)$ takes into account the binary diffusivity of the vapor and the correction for noncontinuum transport processes, $\beta(2\lambda_v/D_p)$, when the particle is small compared to the vapor smear free path, λ_v [64]. The vapor concentration at the surface is that corresponding to equilibrium at the surface. Taking into account the partial pressure variation due to the Kelvin effect, the surface concentration becomes

$$c_{v,s} = \frac{p_{sat}(T_s)}{RT} \exp\left[\frac{4\sigma v_l}{RTD_p}\right]. \tag{2.6}$$

The particle surface temperature, T_s, is determined by an energy balance on the particle, taking into account the conduction heat transfer and the latent heat of vaporization, ΔH_v, leading to

$$\Delta_T = \frac{\Delta H_v \mathcal{D}'_v p_{sat}(T_\infty)}{k_T T_\infty}\left[S - \exp\left(\frac{\Delta H_v}{RT_\infty}\frac{\Delta_T}{1+\Delta_T} + \frac{4\sigma v_l}{RTD_p}\right)\right], \tag{2.7}$$

where $\Delta_T = (T_s - T_\infty)/T_\infty$ [64]. Equation (2.7) must be solved numerically to determine the particle temperature that is needed in the calculation of the particle growth rate.

The time required to grow particles to a given size has been calculated numerically and plotted in Fig. 2.1 for several values of the temperature difference between the saturator and the condenser. Initial particle sizes were 5 nm diameter, or 10% larger

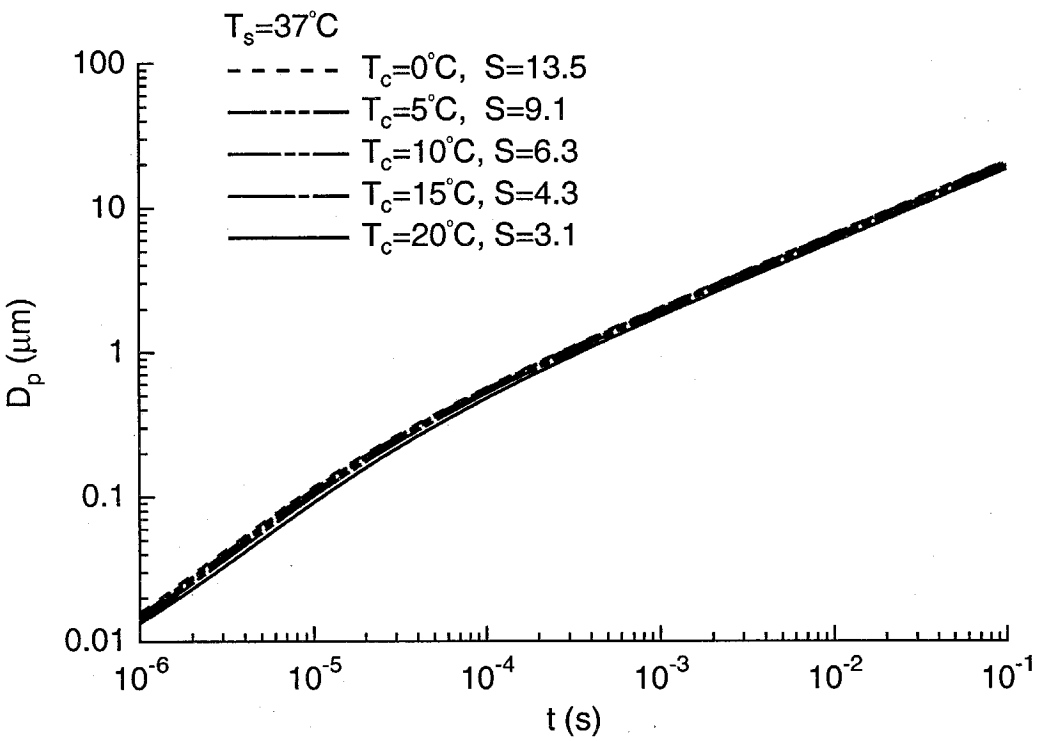

Figure 2.1: Particle growth in laminar flow ultrafine particle CNC.

than the critical size, whichever is larger. Optical detection of growth particles is straightforward once the particle size exceeds roughly 1 μm, so the required growth time is well below one millisecond. At the lowest supersaturation, the driving force for condensation, i.e., the vapor partial pressure in excess of the equilibrium partial pressure is 68% of the vapor pressure leaving the saturator, $p_{sat}(T_s)$, while at the highest supersaturation considered, the difference is 93% of $p_{sat}(T_s)$. The latter driving force is only 37% greater than the former when the saturator is operated at constant temperature. This small difference in driving force accounts for low sensitivity to the condenser temperature that is apparent in Fig. 2.1.

The plumbing delay time of the TSI 3025 UCNC is about 0.5 s, much longer than the time required for growth. That time must also allow for the diffusion of the vapor across the aerosol flow and for cooling of the vapor-laden aerosol to produce the supersaturation. The UCNC also exhibits a smearing time of 0.1 s. While our purpose is not to model the performance of that instrument in detail, it is worthwhile examining some of the factors that determine these response characteristics since particle growth does not appear to be the limiting factor.

The flow in the condenser of the UCNC is laminar, so the vapor and aerosol streams mix by molecular diffusion. The particle diffusivities are much lower than those of the vapor, so the particles follow the streamlines on which they enter the condenser fairly closely, unless some disturbance leads to mixing across the condenser tube flow. That would produce a residence time distribution associated with the laminar tube flow and any recirculations that might be induced.

Assuming that the flow is well behaved, diffusion of vapor across the aerosol stream will delay the onset of growth by a time of order

$$\tau_{da} = \frac{d_a^2}{\mathcal{D}_v}, \tag{2.8}$$

where d_a is the diameter of the aerosol flow jet, and $\mathcal{D}_v$ is the vapor and thermal

diffusivities. This time is short compared to the time scale in which thermal diffusion cools the gas to produce the supersaturation,

$$\tau_{td} = \frac{d_c^2}{\alpha}, \tag{2.9}$$

where d_c is the diameter of the condenser tube, and α is the thermal diffusivity of the gas. Due to the difference in the diameters, $\tau_{da} \ll \tau_{td}$ so the latter time places a lower bound on the growth of particles within the condenser. For the TSI Model 3025 UCNC operated in the high flow rate mode at sea level conditions, this time is estimated to be about $\tau_{td} \approx 0.2$ s due to the tube diameter of 0.46 cm. These delays will contribute to a distribution of grown particle sizes due to delay of activation, but should not cause a distribution of arrival times at the detector. The total residence time in the growth region thus corresponds roughly to the time required to create the growth environment. It is worth noting that the increase in the vapor diffusivity with decreasing pressure will reduce the time required and will accelerate UCNC response.

While the total delay time is reasonable, the cause of the 0.1 s apparent mixing time in the UCNC is not resolved by these calculations. Since all of the particles are, ideally, introduced near the centerline of the condenser tube, laminar flow within the UCNC would not produce a significant distribution of delay times unless some recirculation were present. The interdiffusion of vapor and particles may delay the onset of growth, but should not influence the distribution of times of arrival of particles at the detector. If the particles were dispersed across the cross section of the tube flow, a residence time distribution with approximately the observed characteristic mixing time would result. Alternatively, recirculation zones within the condenser or in the upstream flow passages could cause the smearing within the UCNC. A fast-response UCNC will require that any recirculations be eliminated, or at least reduced in volume, and that the dispersal of particles across the condenser tube be minimized. Particle growth times will still be limited by the time required to

establish the supersaturation within the condenser. While it may be possible to reduce the smearing time by careful attention to those regions of the flow within present instruments where recirculations may be present, the time required for the effect of the cold wall to diffuse to the center of the laminar tube flow remains long. In an effort to reduce both the mean residence time and the mixing time, we have taken a different approach in the present work.

2.3 Mixing CNC

An alternate design for continuous-flow CNCs is the mixing CNC (MCNC), developed by Okuyama, Kousaka, and coworkers [51, 43] based upon the earlier work of Kogan and Burnasheva (1960) [41]. In this instrument, a cold aerosol flow is mixed with a comparable flow of hot, humidified gas. Rapid, nearly adiabatic mixing is facilitated by making the mixing region highly turbulent. Due to the nonlinearity of the temperature dependence of the saturation vapor pressure, mixing of a warm gas stream that is saturated with vapor with a cooler aerosol stream, the aerosol is supersaturated without the use of a cooler. Turbulent mixing can achieve compositional homogeneity rapidly and, as will be shown below, with minimal particle losses. Okuyama et al. (1984) [51] estimated that the growth to particle sizes of order 10 μm in such instruments could be achieved in as little as 50 ms, although previous mixing CNCs have had much longer residence times than that due to the large volumes of the growth regions employed in those designs.

To achieve such a short growth time, the hot, saturated gas and the cold aerosol flow must be mixed in an even shorter time. Corrsin (1957) [19] estimated the time required to dissipate concentration fluctuations in a turbulent mixing region in terms of the turbulent kinetic energy dissipation rate. In the mixing CNC, the turbulent kinetic energy is supplied by the impinging jets. Assuming that the turbulent dissi-

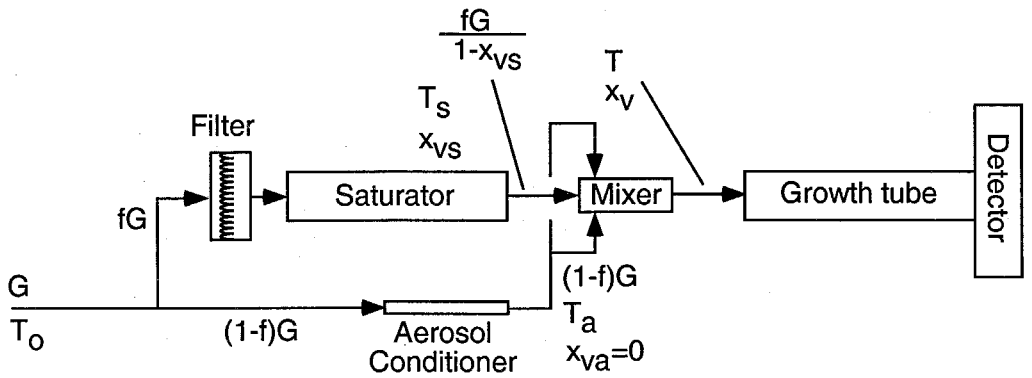

Figure 2.2: Flow arrangement of the mixing CNC.

pation occurs primarily within a region whose length L is on the order of the tube diameter, d_t, and that a fraction ϕ of the total incoming flow rate Q is equally divided among N_j jets of diameter d_j, the turbulent dissipation time, τ_t, is related to the mean residence time in that region τ_{Rt}

$$\tau_t \simeq \tau_{Rt} \left[2N_j^2 \cdot \left(\frac{d_j}{d_t}\right)^4 \left(\frac{d_t}{L}\right)^2 \left(\frac{1}{\phi N_j}\right)^2 \right]^{1/3} \tag{2.10}$$

For sufficiently small jets, $\tau_t < \tau_{Rt}$, and the composition within that small volume is well mixed. Turbulence continues to decay downstream of the region of intense mixing, i.e., downstream of length L, so the $\tau_m > \tau_{Rt} > \tau_t$.

Our present purpose is to develop a fast response MCNC that will allow dramatically accelerated SEMS/SMPS high frequency number concentration measurements. Ideally, we seek to achieve sufficiently fast response to enable DMA scans of 1 s or less. In addition to the dependence of the particle growth rate on pressure, its dependence on the absolute partial pressure of the vapor can be used to accelerate growth. The mixing CNC enables operation at high saturator temperatures and correspondingly high vapor partial pressures. Thus, the MCNC seems particularly well suited to our present purposes.

The MCNC is illustrated schematically in Figure 2.2. A total aerosol flow rate

of G moles air/s is drawn into the instrument. That flow is split, with a fraction f passing through a filter and then through the saturator. The remaining aerosol flow may be passed through a carefully designed conditioner to control its temperature and measure its flow rate. The volume and mixing within this conditioner must be minimized in order to minimize any delays or smearing in the detector response function. The temperature of the gas leaving the saturator is T_s, and the mole fraction of vapor is, ideally, $x_{vs} = x_{sat}(T_s, p)$; the aerosol temperature is T_a. The molar flow rate at the outlet of saturator is increased by the addition of the vapor to

$$G_s = \frac{fG}{1 - x_{vs}}. \tag{2.11}$$

Assuming constant specific heats for the sampled gas (air) and the vapor, and that the mixing is adiabatic, the temperature at the outlet of the mixer is [42]:

$$T = \frac{(1-f)C_{pg}T_a + fC_{pg}T_s + f\frac{x_{vs}}{1-x_{vs}}C_{pv}T_s}{C_{pg} + f\frac{x_{vs}}{1-x_{vs}}C_{pv}} \tag{2.12}$$

The vapor mole fraction at the mixer outlet is

$$x_v = \frac{x_{vs}f}{1 - x_{vs}(1-f)}. \tag{2.13}$$

The saturation ratio, i.e., the ratio of this value to the equilibrium mole fraction at the mixed gas temperature,

$$S = \frac{x_v p}{p_{sat}(T)}, \tag{2.14}$$

may exceed unity due to the nonlinear dependence of the equilibrium vapor pressure on temperature.

Figure 2.3 shows the excess vapor mole fraction $\Delta x_v = (x_v - x_{v,sat})$, saturation ratio, and critical diameter, D^*, as a function of f for several saturator temperatures. By using increases in the saturator temperature to raise the peak supersaturation, the driving force for condensational growth Δx_v can be increased dramatically over

the range of operating conditions examined.

The saturator temperature must exceed a minimum value to produce supersaturation. As the saturator temperature is increased beyond this value, the peak supersaturation shifts toward lower mixing ratios, and Δx_v increases, approaching 5% at the peak supersaturation. The critical diameter corresponding to the peak supersaturation, Fig. 2.3(c), drops below 5 nm for the highest saturator temperatures. It is apparent from this plot that high saturator temperatures are required to achieve low critical particle sizes for MCNC detection. It is worth noting that smaller critical diameters are attainable in the MCNC, although different working fluids may be required to achieve the necessary high supersaturations. This has clearly been demonstrated by de la Mora and coworkers in the measurements of large gas ions with a MCNC [66, 23]. It is also worth noting that particle growth could also be accelerated in the UCNC if the supersaturation were enhanced by increasing the saturator temperature rather than reducing the condenser temperature.

Particle growth can be calculated using Eq. (2.5) as described above. Because of the high vapor partial pressures that can be achieved in the MCNC as we attempt to achieve high growth rates, the local temperature difference between the particle and the gas can be substantial and must be taken into account using Eq. (2.7). Figure 2.4 shows calculated particle growth for a wide range of saturator temperatures at the mixing ratio that produces the peak supersaturation at the indicated saturator temperature. Two points are apparent: (*i*) due to the high vapor partial pressures, the growth times are shorter than are commonly achieved in the laminar flow CNC; and (*ii*) the range of attainable growth rates is much larger than the UCNC. Particles can be grown to readily detectable sizes in as little as 0.1 ms without the additional diffusional delays associated with laminar flow in the UCNC. Moreover, because of the large aerosol flows, particle count rates will be much larger than the UCNC. Thus, it appears that the MCNC should be capable of meeting our objective of enabling fast particle detection through the ultrafine particle size range.

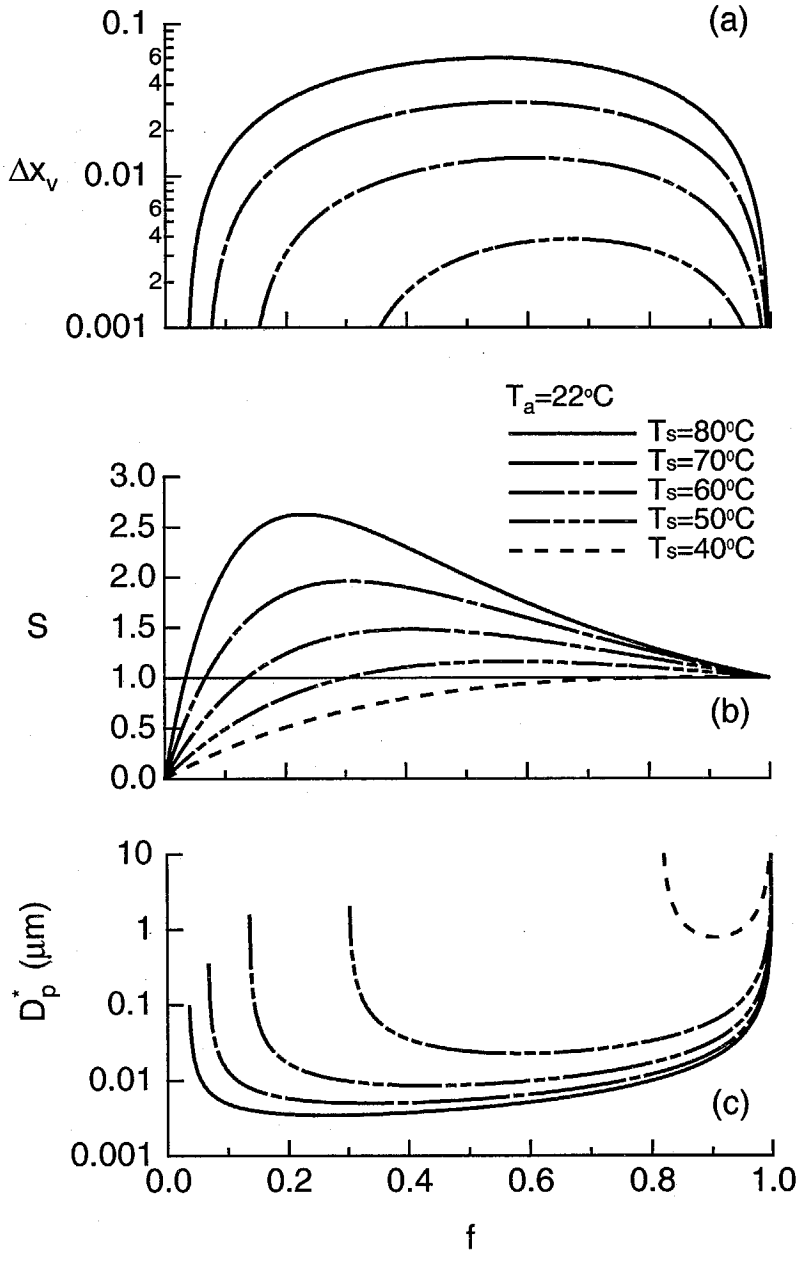

Figure 2.3: Calculated thermodynamic state for mixing CNC operating on butanol at $T_a = 22°$K for various saturator temperatures. (a) Excess vapor mole fraction, (b) saturation ratio, (c) critical diameter corresponding to the peak supersaturation at the indicated saturator temperature.

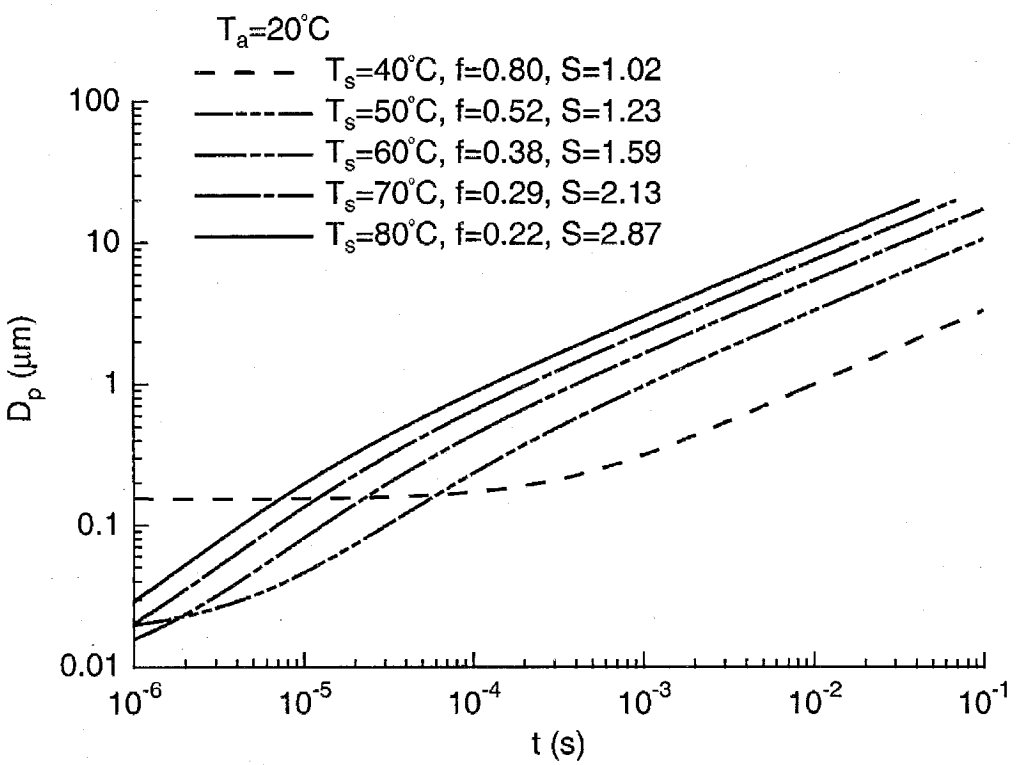

Figure 2.4: Particle growth within an ideal mixing CNC at the peak mixing ratio at the indicated saturator temperature.

2.4 CNC Characterization

2.4.1 Mixing CNC

We constructed a prototype of the fast MCNC sketched in Fig. 2.2. The incoming aerosol was split between the saturator flow and the aerosol sample flow. A fraction of the total flow f is passed through a HEPA filter to remove all particles, and then through a packed bed saturator (a tube filled with n-butanol saturated cotton) that was maintained at a predetermined temperature using a proportional-integral-differential controller algorithm using LabView (National Instruments) data acquisition and control software. For the present experiments, only the saturator temperature was controlled; the aerosol was sampled at ambient temperature. Mixing of the two flows in a small mixing chamber produced the supersaturation. Particles exited the mixing region directly through a small growth tube that connects to the optical particle detector from a TSI Model 3010 CNC. The outlet flow from the CNC passed through a 1.0 l min^{-1} critical flow orifice.

We continuously monitored the flow rate to the saturator by measuring the pressure drop across laminar flow meter with a differential pressure transducer, and controlled it using a proportional flow control valve. A LabView PID controller algorithm controlled the flow rate at the desired value with an accuracy of $\pm 0.2\%$. Since the total flow rate is controlled by the critical orifice downstream of the optical detector, this measurement and control defines the split between aerosol and sample flows.

The fast response of the MCNC derives from the very small volume of the mixing chamber employed. For this initial implementation of the fast MCNC, the mixing chamber was constructed from a $\frac{1}{4}$ inch Swagelok^{TM} cross as illustrated in Fig. 2.5. In original design of mixing-type CNC [42], the cold aerosol flow was surrounded by warm saturated flow to prevent thermophoretic deposition of particles in the mixing chamber. To produce a simple design and ensure rapid and thorough mixing, we

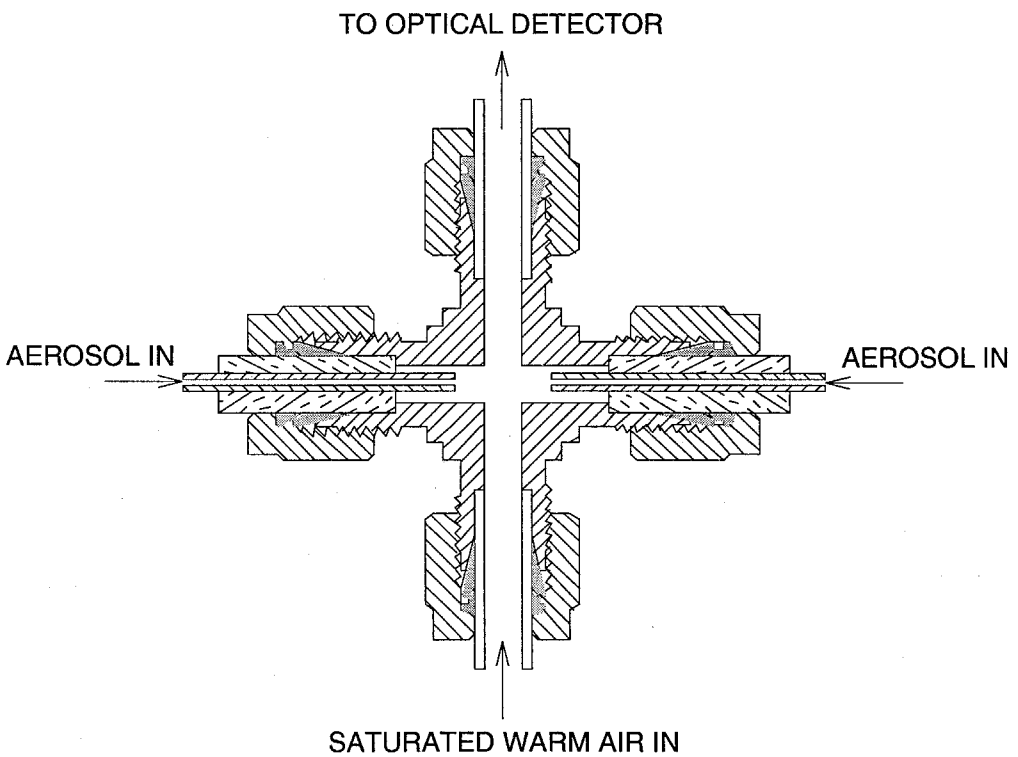

Figure 2.5: Mixer constructed from Swagelok^{TM} cross and used in the demonstration of the fast mixing CNC.

divided the larger aerosol flow into two flows that enter the mixing chamber from opposite sides. The smaller, hot, saturated gas flow entered from the bottom. Counting efficiency measurements, shown below, reveal that thermophoretic and diffusional particle losses in this system are negligible, at least for particles larger than 8 μm diameter. The 0.7 mm internal diameter stainless steel aerosol-introduction tubes produce aerosol jets to ensure good mixing. Polymeric tubes couple the aerosol flow tubes to the cross to minimize thermal coupling prior to mixing. The total volume of the mixing chamber is estimated as 0.85 cm^3. The mean residence time in the mixer is, thus, approximately 0.05 second. The turbulent dissipation time is estimated to be $\tau_t < 0.01$ s. A $\frac{1}{4}$ inch copper tube (0.48 cm internal diameter and 7 cm long) connects the mixer to the optical detector. The combination of that volume with the volume of the nozzle at the entrance to the detector adds an additional residence time of 0.08 s.

2.4.2 Mixing Time Measurement

We measured the plumbing and mixing times of the MCNC and two TSI CNCs by creating a pulse of ultrafine particles with a single discharge in a spark-source aerosol generator [63] immediately upstream of the CNC entrance as illustrated in Figure 2.6. A LabView program initiated a step change in the output voltage of the high voltage power supply and recorded the particle counts. Measurements of the voltage without spark reveal a rise time smaller than 0.02 s. Figure 2.7 shows the particle counts resulting from two measurements. The time delay before the abrupt rise in the particle concentration is $\tau_p = 0.38 \pm 0.013$ s. The spark source rings for some time, creating multiple sparks that lead to a plateau in the particle concentration. Once particle generation ceases, the number concentration decays exponentially with a time constant of $\tau_m = 0.058 \pm 0.002$ s.

Figure 2.8 shows the curve fits to the concentration decay for the MCNC and the

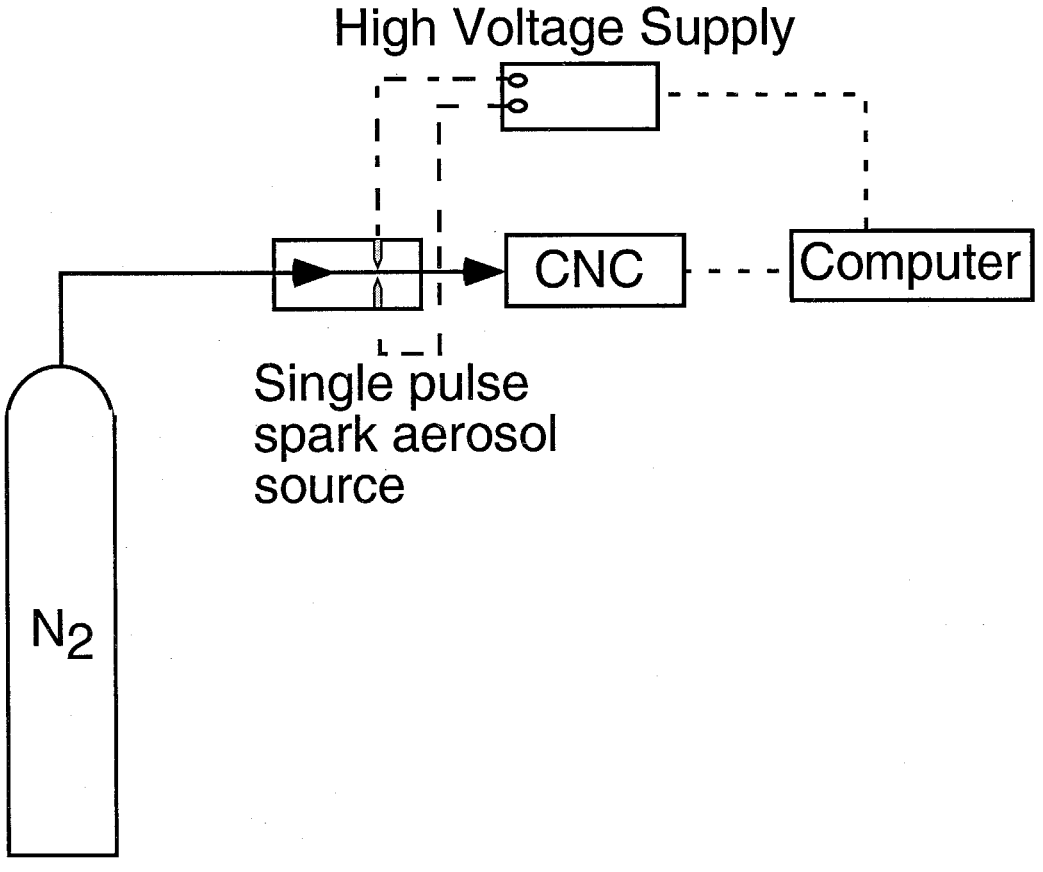

Figure 2.6: Apparatus used for measuring response times. Particles are generated using a spark-source generator immediately upstream from the entrance to the CNC.

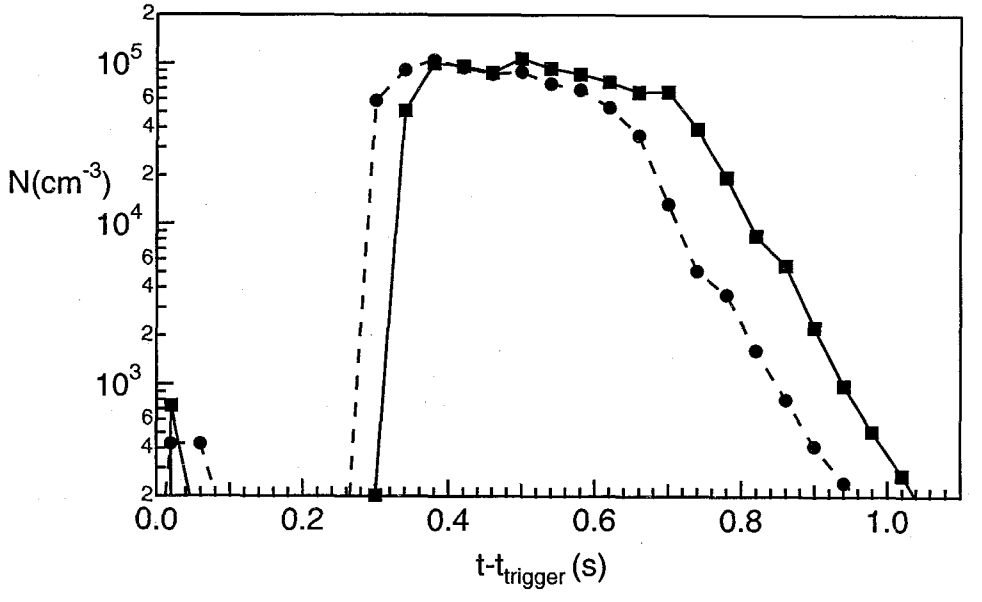

Figure 2.7: Measurements of the number concentration pulse from the spark source aerosol generator with the MCNC.

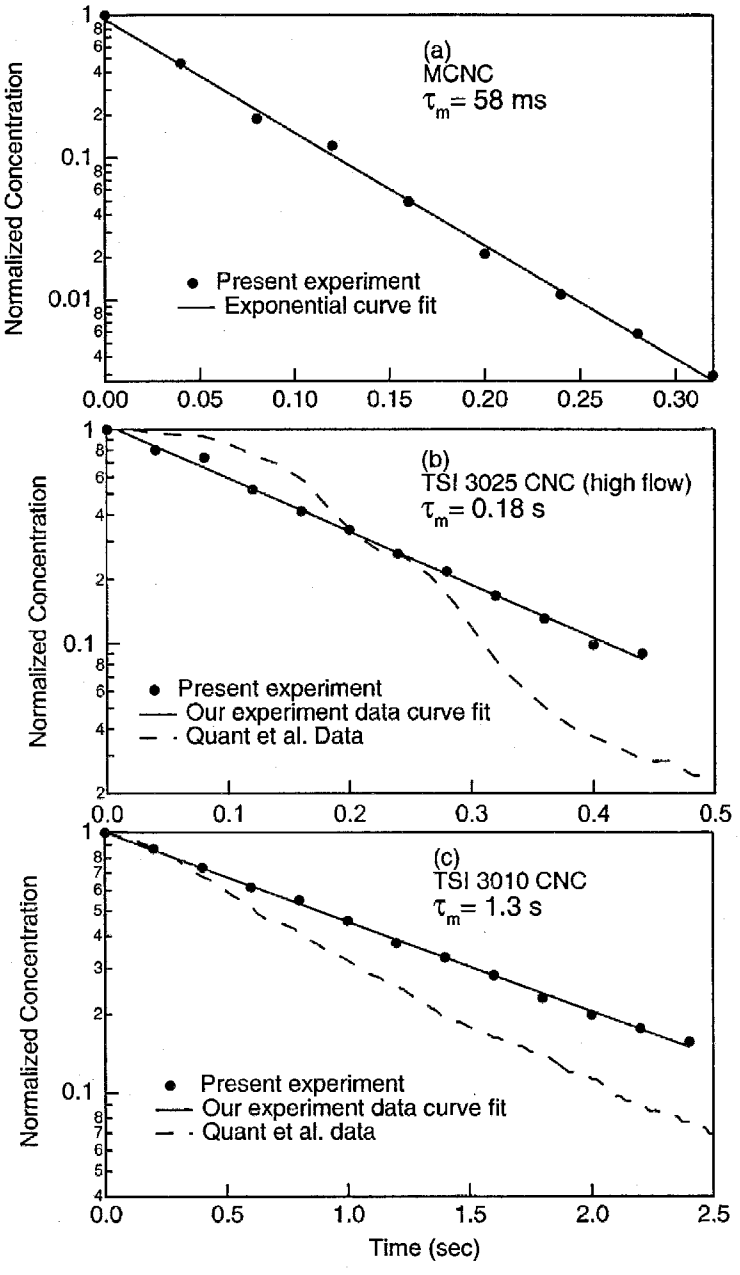

Figure 2.8: Mixing time determination for the MCNC (top), TSI Model 3025 UFCNC (middle), and TSI Model 3010 (enhanced) CNC (bottom). Previously measured decay rates [54] are also shown for the TSI 3025 and 3010 CNCs are also shown as dashed lines.

TSI Model 3025 CNC and a modified TSI model 3010 CNC. Scaled measurements of particle decay by Quant et al. (1992) [54] are also shown for the two TSI detectors. The MCNC response shows a mixing time of $\tau_m = 58$ ms, while those for the TSI Models 3025 and 3010 CNCs are 0.174 ± 0.005 s and 1.35 ± 0.05 s, respectively. The decay rates observed for the TSI counters in the present experiments differ from Quant's results, i.e., 0.10 s for the 3025, and 0.95 s for the 3010. The causes for these differences are unclear. Rather than using an in-line source, Quant et al. (1992) [54] switched from an aerosol flow to a clean air flow using a 3-way valve. This may have perturbed the flows. There may also be differences between the different instruments studied. In particular, the Model 3010 CNC used in the present study had been modified to extend the counting range below 5 nm diameter [58]; the changes may account for some of the difference between the 3010 values. The spark source volume of 2.2 cm^3 introduces a mean residence time of 0.021 s between the aerosol formation point and the entrance to the MCNC. The present values may overestimate the time due to the residence time distribution within the 2.2 cm^3 volume of the spark source and associated plumbing, but that increment is expected to be a small fraction of the 0.021 s mean residence time between the spark source and the entrance to the DMA.

2.4.3 MCNC Counting Efficiency

We probed the MCNC counting efficiency for ultrafine aerosol particles using the apparatus shown in Fig. 2.9. Following the evaporation-condensation method of Bartz et al. (1987) [5], sodium chloride aerosol, produced by nebulizing a solution of 0.05 wt% NaCl into a 2 l min^{-1} air flow with a constant rate atomizer, was evaporated in a 700°C tube furnace and then quenched by injection of 20 l min^{-1} of filtered room-temperature air through four radial jets perpendicular to the center axis. This nucleated ultrafine calibration particles. For coarser particles, we used the output of the nebulizer directly. After the aerosol passed through a ^{210}Po neutralizer,

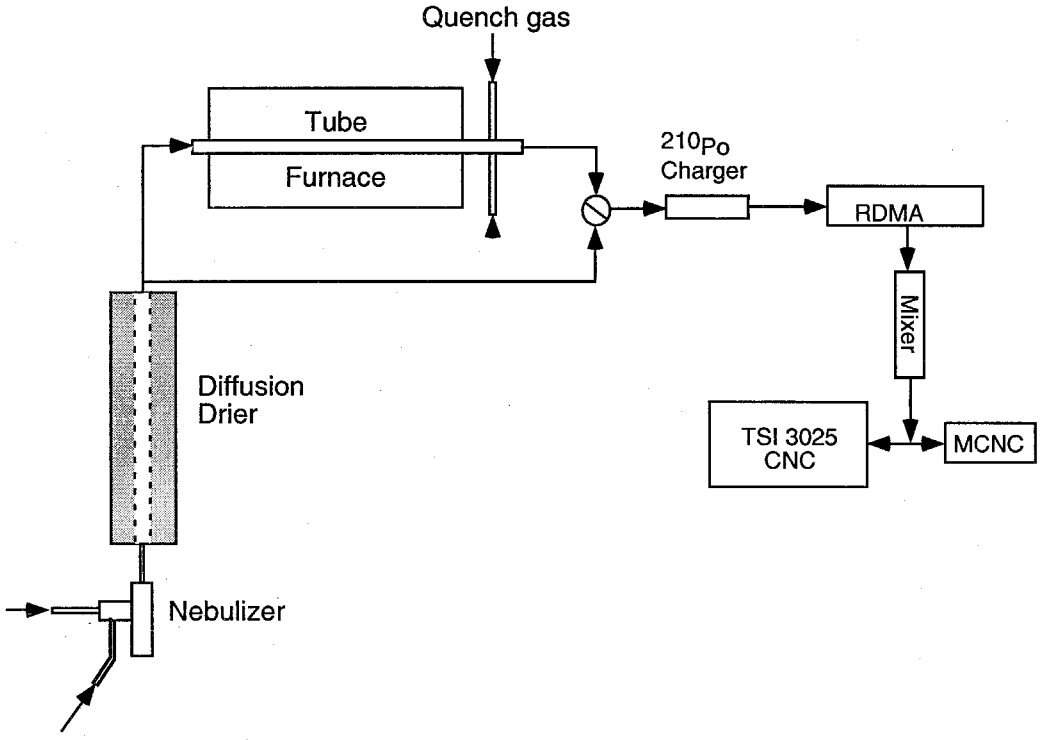

Figure 2.9: Apparatus used to measure the MCNC counting efficiency by comparison to a TSI 3025 UCNC.

classification by a radial DMA (RDMA, [81]) produced a monodisperse test aerosol.

To ensure stable operation, we monitored all of the flows to the RDMA using laminar flow meters that consist of a laminar flow element and a differential pressure transducer, and controlled both the sheath and excess air flows with (MKS) proportional solenoid valves. LabView (National Instruments) software was used to monitor all parameters and execute all control functions through a laboratory computer. Signals from the laminar flow meters and pulses from MCNC and TSI model 3025 UCNC were recorded using an A/D card (National instruments PC-LPM-16), while a 12-bit D/A card (National Instruments AT-AO-6) was used to provide the control voltages to the control valves and high voltage module. The control signal for the high voltage for the RDMA was exponentiated using a log-ratio amplifier to attain uniform precision on a logarithmic voltage scale following the method of Collins (2000) [15]. The control software was based on LabView proportional-integral-differential (PID) controller modules. The RDMA flows were controlled with a precision of $\pm 0.5\%$. The sample flow was 0.491 l min^{-1}, and the sheath and excess flows were maintained at 4.91 l min^{-1}. The MCNC saturator temperature was maintained at 73°C.

Figure 2.10a shows the ratio of the classified aerosol concentration measured with the MCNC to that measured with TSI Model 3025 UCNC. Particles ranging from 5 nm to 150 nm were measured. The ratio is very close to unity for particles larger than 8 nm, indicating that particle losses due to the combined effects of the turbulent mixing, and diffusion and thermophoresis are small. Figure 2.10b compares the counting efficiency of the MCNC to published values for the commercial TSI 3025 [38] and 3010 [47] CNCs. The MCNC efficiency was deduced from the count ratio data of Fig. 2.10a and the published TSI 3025 efficiency. The particle size at which the counting efficiency is 50% is approximately 5 nm in this initial implementation of the MCNC. This is larger than the minimum detection limit of the UCNC, but it should be noted that the MCNC design employed here is very simple and has not been fully optimized. Nor have we explored the influence of saturator temperature or worked

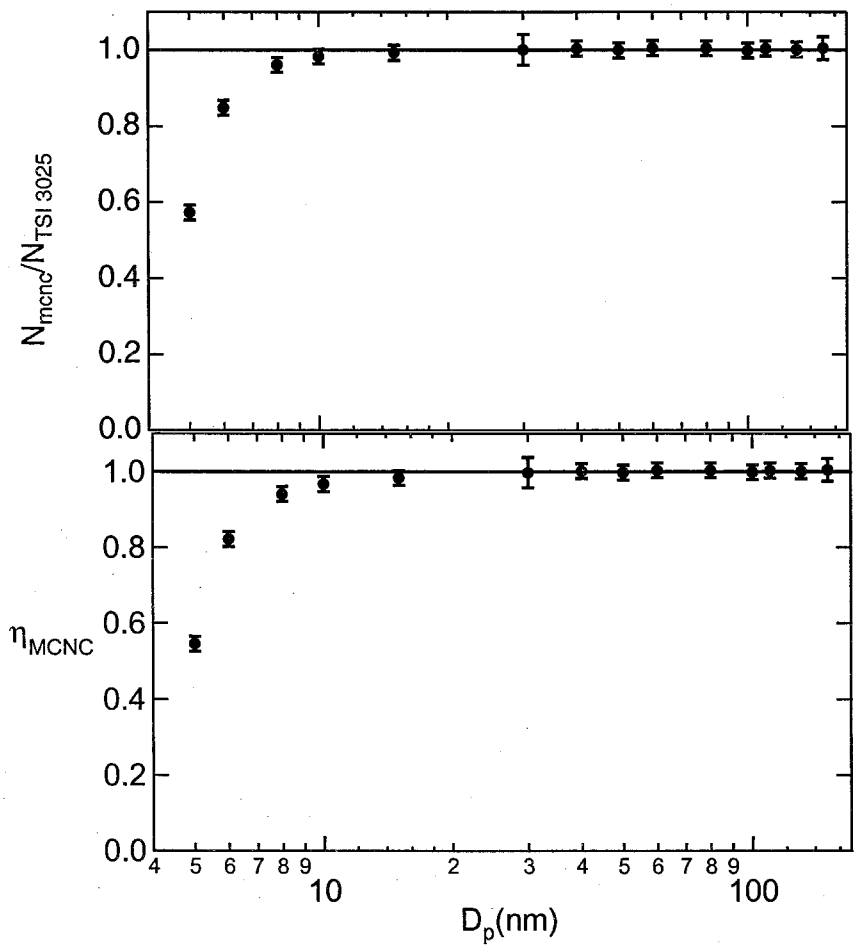

Figure 2.10: Counting efficiency determination. (a) Ratio of the concentration measurements with the MCNC to that with the TSI Model 3025 UCNC and the inferred counting efficiency for the MCNC. (b) Comparison of the counting efficiency for the MCNC to reported values for the TSI 3025 [38] and 3010 [47] CNCs.

Table 2.1: Flows and delay times for different CNCs. Data for TSI CNCs are derived from Quant et al. (1992) [54].

CNC	$Q_{aerosol}$ (l min^{-1})	Q_{total} (l min^{-1})	τ_{delay} (s)	τ_{mixing} (s)	$D_{p,50\%}$ (nm)	Source
MCNC	0.65	1	0.38 ± 0.013	0.058 ± 0.002	5	present work
TSI 3025 (high flow)	0.03	1.5	1.03 ± 0.02	0.174 ± 0.005	3	Present work
TSI 3025 (low flow)	0.03	0.3	1.7	1	3	Quant
TSI 3025 (high flow)	0.03	1.5	0.5	0.1	3	Quant
TSI 3010 (enhanced)	1	1		1.35 ± 0.05	3.5	Present work
TSI 3010	1	1	1.2	0.9	10	Quant

to improve the thermal isolation of the two gas streams, both of which should reduce the minimum detectable particle size. Gamero-Castano and de la Mora (2000) [23] have shown that the MCNC range can be extended to subnanometer sizes by carefully controlling the temperatures of the saturated vapor and aerosol flows to ensure adiabatic operation.

Table I summarizes the fixed delay and "mixing" times for the different models of TSI condensation nucleus counters and the MCNC. The flow rates for the different instruments are also given. It is noteworthy that the aerosol flow rate to the MCNC is 17 times that of the fastest response laminar flow CNCs. This larger aerosol flow rate translates into larger count rates at a given DMA scan rate or, conversely, into equal numbers of particles counted in each channel for much shorter scans.

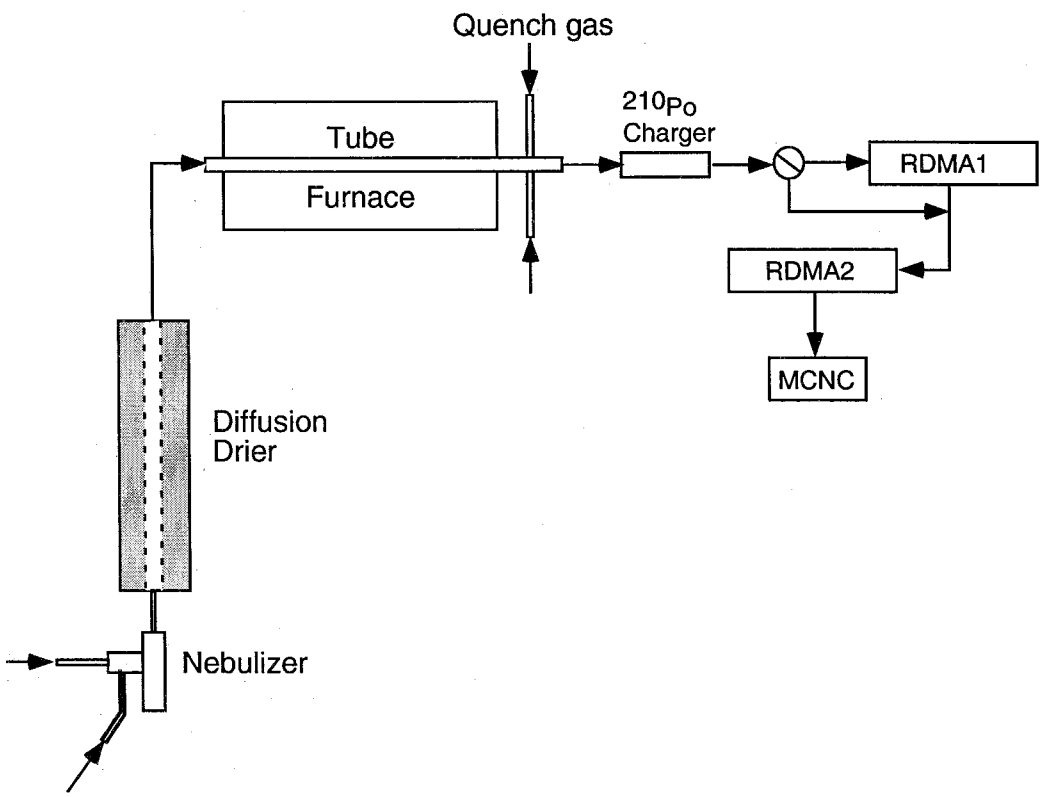

Figure 2.11: Tandem DMA apparatus used examine the performance of the SEMS/SMPS system using the MCNC.

2.4.4 Fast Scanning DMA

We developed this MCNC to enable fast scanning DMA measurements with the SEMS/SMPS. We examined the system performance using the evaporation/condensation aerosol generator, either directly or in the tandem differential mobility analyzer configuration illustrated in Fig. 2.11. This aerosol generator produces a coagulation aerosol of the sort encountered in a wide range of systems. The TDMA system employed two radial DMAs (RDMAs). RDMA1 was used to classify the aerosol at constant voltage, while a second classifier, RDMA2, was scanned to measure the particle size distribution. The sharply peaked particle size distribution produced by RDMA1 accentuates any smearing of the instrument response.

A total of 80 counting bins were employed in each scan, regardless of scan time. Because of limitations in that rate at which charge could be drained from the high voltage power supply used to drive the RDMA, only up scans are reported. Figure 2.12a shows the raw mobility distributions of unclassified aerosols from the evaporation/condensation generator. The measured counts have been corrected for the fixed plumbing delays between the RDMA outlet and the detection point, but not for any smearing due to mixing effects. As the scan time is reduced below about 3 s, distortions appear as finite mixing time (58 ms) approaches or exceeds the counting interval (channel width). For a 2 s scan, 64% of the particles will appear in channels later than expected, and 40% of the particles will be delayed by at least two channels. A 1 s scan delays 40% of the particles by at least 4 channels, causing substantial tails to appear in the measured distributions. Thus, the 1 s scan MCNC smearing is reasonable; it corresponds roughly to a scan of 24 s with the TSI 3010 CPC and a 2 s scan with the TSI Model 3025, operated in the high flow rate mode. It should be noted, however, that the small aerosol flow rate in the latter instrument yields particle counts that are lower than our MCNC by a factor of 17. Deconvolution of the data using the method of Collins et al. (2002) [16], Fig. 2.12b, captures the original distribution even from

the fastest scan.

The smearing becomes much more apparent when an unnaturally peaked distribution is measured, i.e., produced by mobility classification. Figure 2.13a shows the raw data (corrected for fixed delay only) for the mobility classified aerosol. Scans as short as 3 s show little smearing, but a 1 s scan shows significant smearing. Figure 2.13b shows the data after deconvolution.

The inversion of the 1 s scan for the classified aerosol reveals some differences from the slower scans. Several factors contribute to uncertainty in the data inversion. The time bins employed approach the limit of resolution of the LabView algorithms employed in this first implementation of the fast scan. The digital ramp also becomes somewhat noisy at this scan rate. The total number of particle counts is also reduced as the counting bins are narrowed. Nonetheless, the inverted 3 s scan closely approximates the much slower measurements. We even capture the essential features of this sharply peaked aerosol size distribution with the 1 s scan. Additional work on the electronics and control system will be needed, however, before such sharply peaked distributions can be fully resolved with a 1 s scan.

2.4.5 Uncertainties in Ambient Measurements

The expected number of particles counted during scanning DMA measurements is the product of the volumetric flow rate of aerosol that is counted, Q_a, the number concentration of particles in the transmitted particle size interval, $n(\log D_p)\Delta \log D_p$, and the probability that particles in that interval will be charged and transmitted through the DMA to the CNC, p, i.e.,

$$N_e \approx Q_a p n(\log D_p)\ \Delta D_p. \tag{2.15}$$

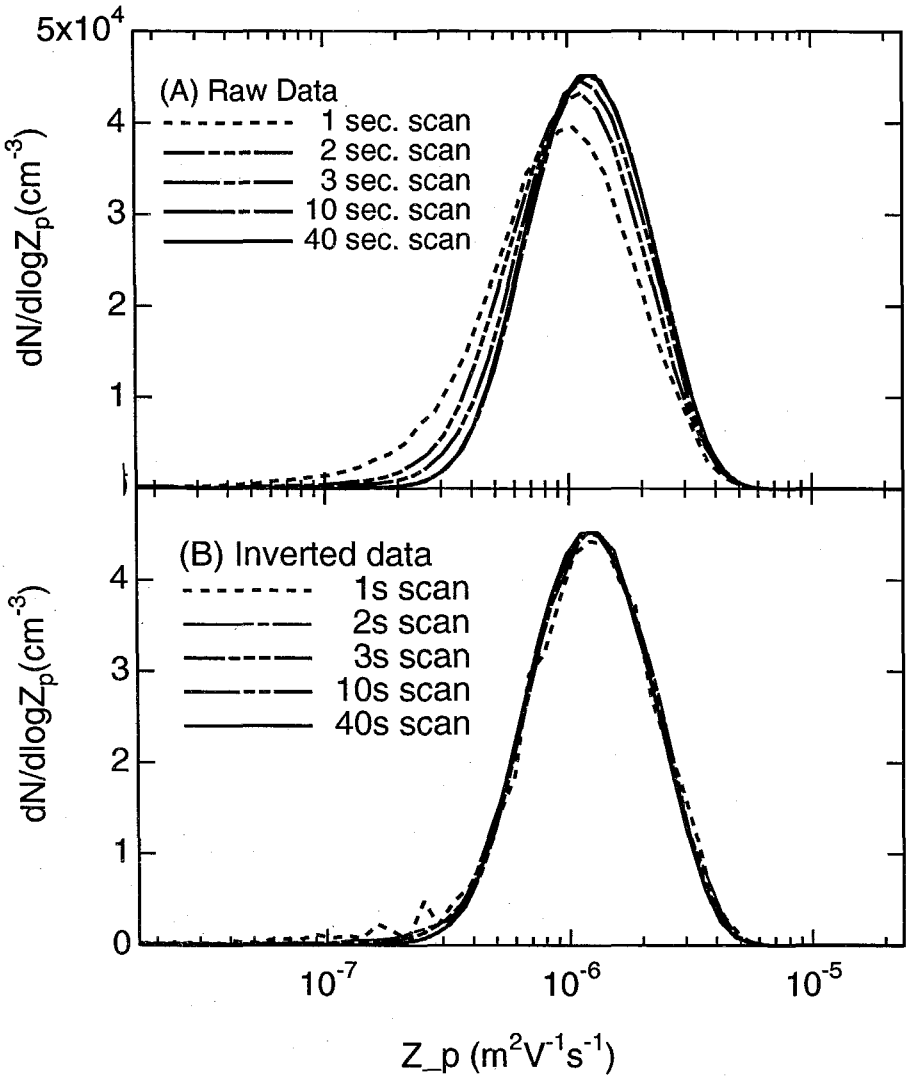

Figure 2.12: Mobility distribution of evaporation/condensation generator aerosol measured with the SEMS using the MCNC as detector. (a) Raw scans; (b) scans after deconvolution with the algorithm of Collins et al. (2002) [16].

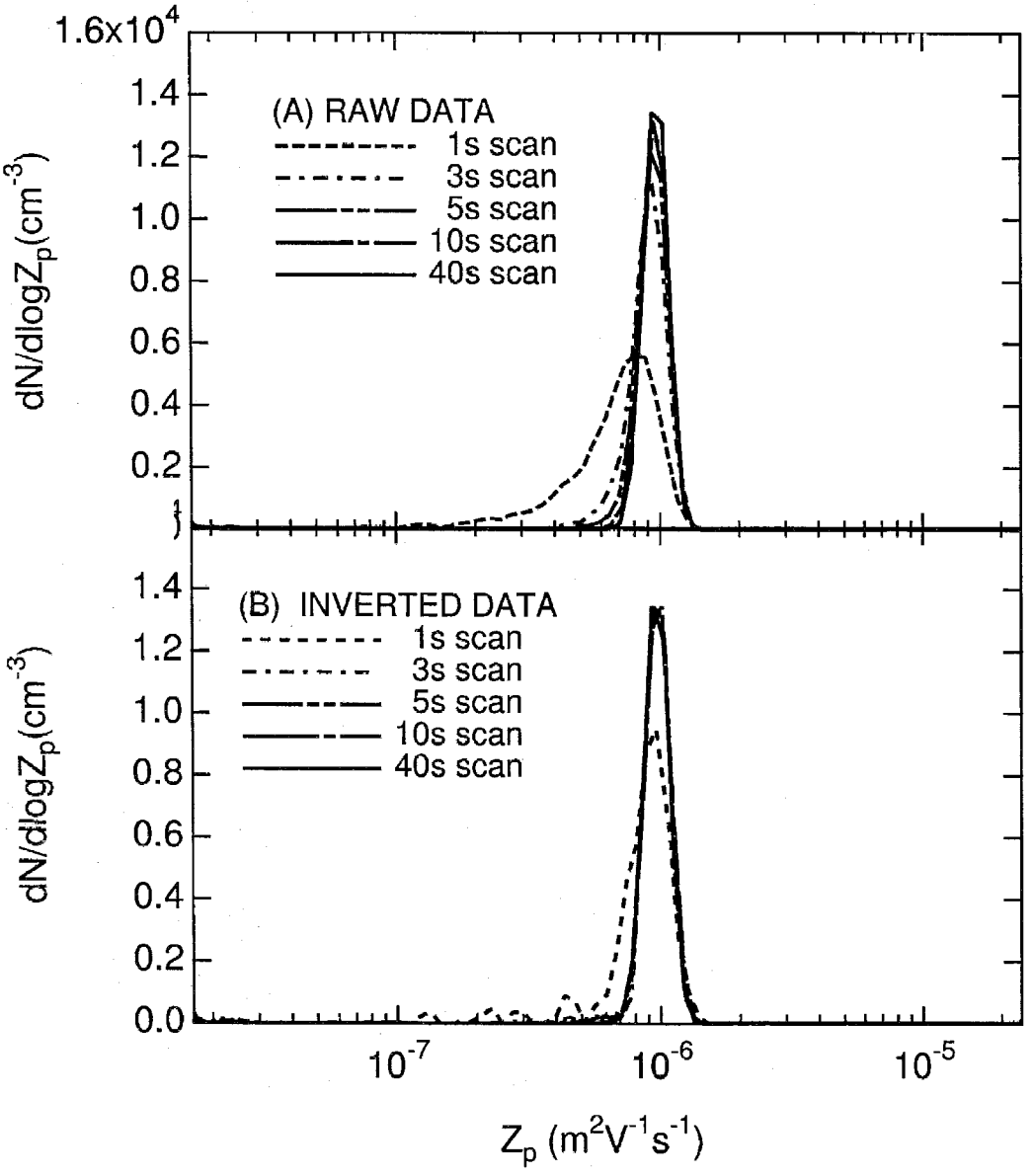

Figure 2.13: Mobility distribution of classified aerosol measured with the SEMS and MCNC. (a) Raw scans; (b) scans after deconvolution with the algorithm of Collins et al. (2002) [16].

Poisson statistics lead to an uncertainty in the actual number of particles counted of

$$\sigma_N \approx \sqrt{N_e}. \tag{2.16}$$

Thus, one makes fast scans knowing that uncertainties in the measurements will be accentuated due to unavoidable degradation of the counting statistics. We probe this effect in Fig. 2.14 by examining the expected performance of the instrument at typical urban (a) and background (b) ambient aerosol concentrations. The uncertainty in the 1 s scan exceeds that of a 1 min scan using either the TSI 3025 as a detector (circles) or the commercial version TSI 3010 (squares). However, a 5 s average of 1 s scans outperforms the Model 3025, and a 1 min average of 1 s scans matches the Model 3010. The large uncertainty in the TSI 3010 distributions below 10 nm diameter results from its low counting efficiency in that size range. Even with the 1 s scan, the size distribution of the urban aerosol is recovered with a concentration uncertainty of about $\pm 15\%$. For the much lower concentrations in the background measurements, the 5 s scan average yields $\pm 25\%$ concentration measurements.

Why then would one use the relatively noisy fast scans, particularly under clean atmospheric conditions? DMA size distributions are measured by scanning, or worse yet, stepping with its additional time delays between measurements, through a range of particle sizes. Each particle size is thus measured at a different time. Fast scans reduce the time lag between measurements of different particle sizes. Even if one must average a number of scans, measurement quality benefits from obtaining a closer approximation to a "true" time average than is possible with slow sequential measurements. In measurements made aboard moving platforms, particularly high speed aircraft, or in the presence of transient sources, e.g., road-side or tunnel measurements of vehicular emissions, this time-averaging may well eliminate biases and misinterpretation that occur when one transits from one air mass to another.

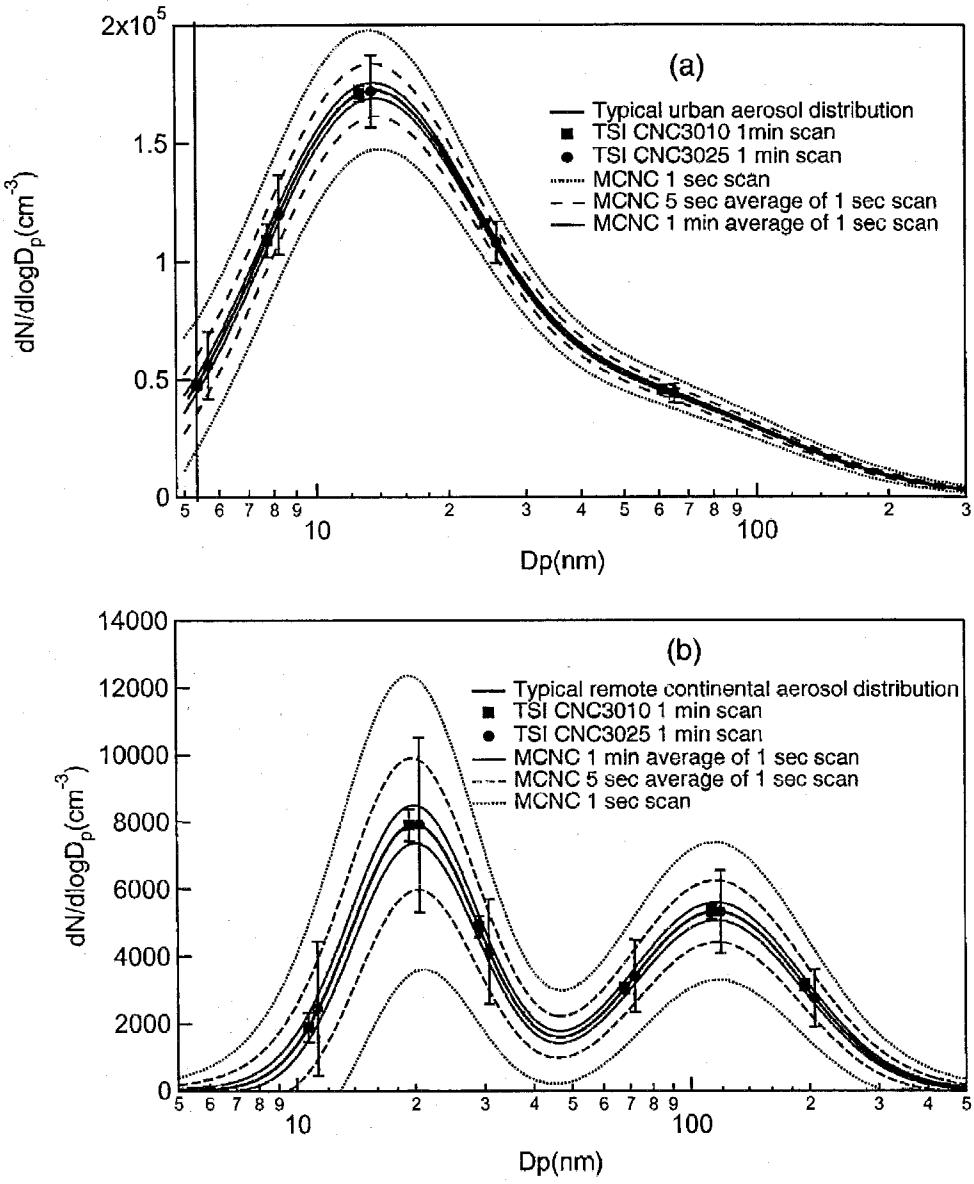

Figure 2.14: Calculated uncertainties in a typical urban (a) and background (b) aerosol for the SEMS/SMPS uses with the MCNC in 1 s scans as compared with 1 min scans using the commercial CNCs as detectors. Uncertainty bands are shown for the MCNC for a single scan, and for 5 and 60 s averages of 1 s scans.

2.5 Discussion and Conclusions

Mixing in flow recirculations within a CNC limits its time response by introducing an exponentially decaying distribution of delays between the time a particle enters the CNC and when it is detected. This was not an issue when CNCs, such as the TSI Model 3010 CNC (based on the earlier Model 3076 design), were first designed, but has important consequences when such detectors are used for time-sensitive measurements. In particular, the distribution of delay times smears scanning DMA size distribution measurements so the full potential of the SEMS/SMPS has not previously been realized. When Stolzenburg and McMurry (1991) [68] separated flow through the saturator from the aerosol flow, they dramatically accelerated the response of the CNC, as evidenced by the short mixing time of the TSI Model 3025, the commercial version of their ultrafine CNC. The very small aerosol flow rate into the condenser region of that instrument has, however, limited its utility for SEMS/SMPS measurements at typical ambient concentrations. Other CNCs, such as the mixing CNCs of Okuyama et al. (1984) [51] have similarly suffered slow response times, because the developers focused their efforts on the counting efficiency rather than the detector response time.

In this paper, we describe a fast version of the mixing CNC that takes advantage of (*i*) the rapid particle growth that is attainable when the partial pressure of the vapor is high, and (*ii*) the rapid mixing that can be achieved with flow-induced turbulence. We have also described a new method for determining the transient response of aerosol detection instruments, at least for particles below 100 nm diameter. With this system, we have quantified the mixing times of two commercial CNCs and our MCNC. Even though the instrument presented here has not been fully optimized, its mixing time is 58 ms, much smaller than the 1.2 s of the Model 3010 CNC tested in this study, and half that of the TSI Model 3025 UCNC. Moreover, the high sample flow rates processed through the MCNC provide the particle counts that are necessary

to take advantage of the faster response. With the new instrument, scanning DMA measurements can be made with minimal mixing-induced distortion in as little as 3 s. The instrument is also capable of resolving typical coagulation aerosols with scans as short as 1 s if the data are deconvoluted.

Residual distortions remained in the fastest (1 s scan) measurements of a sharply peaked particle size distribution produced by mobility classification. A number of factors beyond the problems inherent in data deconvolution may contribute to this distortion. We have digitally controlled a high voltage power supply that is not designed for fast response, so the 1 s voltage ramp suffered greater deviations from the exponential ramp that was sought. Moreover, the fast timing for this ramp is short enough that latency within the present LabView algorithms employed adds noise to the measurements. The effects of these distortions could not be quantified with the present system and remain uncertain. However, both problems can be overcome with improved electronics.

This demonstration has been made using an extremely simple mixing CNC. The mixer was constructed using a Swagelok^{TM} cross. Although we have demonstrated performance that far exceeds present instruments, we have not determined the limits to the technique; we have merely demonstrated that measurements can be made much faster than previously attempted. Higher saturator temperatures or different working fluids should enable detection of particles below the 5 nm 50% detection limit achieved with the present instrument. Reduced mixing and growth tube volumes, or operation at higher flow rates should enable even faster response. Moreover, design for better thermal isolation of the saturated gas from aerosol streams prior to mixing should further enhance performance [23].

Fast scanning DMA measurements are thus enabled by this new detector, but achieving the very short time resolution that such scans suggest will require that adequate particle counts be obtained. Even when count rates are too low for the time resolution to be attained, the fast scanning DMA offers some important advantages

over the slower measurements that have been possible heretofore. By making many size distribution measurements in an interval of time, a reasonable approximation to a true time average can be obtained instead of a succession measurements of different sizes at different times. This is particularly critical in airborne measurements of spatially inhomogeneous air masses. In addition, conditioned sampling techniques can be used to resolve aerosols in different air masses when abrupt transitions are observed. Given the low cost of data acquisition and storage, large numbers of fast scans can readily be recorded for post-experiment analysis.

The fast DMA scans that are enabled by the MCNC also produce some technical challenges for DMA usage. Because of the very large range of voltages that must be scanned in a short time, digital control of the high voltage power supply becomes difficult. Indeed, noise in the power supply combined with low count rates to produce noise in measurements made during 1 s scans. Furthermore, the present power supply was unable to follow scans of decreasing voltage below 5 s scan time. Routine fast-scanning DMA measurements will require either new approaches to digital scan control or a return to analog voltage scanning circuits such as those used by Russell et al. (1996) [58]. When these additional steps are combined with additional improvements in the data acquisition and control algorithms, high resolution SEMS/SPMS measurements in 1 s or even less should be attainable.

2.6 Acknowledgements

The authors would like to thank TSI, Inc., for providing the optical detector. This work was supported by the U.S. Office of Naval Research under Grant Number N0014-96-1-0119. V.F. McNeill received support from the California Institute of Technology Summer Undergraduate Research Fellowship (SURF) program. The authors also gratefully acknowledge the very helpful comments of an anonymous reviewer whose

comments stimulated additional work in revision and significantly enhanced this paper.

Chapter 3

Diffusional Losses in Particle Sampling Systems Containing Bends and Elbows

Reference: Wang J., R.C. Flagan, and J.H. Seinfeld, Diffusional losses in particle sampling systems containing bends and elbows, *J. Aerosol. Sci.*, 33 (6): 843-857, 2002

Abstract

Classical theoretical treatments for diffusional deposition of particles in tube flow describe the losses within straight tubes. The plumbing in many systems of practical interest, notably aerosol instruments, consists of short segments of tubing connected by elbows, bends, and other disturbances. To understand the particle losses in such systems, particle losses in tube flows containing bends and elbows have been studied for Reynolds numbers ranging from 80 to 950. Monodisperse aerosol of 5-15 nm diameter particles passed through individual bends or elbows, and through a number of bends or elbows in series. The results show that the effect of bends and elbows on particle diffusion loss is significant. For a flow configuration with four elbows in series, the penetration efficiency drops as much as 44% when compared to a straight tube with the same length. For Reynolds number smaller than 250, the enhancement of diffusion losses due to bends and elbows is sensitive to both the relative orientations of the bends and elbows and the lengths of straight tubing between them. Because of this sensitivity, direct calibration or simulation is required to assess nanoparticle penetration efficiencies for any flow system containing bends or elbows at low Reynolds number. When the Reynolds number exceeds 250, the enhancement is insensitive to the actual flow configurations. Experimental results are presented, which can be used for design of aerosol flow systems at Reynolds number larger than 250.

3.1 Introduction

Diffusional deposition of ultrafine aerosol particles limits the efficiency with which they can be measured. Gormley and Kennedy (1949) [25] first derived the penetration efficiency for diffusional particles in fully developed laminar flow through a circular tube with a uniform inlet particle concentration. The key parameter determining the transmission efficiency is the particle Peclèt number, $\mathrm{Pe} = \bar{U}d/D$, where $\bar{U}$ is the mean velocity, d is the tube diameter, and D is the particle diffusivity. Focusing on high Peclèt number flows, Gormley and Kennedy(1949) [25] neglected axial diffusion; Tan and Hsu (1971) [69] showed that this assumption is valid for $\mathrm{Pe} > 100$, and when $L/d > 100$ when $1 < \mathrm{Pe} < 100$. These conditions are satisfied in most aerosol sampling instruments.

The parabolic velocity profile of fully developed laminar flow is established within a length $L_{fd} = 0.05d\mathrm{Re}$, where $\mathrm{Re} = \bar{U}d/\nu$ and ν is the kinematic viscosity [35]. Chen and Comparin (1976) [9] demonstrated that the effects of the developing velocity profile near the tube entrance can be neglected provided the Schmidt number, $\mathrm{Sc} = \nu/D \geq 10$. At room temperature and atmospheric pressure, this condition is satisfied for particles larger than 2 nm in diameter.

While particle penetration through straight tubes is well studied, the plumbing within aerosol instruments and sampling systems usually contains many bends, elbows, and other disturbances connected by relatively short lengths of tubing. Although the lengths of the flow paths within the bends or elbows are generally short compared to the connecting tubes, strong secondary flows transverse to the primary flow direction that are generated when a fluid passes through the bend [34] transport particles from the core of the flow toward the walls, greatly enhancing diffusional deposition both inside and downstream of the bend or elbow. The strength of the secondary flow produced by flow through a smooth bend of radius R increases with

increasing Dean number,

$$\mathrm{De} = \mathrm{Re}\sqrt{\frac{d}{2R}}. \tag{3.1}$$

The influence of these secondary flows on inertial deposition has been studied [53, 73], but diffusional particle deposition within and downstream of bends and elbows has received little attention. Insights into diffusional deposition in such flows can, however, be drawn from the analogy between heat and mass transfer. Ede (1961) [21] studied the impact of 90° bends on downstream heat transfer in both laminar and turbulent flows. He found substantial enhancement of heat transfer in the laminar flow regime. Moreover, the temperature profile in the flow entering the bend significantly influenced the enhancement. Mehta and Bell (1981) [46] found similar results for heat transfer in straight tubes downstream from 180° bends. Although these studies provide important insights, their results cannot be applied directly to the diffusional deposition of particles in isothermal flow since natural convection was significant in both studies.

This work focuses on diffusional deposition through two flow geometries that are commonly found within aerosol instruments, 90° bends and elbows, specifically the Swagelok^{TM} elbows that are found in many aerosol flow systems and instruments (Figure 3.1). Ideally, this type of study would parameterize the losses in a way that could easily be applied to the design of aerosol flow systems. Studies of the influence of a single bend with sufficient lengths of tubing both upstream and downstream to ensure fully developed flow would be quite general. Unfortunately, as will be demonstrated below, the complex interactions between the particle concentration profile and the secondary flows produced by successive bends or elbows separated by finite lengths of tubing confounds efforts at such generalization and making experimental quantification of diffusional losses essential at low Reynolds numbers.

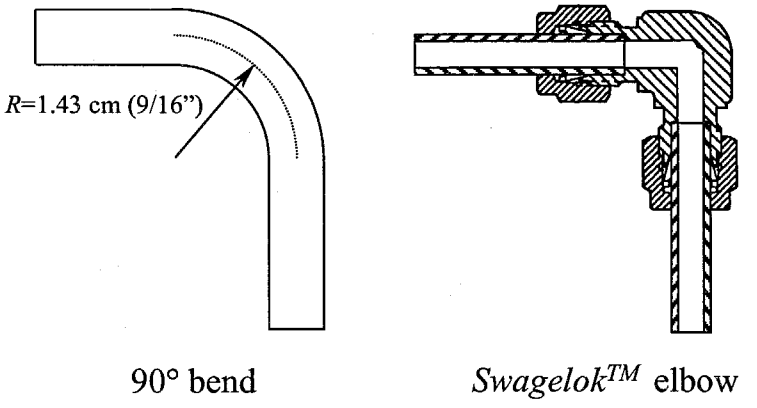

Figure 3.1: Flow geometries of the 90° bend and Swagelok^{TM} elbow used in this study.

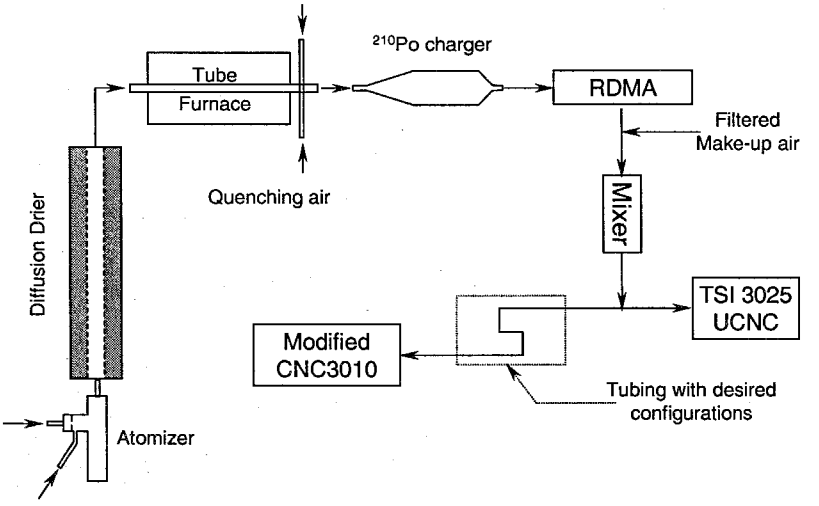

Figure 3.2: Experimental setup for measuring particle penetration efficiencies of tubes of different configurations.

3.2 Experimental Description

Losses in 90° bends and *Swagelok*^{TM} elbows, illustrated in Fig. 3.1 have been studied using the apparatus illustrated in Figure 3.2. The test aerosol was generated using an evaporation-condensation aerosol generator [5]. A sodium chloride aerosol, produced by nebulizing a salt solution was evaporated completely in a 700°C tube furnace with a residence time of about 1 s. Ultrafine NaCl particles were then generated by quenching the vapor-laden gas by mixing with cold air injected through four radial jets perpendicular to the central axis. The resulting intense and rapid cooling induced homogeneous nucleation of the vapor, while dilution of the product aerosol minimized coagulation. To produce a high particle concentration in the size range of interest, a 0.05% NaCl solution was atomized into a 2 L min^{-1} air flow and quenched with 20 L min^{-1} of room temperature air. The aerosol was neutralized using a ^{210}Po charger and then classified by a radial DMA (RDMA, [81]) to produce a monodisperse test aerosol.

We measured the transmission efficiencies of a variety of tube configurations by passing the monodisperse aerosol through each tube assembly. Particle concentrations at the outlet of the tubes were measured by a condensation particle counter, TSI model 3010, modified to extend the lower detection limit to 3 nm diameter while maintaining the large aerosol sample rate (1 L min^{-1}) of the TSI 3010 CPC(CPC3010, [56]). An ultrafine condensation particle counter, TSI model 3025 (UCPC 3025), was used to monitor the output of the aerosol source continuously, enabling one to correct the CPC3010 concentrations for any variations of aerosol source concentration. We measured the particle penetration efficiency over a range of controlled flow rates. For flow rates smaller than the modified CPC3010 sample rate, filtered makeup air was introduced downstream of the tube assembly; for higher flow rates, an appropriately sized critical orifice was used to remove extra flow upstream of the CPC3010.

3.3 Data Analysis

We seek to determine the enhancement of particle losses induced by flow through a bend or elbow. The maximum penetration efficiency of noninertial particles through a flow system with total length, L, including straight tubes and internal passages within bends and elbows, can be calculated using the solution of Gormley and Kennedy (1949) [25] to the convective diffusion of particle through a straight, circular tube with a uniform inlet concentration and fully developed laminar flow. They found that the penetration efficiency is

$$\eta_{G.K.}(x) = 8 \sum_{n=0}^{\infty} \frac{G_n}{\lambda_n^2} \exp(-\lambda_n^2 x), \tag{3.2}$$

where $x = \frac{2L}{d}\mathrm{Pe}^{-1}$. $\lambda_n^2 = 7.312, 44.62, 113.8$ for $n = 0, 1, 2$, respectively, and $\lambda_n^2 = (4n + \frac{8}{3})^2$ when $n > 2$; $G_n = 0.749, 0.544, 0.463$ for $n = 0, 1, 2$, respectively, and $G_n = 1.01276\lambda_n^{-1/3}$ when $n > 2$ [65]. For $x \ll 1$, Ingham (1975) [36] showed that the penetration efficiency asymptotically approaches

$$\eta(x) = 1.0 - 4.07x^{2/3} + 2.4x + 0.466x^{4/3} + \cdots. \tag{3.3}$$

Alonso et al. (1997) [1] showed experimentally that the Gormley and Kennedy (1949) [25] theory is accurate for particle as small as 2 nm under conditions commonly found in aerosol instruments.

Particle penetration through a flow system can be calculated from the measured particle concentration at the entrance, N_0, and outlet, N_e, i.e.,

$$\eta_{sys} = \frac{N_e}{N_0}. \tag{3.4}$$

The system transmission efficiency through a series of $n + 1$ segments connecting n

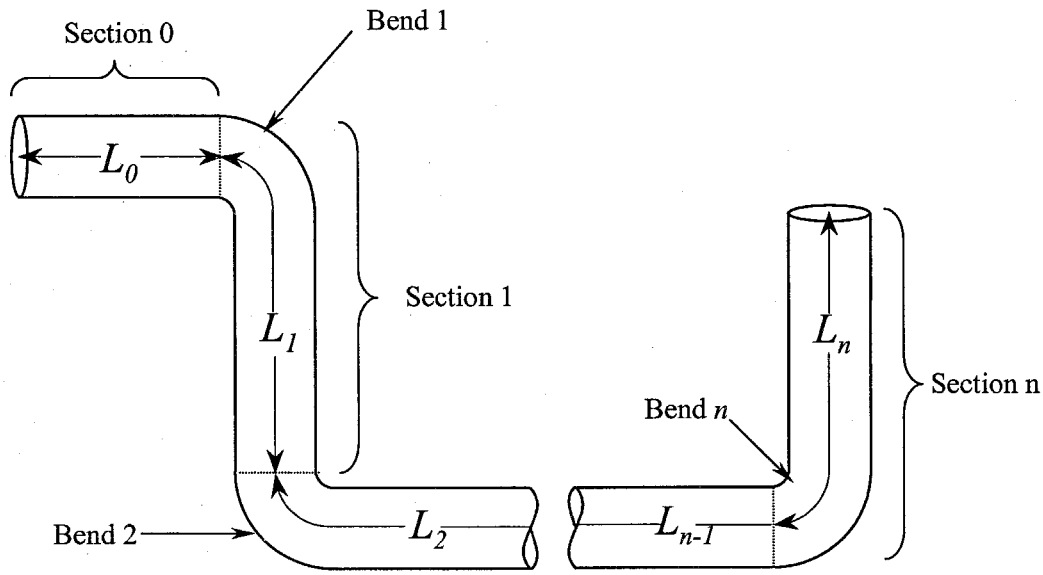

Figure 3.3: Particle sampling system including $n+1$ straight tubes connected by n bends.

bends or elbows as illustrated in Fig. 3.3 can be expressed as the product of the transmission efficiencies through the individual segments, η_i,

$$\eta_{sys} = \prod_{i=0}^{n} \eta_i. \tag{3.5}$$

Losses within each flow segment that has a flow disturbance (bend or elbow) at its entrance will exceed those predicted with the Gormley and Kennedy (1949) [25] model. To characterize the losses caused by such disturbances, we define the effective transmission efficiency of the flow element as the ratio of the observed efficiency to that of a straight tube of the same total length, including both the length of the flow path within the bend or elbow and the downstream straight tube, $\eta_{G.K.}(x_i)$, as

$$\eta_{Ei} = \frac{\eta_i}{\eta_{G.K.}(x_i)}, \tag{3.6}$$

where $x_i = \frac{2L_i}{d}\mathrm{Pe}^{-1}$. The entrance to the flow system is a straight tube of length x_0

with no upstream disturbance, so $\eta_{E0} = 1$ and

$$\eta_0 = \eta_{G.K.}(x_0). \tag{3.7}$$

Prediction of particle penetration efficiencies of sections $1, 2, \cdots, n$ is not straightforward. First, inside the bends, particle loss depends on the geometry of the bends and resulting complex flow field. Then, the secondary flow inside the bends redistributes the particles across the tube cross section, changing the particle diffusion losses in the straight tube downstream of the bend. Numerical simulations by Tsai et al. (1990) [73] revealed that the strength of the recirculation inside a 90° bend depends on the velocity profile across the inlet of the bend. Among three inlet velocity profiles studied (fully developed, partially developed, and uniform), flow with a fully developed inlet velocity profile exhibits the strongest effects of recirculation, while the uniform inlet profile produced the weakest effect. The maximum Stokes number of our experiments was 2×10^{-5}, so the impaction losses were neglected. Therefore, the particle penetration efficiency of section i is written as a function of following parameters,

$$\eta_i = \eta_i(\mathrm{Re}, \mathrm{Sc}, \mathrm{De}, x_i, \widetilde{C}_{i0}, \widetilde{\boldsymbol{U}}_{i0}), \tag{3.8}$$

where $\widetilde{C}_{i0}$ and $\widetilde{\boldsymbol{U}}_{i0}$ are nondimensional particle concentration profile and flow velocity profile at the entrance of the section i, respectively. The effective particle penetration efficiency of bend i is, therefore,

$$\eta_{Ei}(\mathrm{Re}, \mathrm{Sc}, \mathrm{De}, x_i, \widetilde{C}_{i0}, \widetilde{\boldsymbol{U}}_{i0}) = \frac{\eta_i(\mathrm{Re}, \mathrm{Sc}, \mathrm{De}, x_i, \widetilde{C}_{i0}, \widetilde{\boldsymbol{U}}_{i0})}{\eta_{G.K.}(x_i)}. \tag{3.9}$$

When $\mathrm{De} \gg 1$, the secondary recirculation flow inside the bend is strong, so the particle concentration profile leaving the bend is nearly uniform. When the flow path within the bend is a small fraction of the total flow path of section i, the penetration efficiency at large De could be approximated as $\eta_{G.K.}(x_i)$, and $\eta_{Ei} \approx 1$.

This is supported by experiment results presented in the next section. The particle concentration entrance length is [37]

$$L_c \cong 0.05d\mathrm{ReSc} = 0.05d\mathrm{Pe}. \tag{3.10}$$

When $x > x_c$, where $x_c = \frac{2L_c}{d}\mathrm{Pe}^{-1} \approx 0.1$, only the first term of Eqn. (3.2) is of significant,

$$\begin{aligned} \eta_{G.K.}(x) &= 8\sum_{n=0}^{\infty}\frac{G_n}{\lambda_n^2}\exp(-\lambda_n^2 x) \approx 8\frac{G_0}{\lambda_0^2}\exp(-\lambda_0^2 x) \\ &= \eta_{G.K.}(x_c)\exp\left[-\lambda_0^2(x-x_c)\right]. \end{aligned} \tag{3.11}$$

Similarly, for the particle penetration efficiency of section i,when $x_i > x_c$, we have,

$$\eta_i(\mathrm{Re},\mathrm{Sc},\mathrm{De},x_i,\widetilde{C}_{i0},\widetilde{\boldsymbol{U}}_{i0}) = \eta_i(\mathrm{Re},\mathrm{Sc},\mathrm{De},x_c,\widetilde{C}_{i0},\widetilde{\boldsymbol{U}}_{i0})\exp\left[-\lambda_0^2(x_i-x_c)\right]. \tag{3.12}$$

When straight tubes between bends exceed the particle concentration entrance length (and are much longer than the flow entrance length since $\mathrm{Sc} \gg 1$), both the particle concentration profile and flow velocity profile at the inlet of section i are fully developed, i.e., $\widetilde{C}_{i0} = \widetilde{C}_d$ and $\widetilde{\boldsymbol{U}}_{i0} = \widetilde{\boldsymbol{U}}_d$, where the subscript d denotes the fully developed profile. We have,

$$\begin{aligned} \eta_{Ei}(\mathrm{Re},\mathrm{Sc},\mathrm{De},x_i,\widetilde{C}_d,\widetilde{\boldsymbol{U}}_d) &= \frac{\eta_i(\mathrm{Re},\mathrm{Sc},\mathrm{De},x_i,\widetilde{C}_d,\widetilde{\boldsymbol{U}}_d)}{\eta_{G.K.}(x_i)} \\ &= \frac{\eta_i(\mathrm{Re},\mathrm{Sc},\mathrm{De},x_c,\widetilde{C}_d,\widetilde{\boldsymbol{U}}_d)\exp\left[-\lambda_0^2(x_i-x_c)\right]}{\eta_{G.K.}(x_c)\exp\left[-\lambda_0^2(x_i-x_c)\right]} \\ &= \frac{\eta_i(\mathrm{Re},\mathrm{Sc},\mathrm{De},x_c,\widetilde{C}_d,\widetilde{\boldsymbol{U}}_d)}{\eta_{G.K.}(x_c)} \\ &= f(\mathrm{Re},\mathrm{Sc},\mathrm{De}). \end{aligned} \tag{3.13}$$

Eqn. (3.13) indicates that when the length of a straight tube between bends exceeds the particle concentration entrance length, η_{Ei} depends only on three dimensionless numbers: Re, Sc, and De.

Figure 3.4 shows the predicted flow and particle concentration entrance lengths for particles of 5, 8, and 15 nm diameter as a function of flow rate. The particle concentration entrance length increases with increasing volumetric flow rate and particle size. For 5 nm particles, the concentration entrance length is about 1.5 m at a flow rate 0.3 L min^{-1}. At the higher flow rates that are often used to minimize diffusion losses in sampling nanometer size particles, the concentration entrance length is even longer. In practical particle sampling systems and aerosol instruments, the straight tubes between bends are usually much shorter than the concentration entrance length; so η_{Ei} also depends on the actual plumbing geometry of the sampling system, i.e., the lengths of straight tubes and the orientations of the bends. Multiplying both sides of Eqn. (3.9) by $\eta_{G.K.}(x_i)$ and inserting into Eqn. (3.5), the system transmission efficiency for n bends in series becomes,

$$\begin{aligned} \eta_{sys} &= \eta_{G.K.}(x_0) \prod_{i=1}^{n} \left[\eta_{G.K.}(x_i) \eta_{Ei}(\mathrm{Re}, \mathrm{Sc}, \mathrm{De}, x_i, \widetilde{C}_{i0}, \widetilde{\boldsymbol{U}}_{i0}) \right] \\ &= \left[\prod_{i=0}^{n} \eta_{G.K.}(x_i) \right] \left[\prod_{i=1}^{n} \eta_{Ei}(\mathrm{Re}, \mathrm{Sc}, \mathrm{De}, x_i, \widetilde{C}_{i0}, \widetilde{\boldsymbol{U}}_{i0}) \right]. \end{aligned} \tag{3.14}$$

The ratio of the concentration of particles transmitted through a sampling system, N_{sys}, to the concentration transmitted through a straight tube of the same total length, N_{ST}, can be expressed as

$$\begin{aligned} \eta_{R,sys} &= \frac{N_{sys}}{N_{ST}} = \frac{\eta_{sys}}{\eta_{G.K.}(\sum_{i=0}^{n} x_i)} \\ &= \frac{\eta_{G.K.}(x_0) \prod_{i=1}^{n} \left[\eta_{G.K.}(x_i) \eta_{Ei}(\mathrm{Re}, \mathrm{Sc}, \mathrm{De}, x_i, \widetilde{C}_{i0}, \widetilde{\boldsymbol{U}}_{i0}) \right]}{\eta_{G.K.}(\sum_{i=0}^{n} x_i)} \end{aligned}$$

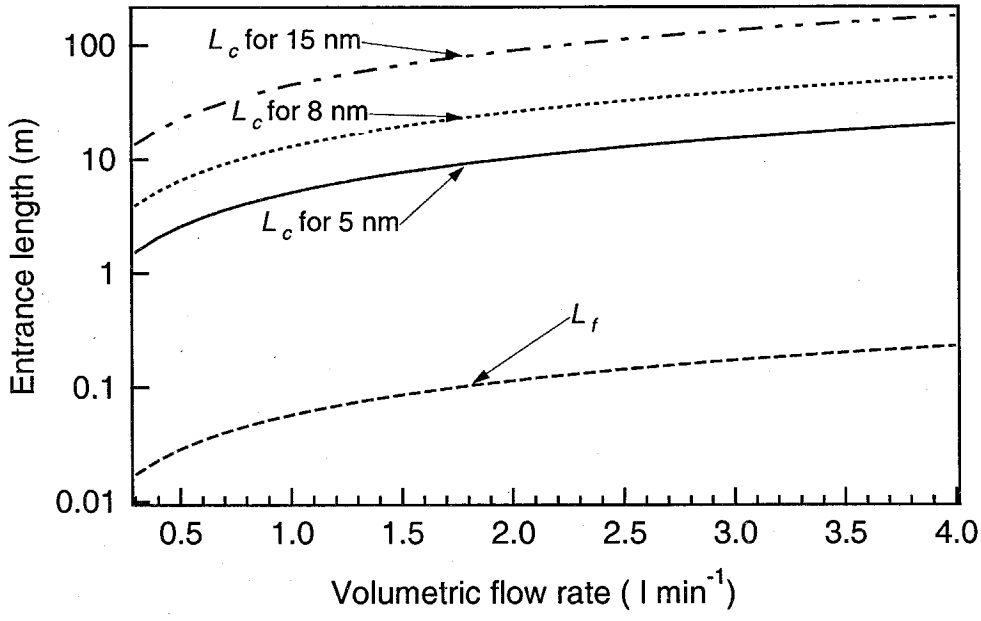

Figure 3.4: Flow entrance length and concentration entrance lengths of particles with 5, 8, and 15 nm diameter as a function of the volumetric flow rate.

$$= \frac{\prod_{i=0}^{n} \eta_{G.K.}(x_i)}{\eta_{G.K.}(\sum_{i=0}^{n} x_i)} \prod_{i=1}^{n} \eta_{Ei}(\mathrm{Re}, \mathrm{Sc}, \mathrm{De}, x_i, \widetilde{C}_{i0}, \widetilde{\boldsymbol{U}}_{i0}). \tag{3.15}$$

The relative system transmission efficiency, $\eta_{R,sys}$, reflects the reduction of particle penetration efficiency due to the presence of bends. $\eta_{R,sys}$ is less than unity for several reasons. At the inlet of a flow element, the particle concentration is highest at the center of the tube cross section due to the preferential particle loss at the wall in the upstream straight tube. Secondary recirculation flow inside the bends redistributes the particles across the tube cross section, transporting the highest particle concentrations from the center to near the wall. This accelerates particle deposition in the downstream straight tube as a result of increased particle concentration gradient near the wall. Therefore, a series of tube segments separated by mixing regions transmits fewer particles than does a straight tube of the same total length. The complex flow within the bends may also cause additional particle losses. The effective penetration efficiency for the ensemble of flow disturbances in a flow system can be defined as

$$\eta_{E,T} = \prod_{i=1}^{n} \eta_{Ei}(\mathrm{Re}, \mathrm{Sc}, \mathrm{De}, x_i, \widetilde{C}_{i0}, \widetilde{\boldsymbol{U}}_{i0}) = \frac{N_{sys}}{N_{ST}} \frac{\eta_{G.K.}(\sum_{i=0}^{n} x_i)}{\prod_{i=0}^{n} \eta_{G.K.}(x_i)}. \tag{3.16}$$

Since $\eta_{G.K.}(x_i)$ can be calculated from Eqn. (3.2), $\eta_{E,T}$ can be derived from measured concentrations, N_{sys} and N_{ST}. Our experiments focus, therefore, on the study of $\eta_{E,T}$ at different flow rates, particle sizes, and geometries. As we will see later, the experimental results of different geometries show that the values of η_{Ei} are insensitive to the flow geometry for a sufficiently high Reynolds number even though the flow segment lengths are shorter than L_c.

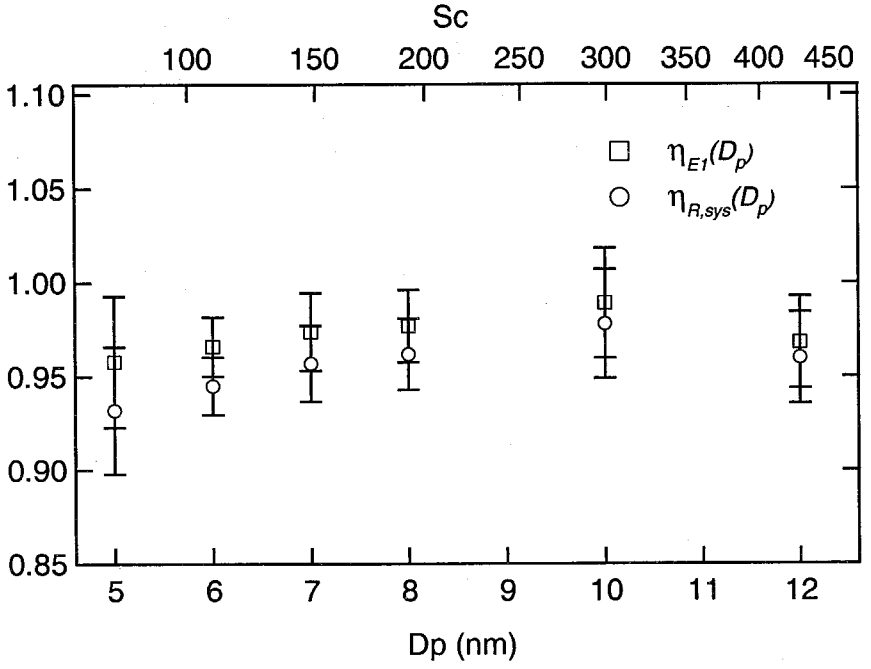

Figure 3.5: Measured $\eta_{R,sys}$ and η_{E1} for a system of two straight tubes joined by a single 90° bend. The volumetric flow rate is 1.052 L min^{-1} (Re = 251).

3.4 Experimental Results

Initial experiments were performed by measuring the particle concentrations, N_{sys} and N_{ST}, through both a system of two straight tubes joined by a single 90° bend versus a straight tube of the same total length. The two straight tubes were each of length 11.5 cm, joined by a 90° bend with 1.43 cm (9/16″) radius. The total length, including the bend, was 25 cm. The O.D. and I.D. of the tubes are 0.64 cm (0.25″) and 0.46 cm (0.18″), respectively. Figure 3.5 shows the relative system transmission efficiency, $\eta_{R,sys}$, and η_{E1} for particles from 5 nm to 12 nm diameters at a flow rate 1.052 L min^{-1} (Re = 251). $\eta_{R,sys}$ decreases with decreasing particle size, indicating the relative reduction in particle penetration efficiency when a 90° bend

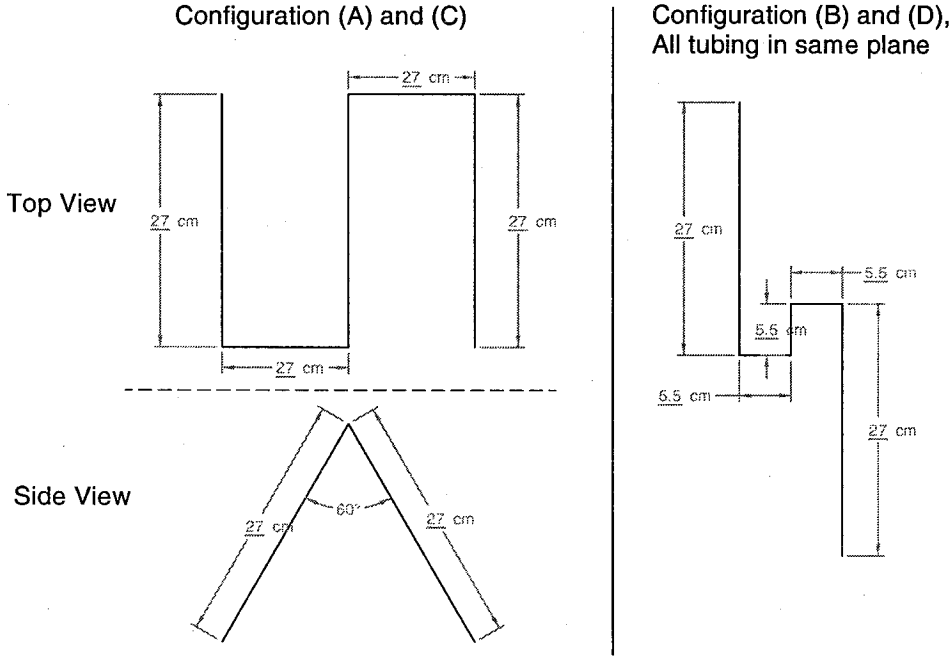

Figure 3.6: Tubes with different configuration (A)–(D). In (A) and (B), 90° bends are used to connect straight tubes while in (C) and (D), 1/4″ Swagelok™ elbows are used.

is present. Since smaller particles have larger diffusion coefficients, diffusional losses upstream of a bend reduce the concentration near the wall at the bend inlet. As a result, particle loss enhancement due to redistribution of the flow is more significant for smaller particles. For a single bend, both $\eta_{R,sys}$ and η_{E1} have large uncertainties since they must be deduced from small differences in particle concentrations between systems that differ only by the presence of a single 90° bend. To increase the effect of diffusional losses in order to improve the experimental accuracy, and at the same time, to examine the influence of specific geometry on the value of $\eta_{E,T}$, more complex geometries will now be considered.

Tubes with four different configurations, designated A-D, and illustrated in Fig.

3.6 were used to study the effects of 90° bends and *Swagelok*^{TM} elbows on particle penetration efficiency. Each configuration consists of five straight tubes. In configurations (A) and (C), the lengths of all straight tubes are identical, 27 cm; in (B) and (D), some straight tubes are as short as 5.5 cm. Copper tube was used to avoid the enhancement of deposition due to particle charge. The O.D. and I.D. of the copper tube are 0.64 cm (0.25″) and 0.46 cm (0.18″), respectively. In configurations (A) and (B), the straight tubes are connected by 90° bends with 1.43 cm (9/16″) radius, while 1/4″ *Swagelok*^{TM} elbows were used in (C) and (D). In (A) and (C), the length of the straight tubes, 27 cm, exceeds the flow entrance length at all Reynolds numbers studied, while in configurations (B) and (D), the length of straight tube, 5.5 cm, exceeds the flow entrance length only when Re < 200. Therefore, when Re > 200, the influence of recirculation strength on $\eta_{E,T}$ can be examined. Also, as shown in Fig. 3.6, the orientations between flow elements are different in (A) and (C) compared to that in (B) and (D). For each configuration, a reference measurement was also made with a straight tube that has the same total length (including straight tubes and 90° bends or *Swagelok*^{TM} elbows).

For each configuration, experiments along with straight tube reference measurements, were carried out using particles ranging from 5 nm to 15 nm diameter at various flow rates (flow Reynolds numbers). Fig. 3.7 shows $\eta_{R,sys}$ and $\eta_{E,T}$ for configurations (A) and (C) at flow rate 0.362 L min^{-1} (Re = 86). The uncertainties (2σ) of $\eta_{R,sys}$ and $\eta_{E,T}$ were derived from repeated measurements. The evaporation-condensation aerosol generator gives a peak concentration at aerosol diameter of 7 nm. Therefore the uncertainties of the results are the smallest at 7 nm and larger at other sizes as a result of lower signal to noise ratio. In configuration (A), straight tubes are connected by 90° bends, while *Swagelok*^{TM} elbows are used in configuration (C). Both 90° bends and *Swagelok*^{TM} elbows significantly decrease particle penetration efficiency in the 5–15 nm size range. For 5 nm diameter particles, the penetration efficiency through configurations (A) and (C) drops to 66% and 56%, respectively,

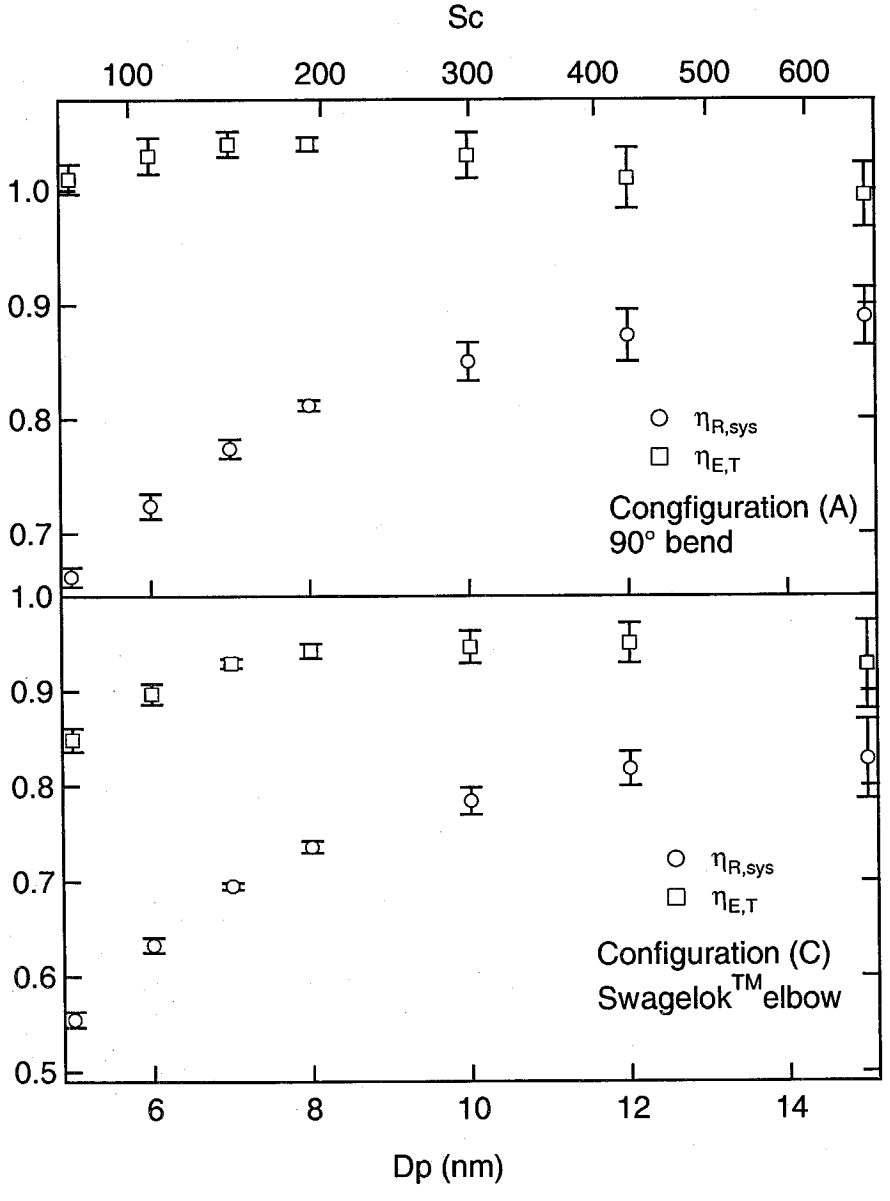

Figure 3.7: $\eta_{R,sys}$ (circle) and $\eta_{E,T}$(square) of configuration (A) and (C). The volumetric flow rate is 0.362 L min^{-1} (Re = 86). The O.D. and I.D. of the tubes are 0.64 cm (0.25″) and 0.46 cm (0.18″), respectively.

of that of a straight tube of the same total length. Even for 15 nm particles, the decrease in penetration efficiency exceeds 10% in both configurations. The results of configurations (A) and (C) show that replacing *Swagelok*^{TM} elbows with the 90° bends improves system particle penetration efficiencies for nanoparticles. Compared to the system relative transmission efficiency, $\eta_{R,sys}$, $\eta_{E,T}$ is much closer to unity in both configurations, especially in configuration (A). This suggests that treating the particle concentration profile as uniform at the inlet of each section provides a better estimate of the system penetration efficiency than treating the system as a straight tube of the same total length. This is true for all particle sizes (Sc), Re, and flow geometries studied in this work.

Figure 3.8 compares $\eta_{E,T}$ between configurations (C) and (D). Since *Swagelok*^{TM} elbows are used in both configurations, at the same particle size and flow rate, the two configurations have the same Re, Sc, and De. The difference lies in the length of straight tubes and orientation between elbows. The length of straight tubes in configuration (C), 27 cm, exceeds the flow entrance length at all Reynolds numbers studied. In configuration (D), the length of straight tube, 5.5 cm, is longer than the flow entrance length only when Re < 200. In both configurations, the concentration profiles are still developing before entering the *Swagelok*^{TM} elbows at all flow rates and particle sizes. At Re $= 86$, the values of $\eta_{E,T}(D_p)$ for the two configurations differ for particles with diameters of 5, 8, and 15 nm; at 5 nm, the difference is about 20%. Since the flows are fully developed before entering the elbows in both configurations at Re $= 86$, this suggests the difference is due to the different particle concentration profiles at the inlet of the elbows. When Re > 250, the differences of $\eta_{E,T}$ for the two configurations lie within statistical error except at Re $= 510$ for particles with diameters 5 and 8 nm. For both configurations, $\eta_{E,T}(D_p)$ increases with decreasing Re. This is because at small Re, recirculation inside the *Swagelok*^{TM} elbows is too weak to move substantial amounts of fluid from the center of the tube, where the particle concentration is highest, to near the wall.

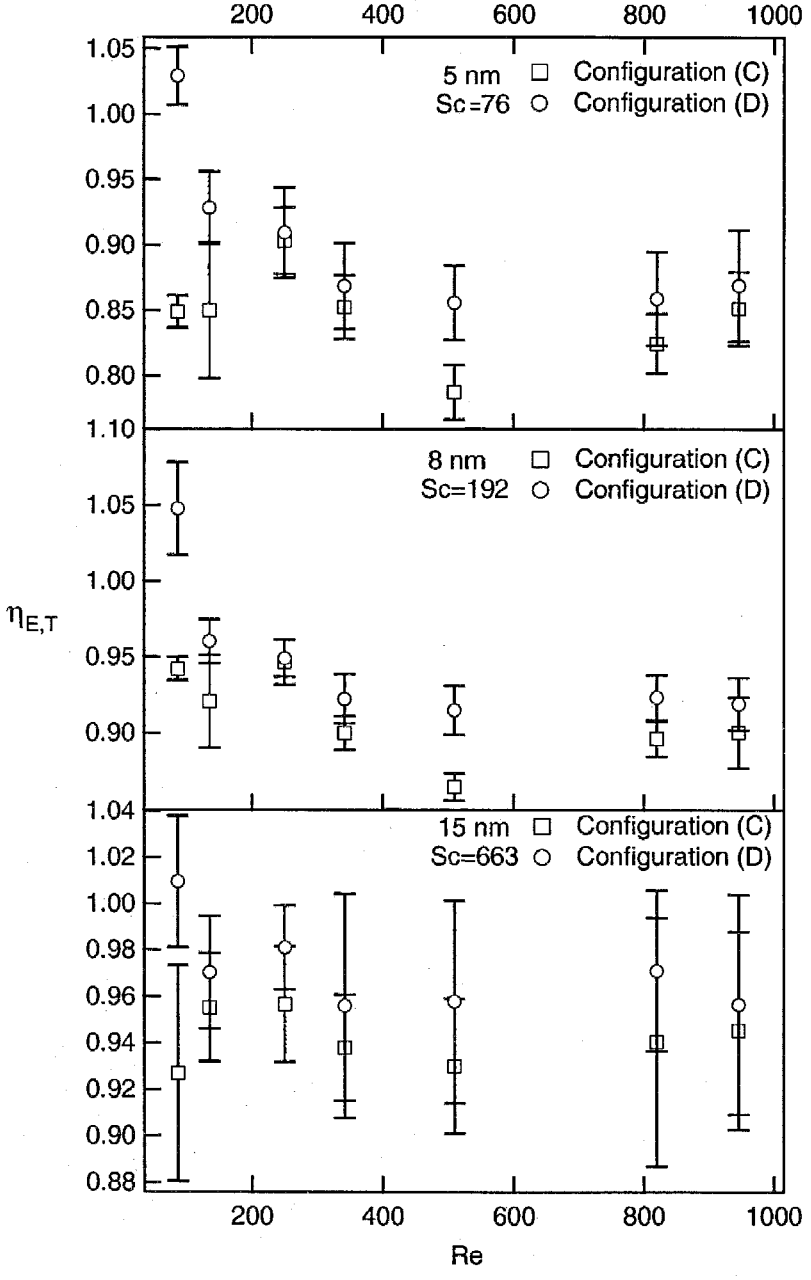

Figure 3.8: Measured values of $\eta_{E,T}$ for configurations (C) and (D) for different particle sizes (Sc) and flow Reynolds numbers.

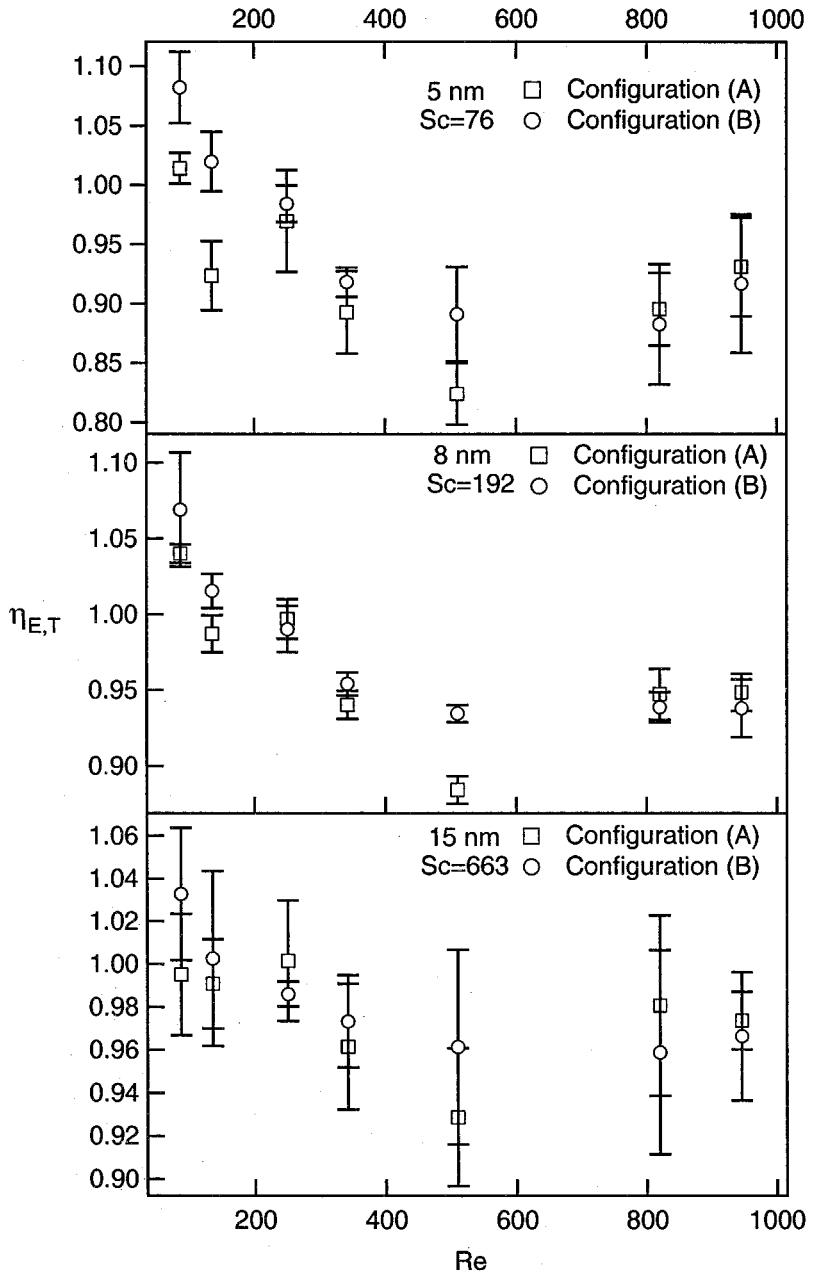

Figure 3.9: Measured values of $\eta_{E,T}$ for configurations (A) and (B) for different particle sizes (Sc) and flow Reynolds numbers.

Figure 3.9 compares the values of $\eta_{E,T}$ for configurations (A) and (B) at different particle sizes and flow Reynolds numbers. Similar to results of configurations (C) and (D), $\eta_{E,T}$ are different for configurations (A) and (B) when Re < 250. Also $\eta_{E,T}$ increases with decreasing Re. Comparing results in Figs. 3.8 and 3.9, we found that replacing *Swagelok*^{TM} elbows with 90° bends in aerosol sampling systems result in slightly higher values of $\eta_{E,T}$ and system particle penetration efficiency. The reason is that the *Swagelok*^{TM} elbow has a smaller bend radius, and higher Dean number at same flow Reynolds number, which leads to a more intensive recirculation inside the elbow and higher particle losses downstream the elbows.

Figure 3.9 shows when Re > 250, the values of $\eta_{E,T}$ for configurations (A) and (B) are statistically similar except at Re $= 510$. Since configurations (A) and (B) have different lengths of straight tubes and orientations between bends, the data suggest that η_E is insensitive to the system flow geometry when Re > 250. Therefore, we estimate η_E and its uncertainty $2\sigma(\eta_E)$ of the 90° bend in a general aerosol sampling system as

$$\begin{aligned}
\eta_E &= \frac{1}{2}\left[\left\{\max\left[\left(\prod_1^4 \eta_{Ei} + 2\sigma\right)_{(A)}, \left(\prod_1^4 \eta_{Ei} + 2\sigma\right)_{(B)}\right]\right\}^{\frac{1}{4}}\right. \\
&\quad \left. + \left\{\min\left[\left(\prod_1^4 \eta_{Ei} - 2\sigma\right)_{(A)}, \left(\prod_1^4 \eta_{Ei} - 2\sigma\right)_{(B)}\right]\right\}^{\frac{1}{4}}\right] \qquad (3.17) \\
2\sigma(\eta_E) &= \frac{1}{2}\left[\left\{\max\left[\left(\prod_1^4 \eta_{Ei} + 2\sigma\right)_{(A)}, \left(\prod_1^4 \eta_{Ei} + 2\sigma\right)_{(B)}\right]\right\}^{\frac{1}{4}}\right. \\
&\quad \left. - \left\{\min\left[\left(\prod_1^4 \eta_{Ei} - 2\sigma\right)_{(A)}, \left(\prod_1^4 \eta_{Ei} - 2\sigma\right)_{(B)}\right]\right\}^{\frac{1}{4}}\right], \qquad (3.18)
\end{aligned}$$

where $(\cdots)_{(A)}$ and $(\cdots)_{(B)}$ denote experimental results of the configuration (A) and (B), respectively. Similarly, the η_E and $2\sigma(\eta_E)$ of the 1/4″ *Swagelok*^{TM} elbow were

Table 3.1: Values of η_E and $2\sigma(\eta_E)$ for 90° bend with 1.43 cm (9/16″) radius. The O.D. and I.D. of the tube are 0.64 cm (0.25″) and 0.46 cm (0.18″), respectively.

Dp	Sc	Re				
(nm)		251	343	510	819	946
5	76	0.992±0.011	0.972±0.010	0.964±0.018	0.969±0.014	0.978±0.016
6	109	0.997±0.006	0.984±0.008	0.967±0.012	0.978±0.008	0.979±0.009
7	148	0.999±0.003	0.987±0.006	0.974±0.011	0.983±0.005	0.982±0.009
8	192	0.998±0.004	0.986±0.004	0.976±0.009	0.986±0.004	0.985±0.006
10	299	0.998±0.005	0.988±0.004	0.981±0.007	0.988±0.009	0.989±0.008
12	428	1.001±0.007	0.991±0.006	0.986±0.010	0.991±0.005	0.993±0.010
15	663	1.000±0.007	0.991±0.008	0.987±0.014	0.991±0.014	0.991±0.008

derived from experimental data of configurations (C) and (D). Tables 3.1 and 3.2 list η_E and $2\sigma(\eta_E)$ for the 90° bend and $Swagelok^{TM}$ elbow over the range of Re studied, respectively. The values of η_E are close to 1, as we discussed before. From Eqn. (3.14), we have,

$$\begin{aligned} \eta_{sys} &= \left[\prod_{i=0}^{n} \eta_{G.K.}(x_i)\right]\left[\prod_{i=1}^{n} \eta_{Ei}(\mathrm{Re}, \mathrm{Sc}, \mathrm{De}, x_i, \widetilde{C}_{i0}, \widetilde{U}_{i0})\right] \\ &\approx \left[\prod_{i=0}^{n} \eta_{G.K.}(x_i)\right](\eta_E)^n . \end{aligned} \tag{3.19}$$

For a particle sampling system of $n+1$ straight tubes connected by n 90° bends or $Swagelok^{TM}$ elbows, when $250 < \mathrm{Re} < 950$, the system penetration efficiency can be estimated by using Eqn. (3.19) and the η_E derived.

The data show that for the same Re, Sc, and De, the values of $\eta_{E,T}$ depend on flow geometry when $\mathrm{Re} < 250$, suggesting that it is not appropriate to use a calibration of one particle sampling system geometry to calculate particle penetration efficiency for another system geometry at low flow Reynolds number. When $\mathrm{Re} > 250$, the

Table 3.2: Values of η_E and $2\sigma(\eta_E)$ for 1/4″ Swagelok^{TM} elbow.

Dp (nm)	Sc	Re				
		251	343	510	819	946
5	76	0.977±0.009	0.964±0.010	0.953±0.017	0.959±0.013	0.965±0.012
6	109	0.979±0.004	0.967±0.009	0.960±0.012	0.966±0.010	0.967±0.009
7	148	0.983±0.002	0.973±0.009	0.966±0.010	0.969±0.010	0.973±0.009
8	192	0.986±0.004	0.978±0.007	0.972±0.010	0.977±0.007	0.976±0.008
10	299	0.990±0.004	0.982±0.007	0.977±0.009	0.979±0.009	0.981±0.007
12	428	0.990±0.009	0.986±0.007	0.981±0.009	0.983±0.007	0.985±0.010
15	663	0.991±0.009	0.989±0.012	0.987±0.013	0.986±0.016	0.988±0.013

results show that the values of $\eta_{E,T}$ are insensitive to the system flow geometry. By comparing $\eta_{E,T}$ to η_{sys}, we found when information of η_{Ei} is lacking, assuming uniform concentration profiles at inlets of each bend gives a much better estimate of system particle penetration efficiency than treating the system as a straight tube of the same total length. The data also show that replacing $Swagelok^{TM}$ elbows with 90° bends with larger bend radius results in higher values of $\eta_{E,T}$ and system particle penetration efficiencies.

3.5 Conclusions

An experimental investigation of additional losses due to 90° bends or $Swagelok^{TM}$ elbows has been undertaken. Experiments have been conducted using monodisperse particles in the 5 to 15 nm size range for tube-flow Reynolds numbers ranging from 80 to 950. The data suggest that secondary recirculation flows inside 90° bends and $Swagelok^{TM}$ elbows enhance diffusional deposition. In a flow passage with four

Swagelok^{TM} elbows , the observed penetration efficiency was as much as 44% lower than observed when a straight tube of the same length was employed. When Re < 250, the increases in particle losses depend on the geometry of the sampling system, i.e., the length of straight tube and orientations of bends and elbows, suggesting that for each instrument containing bends or elbows, an experimental calibration for nanoparticle penetration efficiency is necessary when Re < 250. When Re > 250, the values of $\eta_{E,T}$ are insensitive to the flow geometry. η_E of a 90° bend with 1.43 cm (9/16″) radius and 1/4″ *Swagelok*^{TM} elbow is derived from experiment results, which could be used for a general aerosol sampling system when Re > 250. The data also show the particle losses could be reduced by using 90° bends with large radius instead of *Swagelok*^{TM} elbows. When η_{Ei} is unknown, assuming uniform concentration profiles at inlet of each flow element gives much better estimate of system particle penetration efficiency than does treating the system as a straight tube of the same total length. Possible future work includes detailed numerical simulation of flow field and particle losses in sampling system containing bends with different bend angles and radius, and comparison between numerical simulations and experiment results.

3.6 Acknowledgement

This work was supported by the Office of Naval Research.

Chapter 4

A Differential Mobility Analyzer (DMA) System for Submicron Aerosol Measurements at Ambient Relative Humidity

Reference: Wang J., R.C. Flagan, and J.H. Seinfeld, A differential mobility analyzer (DMA) system for submicron aerosol measurements at ambient relative humidity, *Aerosol Sci. Technol.*, In press.

Abstract

A new differential mobility analyzer (DMA) system for measuring submicron aerosol size distribution at ambient relative humidity, with special attention to implementation on aircraft, is described. The system includes an active RH controller, a cylindrical differential mobility analyzer (CDMA), and a condensation particle counter. A cascade controller consisting of two PID modules maintains the RH inside the CDMA at ambient RH. The flows are controlled with feedback PID controllers, which compensate for the variation of pressure as the aircraft changes altitude. This system was integrated into the CIRPAS Twin Otter aircraft and used to measure ambient size distributions during the ACE-Asia experiment, carried out from March to May, 2001, in Japan.

4.1 Introduction

Aerosols play an important role in the climate system. They scatter and absorb radiation and influence the microphysical structure, lifetime, and amount of clouds. Quantifying the effect of atmospheric aerosols on the climate system requires knowledge of their physical size and chemical composition, as well as of their temporal and spatial variability. Aircraft have proven to be an effective platform for sampling atmospheric aerosol over a reasonably large spatial domain. Aircraft-based measurements have inherent constraints, however, such as limitations on instrument size, weight, and power. Measurements must be made rapidly while taking into account the changing pressure, temperature, and relative humidity. Aircraft-based measurements also suffer from biases that result from modifications occuring in the sampling system that brings atmospheric particles to the instrument. For size distribution measurements, modifications arise from both the aircraft sampling inlet and the difference between the ambient relative humidity (RH) and that inside the instrument itself.

As an air stream is sampled by an aircraft, the speed of the air stream must decrease from the aircraft cruise speed down to the flow rate appropriate for the instrument involved. The ram heating that results from this deceleration increases the temperature of the air stream. The temperature of the sampled air stream can be further changed from ambient temperature as a result of heat exchange between the air stream and the duct surrounding it. While the absolute humidity (g of water/kg of dry air) within the air stream is conserved as it is transported from the atmosphere into the instrument, any temperature changes make the RH inside the instrument different from that in the air outside of the aircraft. For hygroscopic particles, this RH change can lead to a significant bias in size measurement. Some previous investigations in which submicron aerosols have been measured from aircraft are listed in Table 4.1. In most of these studies, the aerosol was dried by a diffusion drier or by heating prior to measurement. Back-calculation of the true ambient size distribution from a dry

measurement requires detailed knowledge of the chemical composition of the aerosol. Such information has generally not been available, at least at the spatial and size resolution required.

Table 4.1: Comparison of size ranges, platform, and RH conditions of airborne instruments for measuring submicron aerosol size distributions.

Reference	Platform	Diameter range	Instrument RH
Brock et al. (1989) [7]	UW C131a	0.010-1.0μm	Dry
Hegg et al. (1993) [28]	UW C131a	0.020-0.6μm	Dry
Hudson and Clarke (1992) [32]	NCAR Electra	0.020-0.6μm	Dry
Russell et al. (1996) [58]	UW C131a	0.005-0.2μm	Dry
This work	CIRPAS Twin Otter	0.015-1.0μm	Ambient RH

A system capable of measuring aerosol size distributions at ambient RH, especially from aircraft platforms, has long been a major need. In this work, we report an automated differential mobility analyzer (DMA) system for aircraft-based measurements of atmospheric aerosol at ambient RH, a key element of which is an active RH controller that maintains the RH inside the DMA at the ambient RH by adding or removing water vapor from the air stream. The system was tested and deployed during the ACE-Asia experiment carried out during March-May, 2001, in Japan. Data regarding the performance of the system, and measured size distributions, are presented.

4.2 Instrument Design

Figure 4.1 illustrates the system. Its main components are an active RH controller, a ^{210}Po aerosol neutralizer [58], a cylindrical differential mobility analyzer (CDMA,

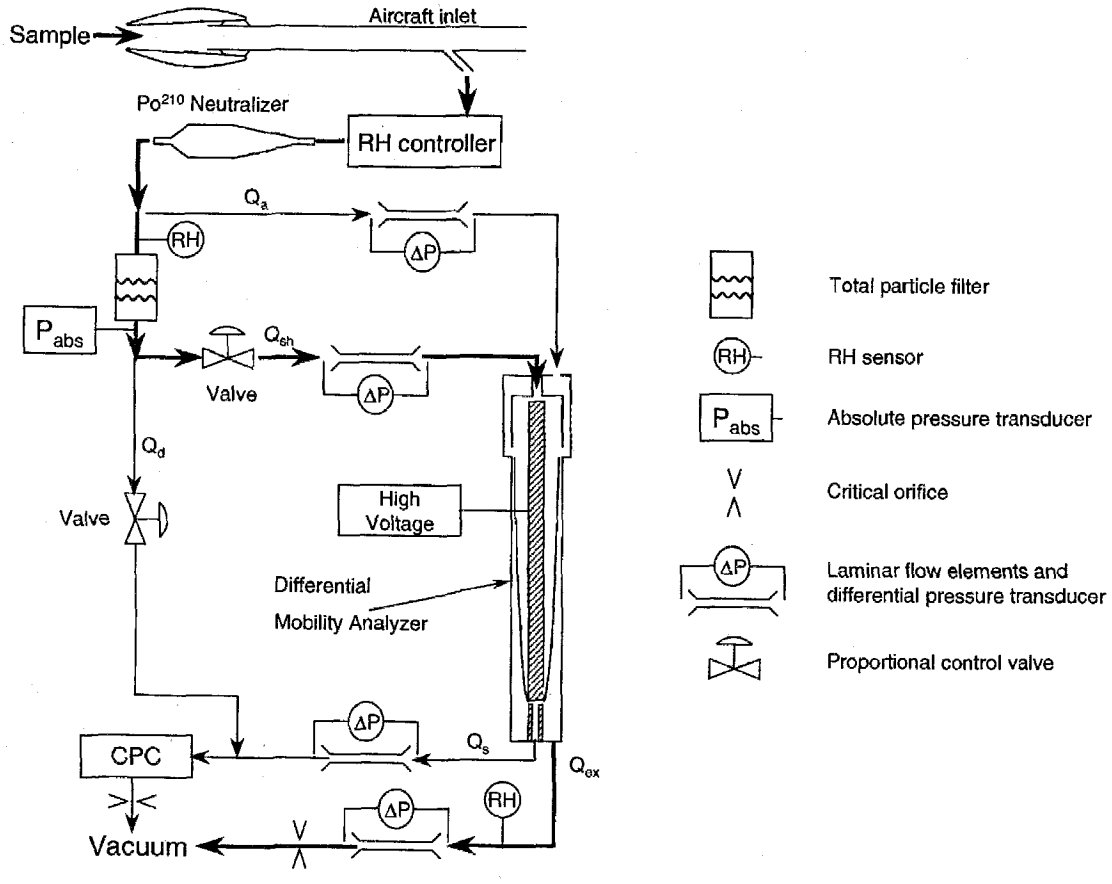

Figure 4.1: Configuration and components of the DMA system.

TSI, model 3081), and a condensation particle counter (TSI model 3010). The CDMA measures particles with diameters from 15 nm to 1 μm. Using the scanning mobility technique [79], the system is capable of generating a size distribution every 90 s. In the particular application to be discussed below, the air flow was drawn directly from the aircraft inlet at a rate of 2.85 L min^{-1}.

4.2.1 RH Control

An active RH controller was developed to maintain the RH inside the instrument

at ambient RH. Because of the speed of the aircraft, the RH controller must respond rapidly to changing ambient RH. A cascade controller consisting of two PID control modules was used to meet this requirement. A schematic of the RH controller is shown in Figure 4.2.

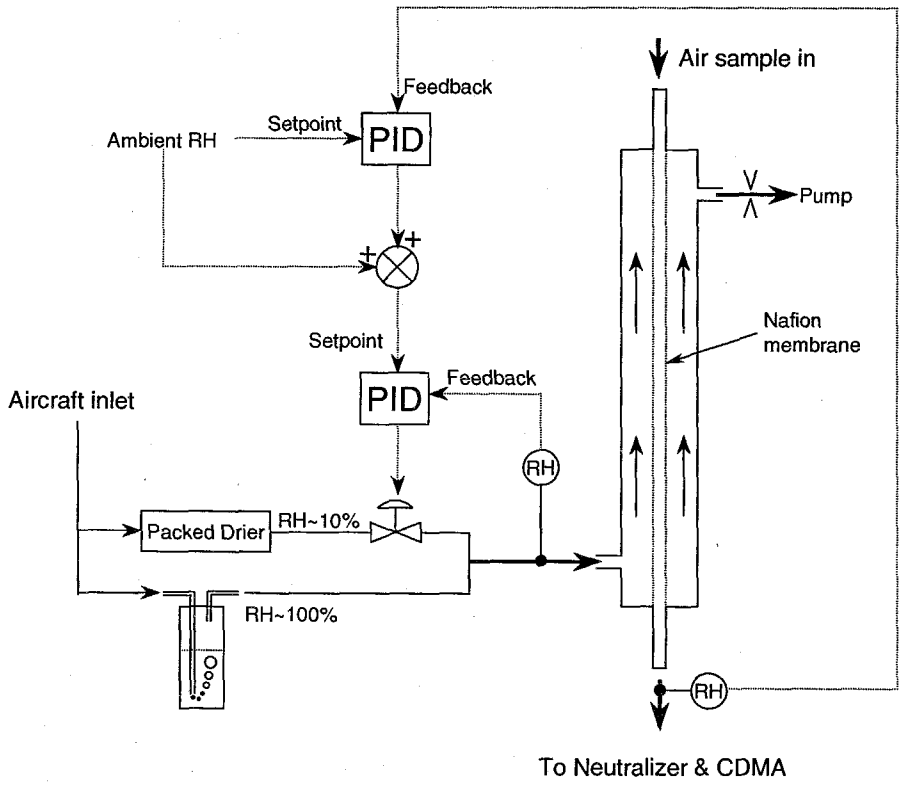

Figure 4.2: Schematic of the active RH controller.

The RH controller consists of a moisture exchanger (PermaPure, model PD07018T-12SS), two RH sensors (Vaisala model Humitter50Y), and one proportional control valve. The moisture exchanger is made of 18 Nafion® membrane tubes housed within a stainless steel shell. Nafion is a hygroscopic ion exchange membrane that selectively absorbs water. Given sufficient time, the partial water vapor pressures of both sides of the Nafion membrane reach equilibrium. In the moisture exchanger, the air sample

flows within the Nafion tubes. The RH of the air sample is controlled through adjusting the RH of a countercurrent purge flow that is introduced between the Nafion tube and the shell. A cascade controller consisting of two PID modules was used. The first PID module takes the ambient RH as the setpoint and the RH of the air sample exiting the Nafion tubes as the feedback. The sum of the output of the first PID module and the ambient RH serves as the setpoint of the second PID, which controls the RH of the purge flow. The purge flow is a mixture of two flow streams. One is the dry flow generated by passing the air stream through a packed drier; the other is humidified to near saturation by passing through a water bottle. The RH of the air streams after the drier and the water bottle are about 10% and 100%, respectively. The total purge flow rate is set at 12 L min^{-1} by a critical orifice. The RH of the purge flow is controlled through a proportional valve that varies the mixing ratio of the two air streams. The advantage of the cascade controller is described below. The Nafion membrane tries to equalize the partial water vapor pressures, in our application, RH, on its two sides. As a result, the RH of the purge flow to maintain the air sample at ambient RH is close to the ambient RH. We write the setpoint of the purge flow RH, RH_p as

$$RH_p = RH_{amb} + \Delta RH, \tag{4.1}$$

where RH_{amb} is the ambient RH. ΔRH, which is the output of the first PID module, represents the difference between the purge flow RH setpoint and the ambient RH. ΔRH is not zero due to the water vapor exchange between the purge flow and the sample flow in the Nafion moisture exchanger. Compared to RH_p, which varies according to RH_{amb}, the ΔRH changes more slowly, especially when RH_{amb} changes rapidly. By controlling a slow changing ΔRH, the cascade controller yields better control performance. Preliminary experiments confirmed that the cascade control algorithm represents a significant improvement over conventional single PID control, especially in the presence of rapidly changing ambient RH. The active RH controller can operate from 10%–90% RH, but the response time of the system varies over this

range. The water content of the Nafion ion exchange membrane varies dramatically with RH. The response time varies because of the dynamics of water uptake by the Nafion ion exchange membrane. Each sulfonic acid group in the Nafion absorbs up to 13 molecules of water. The water content of fully hydrated Nafion is 22% by weight. Large changes in the water content of the membrane slow the adjustment of the output humidity of humidity control system. When the relative humidity falls below about 25%, the pore size decreases, limiting the permeability of the membrane, again slowing the response [52]. At either extreme, using Nafion tubes with thinner walls would minimize the response time due to absorption/desorption of water. With the Nafion tubes that are commercially available at the present time, the dynamic response is fastest for relative humidity between about 25% and 75%, and slows substantially when the humidity is outside this range or the change is large. Once the Nafion membrane equilibrates, the time response to small perturbations recovers. To monitor the potential RH change after the RH controller, a third RH sensor is installed to measure the RH of DMA excess flow, which is compared with the RH of the flow exiting the RH controller.

4.2.2 Flow Control

As shown in Figure 4.1, the flow exiting the RH controller is first introduced to a ^{210}Po neutralizer, which brings the aerosol to a steady-state bipolar charge distribution. The flow is then divided into three streams: the aerosol, sheath flows for the CDMA (Q_a and Q_{sh}, respectively), and the dilution flow to the CPC (Q_d). A HEPA filter removes particles in the sheath and dilution flows. The critical orifice in the CPC controls the flow through that instrument at 1 L min^{-1}. A critical orifice was also used to control the excess flow (Q_{ex}) exiting the main outlet of the CDMA at 1.85 L min^{-1}. Initial tests employed control valves in place of the critical orifices to reduce the power consumption, but the flow stability was deemed inadequate. This

was traced to pressure transducers that produced noisier signals than previous units of the same model. The critical orifices circumvented this problem, but for applications that limit power consumption, particularly when the DMA is operated at higher flow rates, active flow control would be preferred over critical orifices. The sample flow (Q_s) that carries classified particles with narrow mobility range is mixed with particle-free dilution flow and measured by the CPC. All four flows associated with the CDMA are monitored constantly by measuring the pressure drops across laminar flow elements with electrical differential pressure transducers(Validyne). This configuration allows the system to respond to deviations of flow rate from the setpoint that result from changes in sampling conditions. Deviations of flows are used as feedback for two independent PID controllers. One maintains a constant CDMA inlet flow ratio while the other a constant outflow ratio:

$$\frac{Q_a}{Q_{sh}} = 0.1 \tag{4.2}$$

$$\frac{Q_s}{Q_{ex}} = 0.1 \tag{4.3}$$

The flows are also constrained by three steady-state relationships. Two of these are set by critical orifices:

$$Q_{ex} = 1.85 \text{ L min}^{-1} \tag{4.4}$$

$$Q_s + Q_d = 1.0 \text{ L min}^{-1} \tag{4.5}$$

The third steady state relationship is derived from the steady-state mass balance for the CDMA flows:

$$Q_a + Q_{sh} = Q_s + Q_{ex} \tag{4.6}$$

The five relationships given above fix the five flows at following values:

$$Q_a \;=\; Q_s = 0.185 \text{ L min}^{-1}$$

$$\begin{aligned} Q_{sh} &= Q_{ex} = 1.85 \text{ L min}^{-1} \\ Q_d &= 0.815 \text{ L min}^{-1} \end{aligned} \tag{4.7}$$

Because of the linear relationship between flow and pressure drop across the laminar flow elements, this algorithm results in a constant flow ratio within 1% over the range of operation. Fast measurements are made by classifying particles in an electric field that varies exponentially with time, the so-called scanning electrical mobility spectrometer (SEMS, [79]). A high resolution D/A card (16 bit, National Instruments) is used to provide a 0-10 V control signal that drives the high voltage unit (Bertran 605C-100N), which has a range of 10-10000 V. The high voltage output from the unit is monitored through a built-in voltage divider and a high resolution A/D card (16 bit, National Instrument).

4.2.3 Software and Data Reduction

Software to drive each of the components of the system and to record data from each of them was written in Labview (National Instrument). Digital and analog data acquisition is through a 16-channel A/D card (National Instrument, PCI6034E). The measured signals are used to calculate the control signals for the proportional control valves and the high voltage unit. The control signals are sent out through a D/A card (National Instrument, PCI6703). The software simultaneously monitors the flow rates, relative humidities, pressures, and temperatures, and writes them into a file at the end of each size distribution measurement. The status of the CPC (e.g., the temperature of saturator and condenser) and the particle counts detected by the CPC during 1 s intervals are transmitted from the CPC to the computer through a RS232 connection and saved into a file. A real-time display shows the flow rates, temperatures, and raw data counts, which are updated every second.

A DMA data inversion program [16], which provides the options of inverting the

data in real time, i.e., immediately after each size distribution measurement, was incorporated into the control software. Regardless of whether real-time data display is enabled, the raw data are saved for off-line analysis. The main features of the inversion method include removing the smearing effect associated with the residence time distributions within the CPC [16], using a diffusionally broadened DMA transfer function, and providing the option to use one of several inversion routines depending on the specifics of the measurement.

4.3 In-Flight Instrument Performance

The DMA system described above has been integrated into the CIRPAS [6] Twin Otter research aircraft. In one configuration, the water bottle was removed from the RH controller to use dry air as the purge flow. The modified system measures the dried aerosol size distribution, which is compared to the ambient size distribution measured by the second system.

During the ACE-Asia experiment, 19 flights of the Twin Otter were conducted based out of Iwakuni Marine Corps Air Station, Japan. We report here on the performance of the instrument in measurement of submicron aerosol size distributions at ambient RH during these flights, and on the difference between simultaneous dry and ambient RH measurements. For this purpose, conditions in the instrument were carefully monitored. Since the system samples directly from the aircraft inlet, the pressure inside the CDMA varies as the aircraft changes altitude. The feedback control in the instrument maintains ratios Q_a/Q_{sh} and Q_m/Q_{ex} constant so that the shape of the DMA transfer function, and hence the size resolution of the size measurement, is maintained. The effectiveness of the feedback control is illustrated in Figure 4.3, in which the flow rates during a gradual ascent through the boundary layer on April 17, 2001, are shown.

When the absolute pressure within the system changes due to descent or ascent of the aircraft, the air within the CDMA expands or contracts, which results in a net inflow or outflow from the CDMA. Two independent PID controllers maintain the ratios Q_a/Q_{sh} and Q_m/Q_{ex} constant, thereby maintaining the shape of the CDMA transfer function during the transition period. The imbalance of the flow invalidates Equation 4.6 and leads to deviation of flow rates from their setpoints. As a result, the transfer function shifts in mobility space. The magnitude of this shift is now estimated.

According to the ideal gas law,

$$PV_{DMA} = nRT, \tag{4.8}$$

where V_{DMA} is the volume inside the CDMA, and n is the number of moles of air inside the CDMA. Assuming the system temperature remains constant during the transition period, the change of n due to pressure change can be written as

$$dn = \frac{V_{DMA}}{RT} dP \tag{4.9}$$

From the ideal gas law,

$$dV = \frac{RT}{P} dn \tag{4.10}$$

Combining Equations 4.8 and 4.10, the net volumetric flow into the DMA, Q_{net} can be written as

$$Q_{net} = \frac{dV}{dt} = \frac{RT}{P}\frac{dn}{dt} = \frac{V_{DMA}}{P}\frac{dP}{dt} = \frac{V_{DMA}}{P}\frac{dP}{dZ}\frac{dZ}{dt}, \tag{4.11}$$

where Z is the altitude, and dZ/dt is the climb or descent rate.

For flights during the ACE-Asia experiment, the climb and descent rates usually did not exceed 300 m min^{-1}. On this basis, Q_{net} is estimated to be smaller than 0.015 L min^{-1}, which is less than 1% of the total inlet or outlet flow of CDMA. Therefore,

the shift of the DMA transfer function in mobility space can be neglected as long as the ratios Q_a/Q_{sh} and Q_m/Q_{ex} are maintained. Figure 4.3 shows all flow rates are maintained during the ascent, indicating the system is able to adjust rapidly to the pressure changes.

Figure 4.4 shows the result of RH control on April 25, 2001, during sampling a layer at an altitude of 3000 m. The variation of RH within the layer was relatively small. As demonstrated in Figure 4.4, the RH controller successfully maintained the RH inside the DMA at its ambient level. Figure 4.5 shows similar results for the flight on April 17, 2001. In contrast to the flight of April 25, the RH changed rapidly as the aircraft sampled different layers. The RH controller tracked the ambient RH well most of the time, although the controlled RH in the CDMA lagged behind the ambient level after abrupt RH excursions. As previously noted, the Nafion membrane response slowly to large changes in the purge flow RH, especially when the RH suddenly increased above 75% or fell below 25%. For all 19 flights carried out during ACE-Asia, the differences between RH measured upstream and downstream of the CDMA were less than 5%, indicating a small change in RH downstream of RH controller.

Figure 4.6 shows measured dry and ambient boundary layer aerosol size distributions during the flight on April 25, 2001. The size distributions measured during a constant altitude leg at 320 m from UTC 3:17 to 4:00 are averaged over that period. The ambient RH of this layer is $77\% \pm 4\%$. Compared to the dry size distribution, the ambient distribution is shifted significantly toward larger sizes, suggesting a substantial fraction of hygroscopic aerosols in the size range measured.

4.4 Acknowledgements

The authors extend special appreciation to the CIRPAS crew for their help in integrating the DMA system into Twin Otter aircraft: Haflidi Jonsson, Bob Rogell,

Dennis Hamaker, Nava Roy, and Roy Woods. This work was supported by the Office of Naval Research.

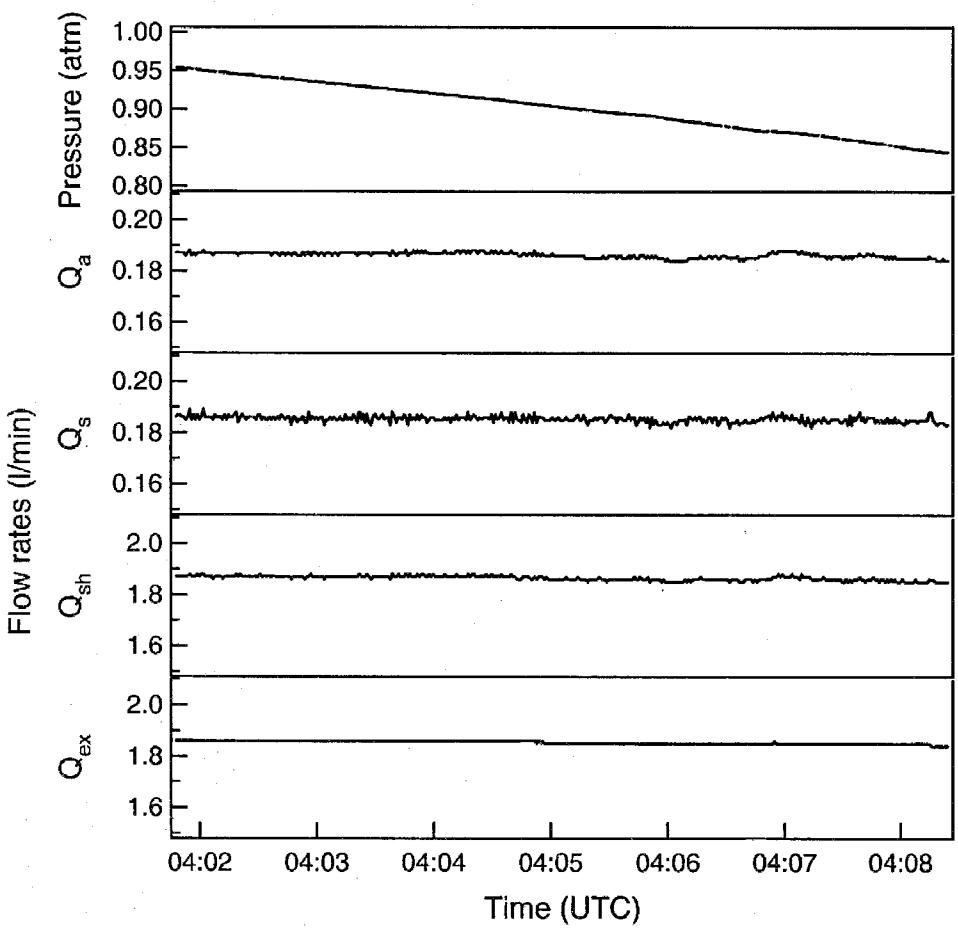

Figure 4.3: CDMA flow rates and pressure change during a gradual ascent through the boundary layer in East China Sea on April 17, 2001.

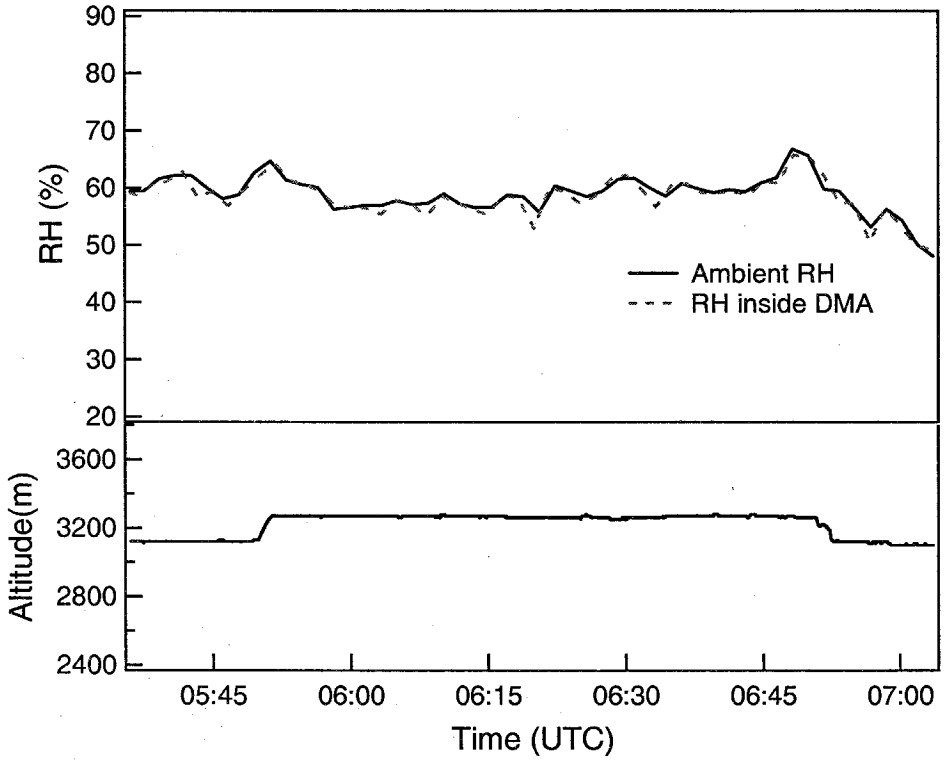

Figure 4.4: Comparison of instrument and ambient RH during sampling of layer at 3000 m altitude south of Shikoku Island, Japan on April 25, 2001.

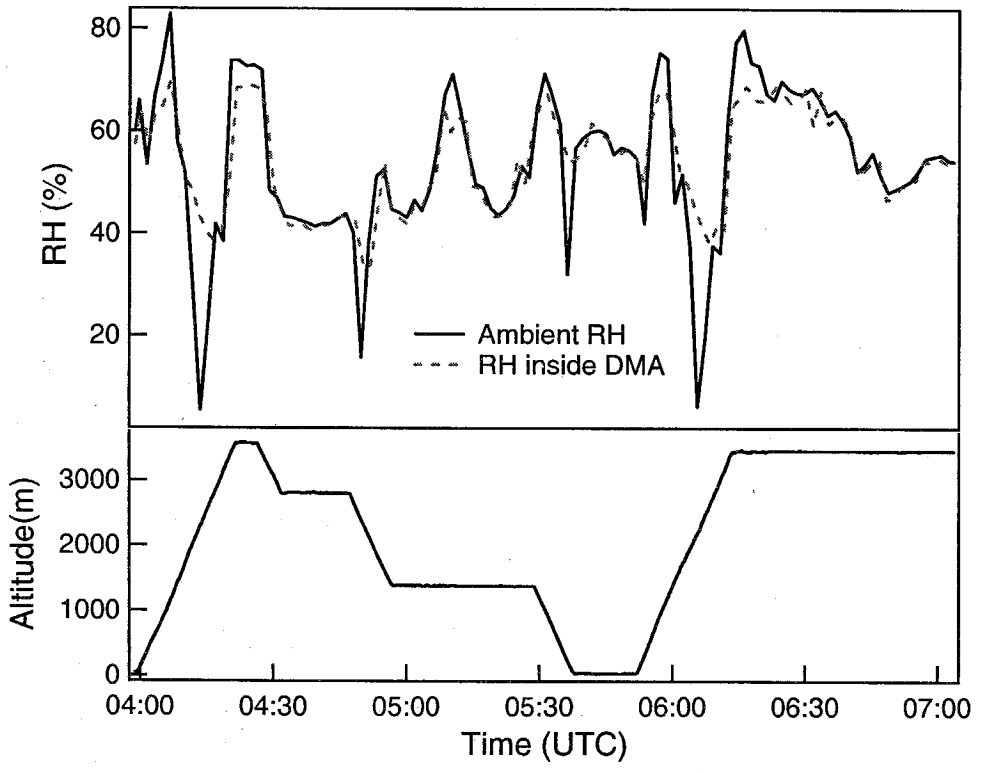

Figure 4.5: Comparison of instrument and ambient RH during flight in East China Sea on April 17, 2001.

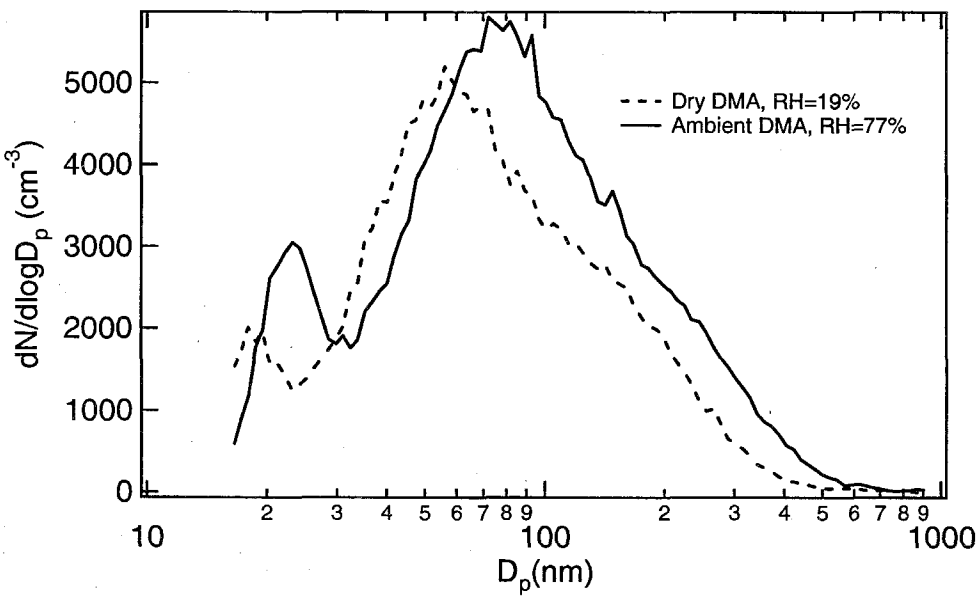

Figure 4.6: Dry and ambient size distributions measured at 320 m altitude during UTC 3:17 to 4:00, on April 25, 2001. Ambient RH is $77\% \pm 4\%$.

Chapter 5

Clear-Column Radiative Closure During ACE-Asia: Comparison of Multiwavelength Extinction Derived from Particle Size and Composition with Results from Sunphotometry

Reference: Wang J. et al., Clear-column radiative closure during ACE-Asia: comparison of multiwavelength extinction derived from particle size and composition with results from sunphotometry, *J. Geophys. Res.*, In press.

Abstract

From March to May 2001, aerosol size distributions and chemical compositions were measured using differential mobility analyzers, an aerodynamic particle sizer, Micro-Orifice Uniform Deposit Impactors, and denuder samplers on-board the Twin Otter aircraft as part of the ACE-Asia campaign. Of the 19 research flights, measurements on 4 flights that represented different aerosol characteristics are analyzed in detail. Clear-column radiative closure is studied by comparing aerosol extinctions predicted using in situ aerosol size distribution and chemical composition measurements to those derived from the 14-wavelength NASA Ames Airborne Tracking Sunphotometer (AATS-14). In the boundary layer, pollution layers, and free troposphere with no significant mineral dust present, aerosol extinction closure was achieved within the estimated uncertainties over the full range of wavelengths of AATS-14. Aerosol extinctions predicted based on measured size distributions also reproduce the wavelength dependence derived from AATS-14 data. Considering all four flights, the best-fit lines yield predicted/observed ratios in boundary and pollution layers of 0.96 and 1.03 at $\lambda = 525$ nm, and 0.94 and 1.04 at $\lambda = 1059$ nm, respectively. In free troposphere dust layers, aerosol extinctions predicted from the measured size distributions were generally smaller than those derived from the AATS-14 data; the predicted/observed ratios are 0.65 and 0.66 at 525 nm and 1059 nm, respectively. A detailed analysis suggests that the discrepancy is likely a result of the lack of the knowledge of mineral dust shape, as well as variations in aerosol extinction derived from AATS-14 data when viewing through horizontally inhomogeneous layers.

5.1 Introduction

Quantifying the effect of atmospheric aerosols on the climate system requires knowledge of their physical, chemical, and optical properties, as well as of their temporal and spatial variability. ACE-Asia was designed to study the aerosol in the atmosphere of East Asia, one of the Earth's most significant and complex anthropogenic aerosol sources. With widespread fossil fuel and biomass burning, coupled with large outbreaks of mineral dust, the atmospheric aerosol leaving the Asian continent is, arguably, the most complex on Earth. Through simultaneous measurement of aerosol microphysical, chemical, and radiative properties from a variety of platforms, the ACE-Asia campaign provided data to assess the climate impact of Asian aerosol.

A fundamental question that underlies prediction of aerosol climatic effects is how accurately aerosol radiative properties can be predicted based on measured in situ microphysical and chemical properties. If it can be demonstrated that columnar aerosol extinction and other radiative properties (e.g., absorption, angular distribution of scattering) can be accurately predicted given the knowledge of atmospheric aerosol size and composition, then models that predict these properties can be confidently used to predict climatic effects of aerosols. This so-called radiative closure has been attempted with varying degrees of success in several field campaigns using a variety of overdetermined measurements and modelling techniques [14, 30, 29, 31, 55, 17]. ACE-Asia was planned to provide an unprecedented opportunity to perform aerosol radiative closure studies from a number of platforms. This paper focuses on radiative closure between the aerosol extinction calculated using in situ measurements of aerosol size distributions and chemical compositions aboard the CIRPAS Twin Otter aircraft and those derived from the 14-wavelength NASA Ames Airborne Tracking Sunphotometer (AATS-14), which flew on the same aircraft.

ACE-Asia was conducted in East Asia from late March to early May, 2001. Intensive field measurements were conducted off the coast of east China, Korea, and Japan.

A detailed description of the campaign is given by Huebert et al. (2002) (overview paper, [33]). The CIRPAS Twin Otter flew 19 scientific missions out of Iwakuni Marine Corps Air Station, Japan. Four of those missions sampling different air masses provided ideal conditions for detailed analysis of predicted and observed clear column aerosol extinction, and we address these four cases in detail in the present paper.

5.2 Aerosol Size Distribution Measurements

The suite of instruments related to this study, which are deployed on the Twin Otter, are listed in Table 5.1. Measurements and data reduction for each instrument are described in detail in this section. Because it is essential to assess the uncertainty associated with the eventual radiative closure, and because some of that uncertainty results from uncertainties in the aerosol size and composition measurements, we devote attention to a careful analysis of the measurements on which the radiative closure is based.

5.2.1 Differential Mobility Analyzer (DMA)

Two differential mobility analyzer (DMA) systems, operated in parallel inside the main cabin of the Twin Otter, were deployed during ACE-Asia [78]. One of the two systems measures the dry aerosol size distribution by passing the aerosol flow through a Nafion dryer prior to the measurement. The other measures the aerosol size distribution at ambient relative humidity (RH) by using an active RH controller, which maintains the RH of the aerosol flow at ambient level by actively adding or removing water vapor from the flow [78]. The size measurement sections of the two systems downstream of the drier and active RH controller are identical. The main components of the measurement section are a cylindrical DMA (TSI Inc.,

Table 5.1: Measurements made on board the Twin Otter that are related to this study.

Property measured	Size range	Instrument	Time resolution
Aerosol microphysics			
Aerosol size distribution	0.015-1 μm	Differential mobility analyzer system	100 s
Aerosol size distribution	0.5-20 μm	Aerodynamic particle sizer	20 s
Aerosol hygroscopicity	0.040-0.6 μm	Tandem DMA system	20 min
Aerosol composition			
Inorganic anions, elements	< 3 μm	MOUDI sampler	30 min - 1 h
OC, EC	< 2.3 μm	Denuder sampler	30 min - 1 h
Optical property			
Aerosol optical depth		14-wavelength sunphotometer	4 s
Aerosol scattering coefficient		TSI 3563 nephelometer	1 s
Meteorological measurement			
Pressure, temperature, and RH		Various	1s

model 3081) and a condensation particle counter (TSI Inc., model 3010), which has a 50% counting efficiency at 10 nm. All the flows associated with the DMA are monitored and maintained by feedback controllers to compensate for environmental changes during airborne measurement. Using the scanning mobility technique, each DMA system generates a size distribution from 15 nm to 1 μm diameter every 100 s. Both DMA systems were carefully calibrated prior to and during ACE-Asia, and accurately recovered both the peak size and number concentration of monodisperse calibration aerosols as small as 30 nm diameter. The aerosol sample flows for the DMA systems were drawn from the Twin Otter community inlet, which was shared by other instruments in the main cabin. For the particle size range measured by the DMA systems (diameters smaller than 1 μm), the aerosol transmission efficiency through the community inlet has been established to be 100%. Data from DMA systems were analyzed using the data inversion procedure described by Collins et al. (2002) [16].

5.2.2 Aerodynamic Particle Sizer (APS)

An aerodynamic particle sizer (APS, TSI model 3320), which has a measurement range of 0.5 μm to 20 μm in aerodynamic diameter, was mounted under the left wing of the Twin Otter. The APS infers particle size by measuring the velocity of particles inertially accelerated in an expanding air stream; large particles undergo smaller acceleration and achieve lower velocity than small particles. Note that the APS does not measure the traditional aerodynamic particle size, for reasons that are explained below.

Independent of the sampling pressure, i.e., aircraft altitude, the velocity of expanding air downstream of the APS nozzle reaches 150 m/s. The particle Reynolds number inside the acceleration region is defined as

$$\mathrm{Re_p} = \frac{\rho_\mathrm{g} D_\mathrm{p} (V_\mathrm{g} - V_\mathrm{p})}{\eta}, \tag{5.1}$$

where ρ_g is the density of air, $D_\mathrm{p} = \sqrt[3]{\frac{6V}{\pi}}$ is the particle volume-equivalent diameter, where V is the volume of the particle. V_g is the air speed in the instrument, V_p the speed of the accelerated particle, and η the viscosity of air. For polystyrene latex (PSL) particles with diameters of 1.0, 2.1, 5, and 15 μm, the corresponding values of $\mathrm{Re_p}$ in the acceleration region are 0.65, 4.8, 24, and 103, respectively [77]. Therefore, the interaction of the particle and the surrounding air often lies well outside the Stokes regime ($\mathrm{Re_p} < 0.05$). Under the ultra-Stokesian condition ($\mathrm{Re_p} > 0.05$), the particle speed after acceleration is a function of particle aerodynamic size as well as the density of the particle [4, 80]. In an attempt to quantify the effect of particle density on APS measurement, Wang and John (1987) [77] found that within the resolution of the instrument, inside the detection volume, two particles with the same velocity, i.e., the same APS response, have the same acceleration. This finding enables accurate interpretation of APS measurements provided with calibration data. Cheng

et al. (1990) [10] generalized the analysis to include particle shape and slip correction factor. For two particles with the same APS response, the following relationship holds:

$$\left[\frac{\kappa(1+a_2\mathrm{Re}_{\mathrm{p}2}^{b_2})}{\rho_{\mathrm{p}2}D_{\mathrm{p}2}^2C(D_{\mathrm{p}2})}\right]_2 = \left[\frac{(1+a_1\mathrm{Re}_{\mathrm{p}1}^{b_1})}{\rho_{\mathrm{p}1}D_{\mathrm{p}1}^2C(D_{\mathrm{p}1})}\right]_1, \tag{5.2}$$

where subscript 1 denotes the calibration particle (In the present case, spherical PSL particles, density = 1.05 g/cm^3), and subscript 2 denotes the particle of interest. ρ_{p} is the particle density, C the slip correction factor, κ the dynamic shape factor, and $(1+a\mathrm{Re}^b)$ the ultra-Stokesian correction factor. For a spherical calibration particle, $\kappa = 1$, $a = 1/6$, and $b = 2/3$. The slip correction factor and the Reynolds number are evaluated at the APS sensing volume, which has a lower pressure and temperature than the ambient condition as a result of the expansion of the air stream. Given the calibration particle diameter, $d_{\mathrm{v}1}$, and its density, $\rho_{\mathrm{p}1}$, the volume-equivalent diameter of the measured particle, $d_{\mathrm{v}2}$, can be derived using Eqn. (5.2) with knowledge of its density, $\rho_{\mathrm{p}2}$, the dynamic shape factor, κ, and the ultra-Stokesian correction $(1 + a_2\mathrm{Re}_{\mathrm{p}2}^{b_2})$.

The density of the measured particle is calculated using the size-resolved particle chemical composition, together with its water content, which is calculated using the gas-aerosol thermodynamic model, ISORROPIA [50]. The details of the density calculation are described subsequently. In this study, particles are assumed to be spherical, a reasonable assumption for hygroscopic aerosols in the marine boundary layer, where most often the aerosols are deliquesced as a result of high relative humidity. For particles at low RH and nonhygroscopic particles, such as mineral dust, the assumption of sphericity does not necessarily hold. Lack of knowledge of dust particle shape as well as its dynamic shape factor κ, and the ultra-Stokesian correction factor $(1 + a_2\mathrm{Re}_2^{b_2})$, is a source of uncertainty in APS measurements. Uncertainties in the aerosol extinction calculation resulting from the assumption of spherical particles is estimated by using data on nonspherical agglomerate particles measured by Cheng

et al. (1993) [11].

The APS occasionally detects recirculating particles within the detection region, leading to so-called artificial particles. The particles involved are generally small in size but, due to recirculation, cross the detection laser beams multiple times with a reduced speed. As a result, when this occurs, these small but slow particles are misinterpreted as large particles. While on a number concentration basis, these artificial particles represent only a very small fraction of the total particles detected, because these particles are interpreted as large (> 5 μm), this could introduce significant errors into an aerosol extinction calculation. These artificial particles can be removed by applying a matrix data mask to the correlated APS data, which is a simultaneous measurement of the particle speed and scattering intensity as they cross the laser beams. Based on the principle that large particles scatter more light than small particles, a particle sized to be large (slow speed) but associated with little light-scattering is identified as artificial and removed from the data. Figure 5.1 shows an example of the correlated data, which were taken during Research Flight 9 on April 14, 2001. The x-axis is the light scattering channel, which increases in the direction of increasing intensity of light scattered by particle. The y-axis is the time of flight channel, which increases with increasing particle time of flight between the two detection laser beams, i.e., aerodynamic particle size. The data mask is represented by a straight line in the two-dimensional time of flight-scattering intensity space. Particles appearing below the line are identified as artificial and removed. The mask given by the dashed line (TSI carbon mask) is based on the calculation of light scattered by black carbon particles; the solid line is a custom mask constructed based on ACE-Asia data. Analysis of data using each of the two data masks is considered in the case studies.

APS measurements of liquid droplets are also susceptible to errors due to droplet deformation, especially near the upper size limit of the APS. Griffiths et al. (1986) [26] found for 15 μm droplets that the sizes measured by the APS are 7%–20% smaller

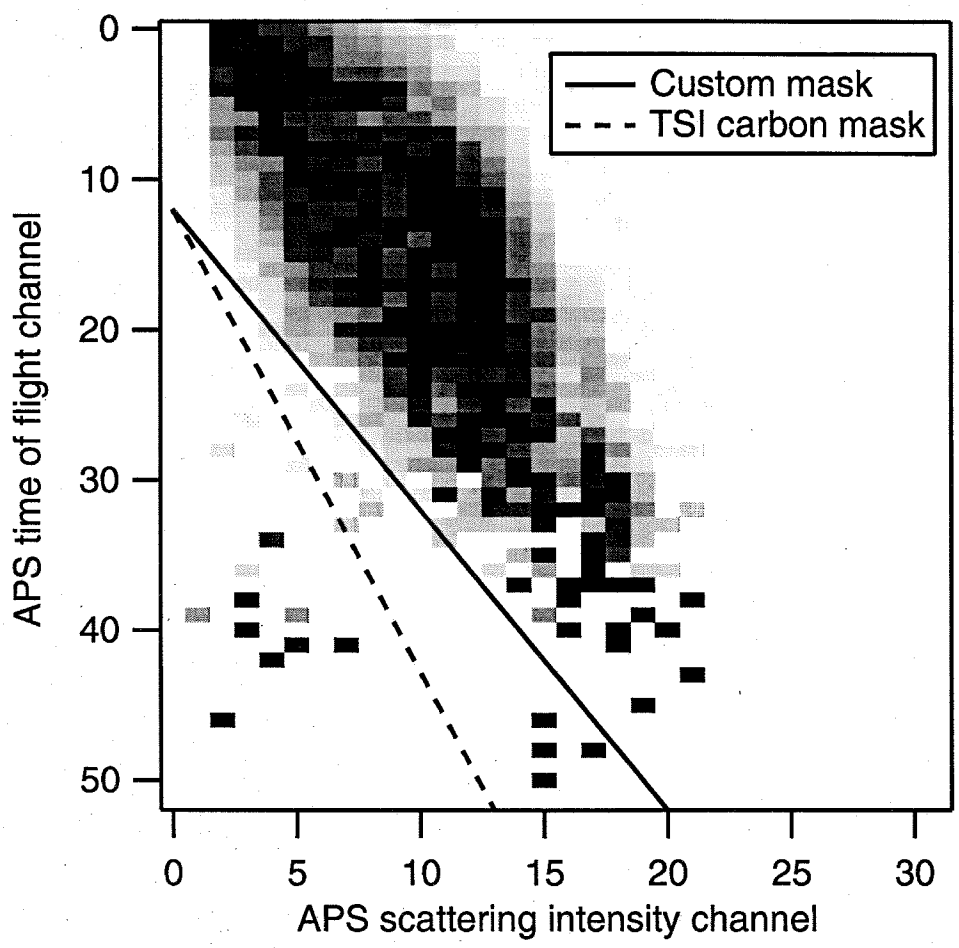

Figure 5.1: APS correlated data, taken during Research Flight 9 on April 14, 2001. Two data masks used to remove artificial particles are indicated by the solid and dashed lines. The x-axis is the light scattering channel, which increases with increasing intensity of light scattered by particles. The y-axis is the time of flight channel, which increases with increasing particle time of flight between two detection laser beams, and is an indication of particle size.

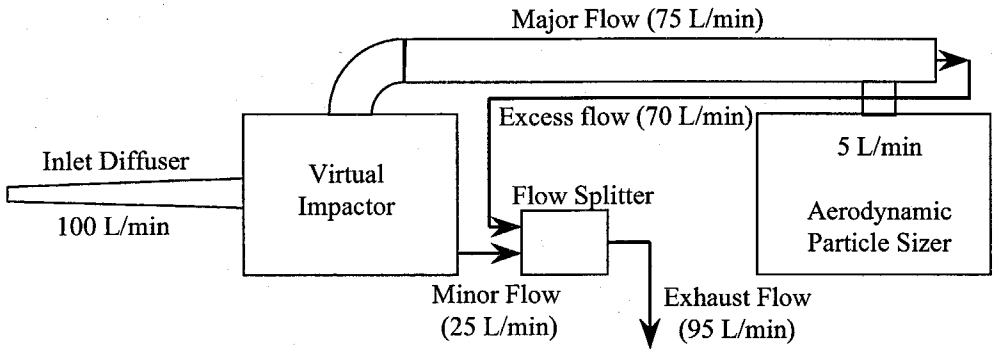

Figure 5.2: Schematic diagram of the inlet system for airborne APS measurement.

than the true size depending on the liquid used to generate the droplet. Droplet deformation is characterized by the Weber number, which is the ratio of aerodynamic drag force to the surface tension of droplet. For water droplets, the Weber number within the APS size range is less than half of the critical value, the point at which the deformation becomes significant. In addition, for APS measurements during ACE-Asia, large droplets, which are often dominated by NaCl (sea salt), have a smaller Weber number than that of pure water droplets as a result of increased surface tension. Thus, droplet deformation can be neglected as a source of error in ACE-Asia APS data.

The commercial APS has been engineered for laboratory measurement. A special inlet for airborne sampling was developed by MSP Corp. to minimize impaction particle losses when transporting particles in a high speed air stream to the instrument (Figure 5.2). The flow rate of the APS inlet system, 100 L/min, is equal to the product of the average aircraft cruising speed, i.e., 50 m/s, and the cross-sectional area of the inlet diffuser tip. The actual instantaneous flow rate may be somewhat different from the average value, 100 L/min, and the resulting uncertainty in predicted aerosol extinction is discussed subsequently. After entering the inlet diffuser, the flow slows down significantly. The ID of the inlet diffuser tip is 0.66 cm and the ID at the

end of the 7 degree diffuser is 2.54 cm. The flow then enters a virtual impactor, where it is split in a 25/75 ratio. The flow division is achieved by a flow splitter with two carefully sized orifices, the performance of which was confirmed experimentally under typical flight conditions. A small fraction (5 L/min) of the major flow after the division (75 L/min) is sampled by the APS, and the remainder of the flow (70 L/min) is removed from the system with the minor flow.

The total counting efficiency of the APS measurement, η_t, is

$$\eta_t = \eta_s \eta_{APS}, \tag{5.3}$$

where η_s is the transmission efficiency of the airborne inlet system and η_{APS} is the counting efficiency of the APS. η_s is determined using uranine-tagged oleic acid particles, which are generated by a TSI vibrating orifice aerosol generator. The efficiency was calculated from the mass of aerosol collected on the 5 L/min APS tube with respect to the total mass entering the sampling system at 100 L/min flow rate, multiplied by the flow split ratio (i.e., 20).

The counting efficiency of the APS is a product of aspiration (η_{asp}), transmission (η_{tran}), and detection (η_{det})efficiencies:

$$\eta_{APS} = \eta_{asp} \eta_{tran} \eta_{det} \tag{5.4}$$

The aspiration and transmission efficiencies characterize the super-isokinetic sampling of the APS inner inlet and the particle deposition on the inner nozzle, respectively. The detection efficiency is defined as the fraction of particles entering the detection area that are counted.

While APS counting efficiency APS has received a lot of attention, the only study of the counting efficiency of the most recent model 3320, that deployed on the Twin Otter, is apparently that of Armendariz and Leith (2002) [2]. The counting efficiency from Armendariz and Leith (2002) [2] and that of an earlier model (3310) from Kin-

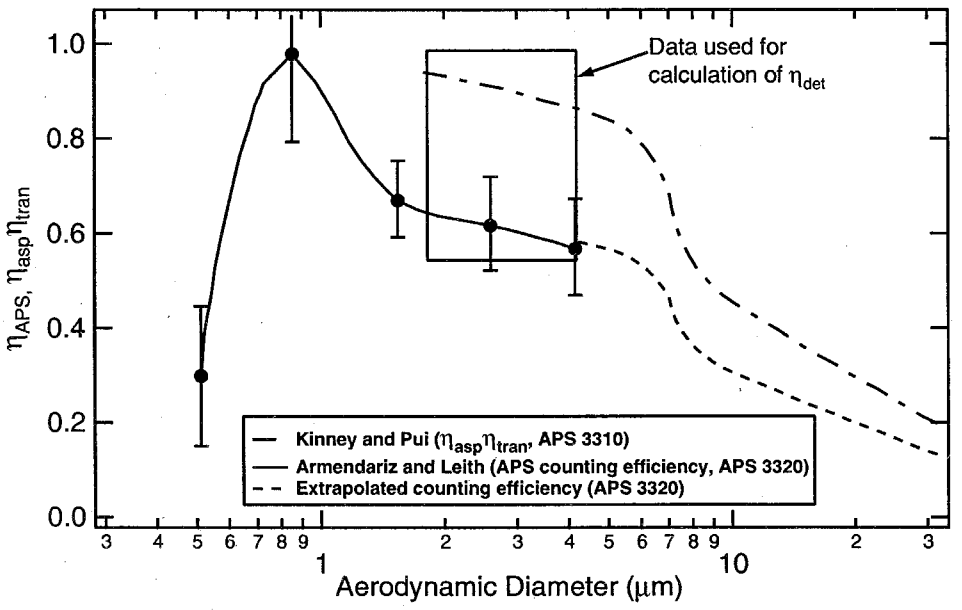

Figure 5.3: APS counting efficiency from Armendariz and Leith (2001) [2] and $\eta_{\text{asp}}\eta_{\text{tran}}$ for APS model 3310 from Kinney and Pui (1995) [40].

ney and Pui (1995) [40] are shown in Figure 5.3. Due to the problem of artificial particles appearing in the large size range, Armendariz and Leith (2002) [2] reported the counting efficiency of particles only smaller than 5 μm. The data show that the counting efficiency of the APS 3320 begins at 30% for 0.5 μm diameter particles, increases to 100% for 0.9 μm particles, then drops to 60% for 5 μm particles. The non-unity counting efficiency around 0.5 μm is probably due to the low detection efficiency, a result of low scattering light intensity of submicron particles. In this study, APS measurements below 0.7 μm were not used, since the detection efficiency varies for particles with different refractive indices.

Kinney and Pui (1995) [40] studied the product of the aspiration and transmission efficiencies ($\eta_{\text{asp}}\eta_{\text{tran}}$) of the earlier 3310 model. Since the APS 3320 has a similar design of the inlet geometry and similar flow characteristics to those of the 3310 model, the detection efficiency of the APS 3320 within the overlap region of the two measurements can be approximated by the ratio of reported efficiencies (Figure 5.3). Assuming the detection efficiency is constant for particles larger than 2 μm, the counting efficiency of the APS 3320 can be extrapolated from Kinney and Pui's results to diameters exceeding 5 μm. The assumption of a constant detection efficiency is supported by the detection efficiency derived in the overlap region, which shows little variation. To account for the potential error in the extrapolation of the APS counting efficiency, a $\pm$50% uncertainty is assumed for the APS concentration over the extrapolation size range in the uncertainty analysis of the aerosol extinction calculation.

5.2.3 Integration of Size Measurements

Adjusting the DMA and APS measurements to ambient size distributions, which are needed for extinction calculations, requires knowledge of measurement conditions inside each instrument as well as the response of aerosol size to the RH change. For the DMA system with active RH control, the RH inside the instrument was generally

maintained at the ambient level and little correction was needed. However, when the aircraft sampled air masses with rapid RH variation, the RH inside the instrument lagged somewhat behind the ambient RH. The RH inside the DMA was continuously monitored and recorded. Determining deviation of the APS measurement RH from the ambient RH inside the APS is more complicated than for the DMAs since neither RH nor temperature of the sample flow is directly measured. Assuming no heat exchange between the aerosol flow and the conduit wall, the temperature of the air stream increases about 1.2°C as the flow decelerates in the diffuser. The residence time of the air flow before reaching the APS is about 0.4 s, which is sufficient for particles up to 20 μm diameter to adjust to the decreased RH. Before reaching the sensing volume, the RH of the aerosol flow once again changes as a result of acceleration through the APS nozzle. However, the resulting lower temperature and higher RH will not further change the particle size, since the time between acceleration and detection is about 1 μs. Since the water vapor concentration is conserved during transport of the air stream to the APS, the RH of the APS measurement was calculated from the ambient RH assuming a 1.2°C increase in temperature. The sensitivity of calculated aerosol extinction to the amount of APS ram-heating is discussed later.

5.2.4 Aerosol Chemical Composition and Mixing State

Back-calculation of the *ambient* particle size distribution from each instrument's data requires knowledge of the size response to RH. Interpretation of APS data requires the particle density, which, in turn, generally necessitates knowledge of aerosol chemical composition and mixing state. The construction of aerosol chemical composition is discussed in this section, and the two sections following focus on the calculation of the aerosol size response to RH and aerosol density. On board the Twin Otter, a set of 8 Micro-Orifice Uniform Deposit Impactors (MOUDI) and three denuder samplers were deployed to characterize aerosol chemical compositions. The sample flow rate of the MOUDI is 100 L/min. Each MOUDI has 5 stages that collect particles within pre-

determined aerodynamic diameter ranges. However, only one stage of each MOUDI was used to collect particles (below 3 μm) during the ACE-Asia campaign. The 8 MOUDIs enable sampling of multiple representative air mass during each flight. The MOUDI sample filters were extracted using deionized water (HPLC grade) through mechanical shaking for 20 minutes. The filter extracts were then analyzed for the metallic elements using an inductively coupled plasma — atomic emission spectrometer (ICP-AES, model Jarrell Ash 955), and water-soluble anionic species using a standard ion chromatography (IC) system (model DIONEX DX-500) [24].

A pair of low-flow denuder samplers were used to collect filter samples for analysis of Organic Carbon (OC), and Elemental Carbon (EC) using a thermal-optical carbon analyzer. A single high-volume particle trap impactor-denuder sampler was used to collect samples for the determination of water-soluble organic carbon and individual compounds comprising the OC. Calibration experiments determined the collection efficiency of the denuder sampler is over 90% for particle with 2.3 μm diameter or smaller [45].

None of the above samplers produced size-dependent information on chemical composition; thus, the following assumptions are made in order to construct the size-resolved chemical composition. Since the concentration of NH_4^+ was not determined, the NH_4^+ concentration is estimated using the molar ratio, $NH_4^+/(2SO_4^{2-} + NO_3^-)$. Table 5.2 lists recent studies of aerosol chemical composition in East Asia. Ammonium to sulfate plus nitrate molar ratios among the studies range from 0.59 to 0.89. A ratio of 0.75 is assumed in this study. Based on previous observations that sulfate, nitrate, OC, and EC are found primarily in small particles, and dust and sea salt are most likely to reside in larger particles, the aerosol mass was divided into fine and coarse modes. The size boundary between the two modes will be discussed below. The fine mode consists of NH_4^+, SO_4^-, NO_3^- OC, and EC, and the coarse mode includes sea salt and dust. When the mass size distributions of the fine and coarse modes are log-normal distributions with the same geometric standard deviation, for aerosol

Table 5.2: The concentration of NH_4^+, SO_4^{2-}, and NO_3^- during recent studies of aerosol chemical composition in East Asia. Unit: $\mu g/m^3$

Reference	NH_4^+	SO_4^{2-}	NO_3^-	Molar ratio $NH_4^+/(2SO_4^{2-}+NO_3^-)$	Location
He et al. (2001) [27]	4.28	10.15	7.26	0.72	Beijing, China
Choi et al. (2001) [12]	4.5	7.28	8.04	0.89	Seoul, South Korea
Choi et al. (2001) [12]	5.51	12.79	13.14	0.64	Seoul, South Korea
Choi et al. (2001) [12]	3.87	11.16	8.16	0.59	Seoul, South Korea
Kim et al. (1998) [39]	2.81	8.4	0.89	0.82	Cheju, South Korea

with diameter D_p, the mass ratio of the two modes could be written as

$$\frac{f_{coarse}(D_p)}{f_{fine}(D_p)} = (\frac{D_p}{D_{p0}})^{\alpha}$$
$$f_{coarse}(D_p) + f_{fine}(D_p) = 1, \tag{5.5}$$

where $f_{coarse}(D_p)$ and $f_{fine}(D_p)$ are the mass fractions of coarse mode and fine mode in the total mass of aerosol with diameter D_p, respectively. α is a positive number that ensures that the fine mode and coarse mode dominate the total mass at small and large particle sizes, respectively. It will be shown subsequently that the calculated aerosol extinction is insensitive to the value of α, and a value of 3.3 is assumed in this study. D_{p0} is the particle diameter at which the mass fractions of the fine mode and the coarse mode are equal to each other, 50%, which is the "size boundary" between the two modes. D_{p0} is selected such that when Eqn. (5.5) is combined with the in situ aerosol size distributions, the calculated fine mode mass of aerosol matches the MOUDI and denuder sampler measurements. The mass ratios among the chemical species of the fine mode are assumed as constants, which are determined from MOUDI and denuder sampler measurements. The assumption of constant mass ratio among fine mode chemical species is supported by on-board Aerosol Mass Spectrometer size

and chemically resolved mass concentration measurements, which showed the mass ratios between $SO_4/NH_4/NO_3$/Organics were approximately independent of size in the submicron size range [3]. For the partition of sea salt and dust within the coarse mode, the majority of the coarse mode is assumed to be sea salt in the boundary and pollution layers, and dust in the free troposphere (with the exception of the April 23 case discussed later). These assumptions are necessary, since none of the samples is size-resolved, and the filters do not include all the mass above 3 μm diameter. For each flight, size-resolved chemical compositions were generated for each layer.

A Tandem DMA system was on-board the Twin Otter for measurement of aerosol hygroscopic properties [18]. The system employs two high flow DMAs to maximize the counting statistics. Hygroscopic properties of particle with diameters ranging from 40 nm to 586 nm were measured. During most of the ACE-Asia flights, the Tandem DMA data showed that aerosols of the same dry size grew to similar final size, i.e., similar water uptake when exposed to high humidity, suggesting that the particles were internally mixed. Based on these observations, the present analysis assumes internally mixed aerosols. While the mixing state of supermicron particles is not available from hygroscopicity measurements, the assumption of an internally mixed aerosol in this size range should not cause significant errors, since frequently the supermicron aerosols were dominated by a single component, sea salt or mineral dust.

5.2.5 Calculation of Aerosol Size Response to RH

Given aerosol chemical composition, the size response to varying RH was determined using the thermodynamic equilibrium model, ISORROPIA [50]. ISORROPIA describes the sodium-ammonium-chloride-sulfate-nitrate-water aerosol system, and predicts the equilibrium water content, as well as the concentration, of chemical species in both aqueous and solid phases of aerosol at given RH and temperature.

For RH between the crystallization and deliquescence points, particles can exist in either the metastable state (deliquesced) or equilibrium state (crystallized). Usually, the state of the aerosol can be determined by comparing the two size distributions measured by the DMA systems. As described above, the RH within one DMA (termed the "ambient" DMA) was maintained at ambient level by using an active RH controller. However, the size distribution measured by the "ambient" DMA is not always the true size distribution of the ambient particles. Since the RH of the aerosol flow first decreases as the flow enters the inlet, the deliquesced aerosol may be crystallized due to the initial RH decrease, and remain crystalized even after the RH later recovers to the ambient level. Therefore, we can be confident that the ambient aerosol is deliquesced only when the *aerosol measured by the "ambient" DMA* is deliquesced, which is evidenced by a shift of the size distribution measured by the "ambient" DMA towards larger sizes as compared to the dry distribution. When particles measured by the "ambient" DMA are crystallized (identical size distributions from the two DMA systems), the true state of the ambient aerosol is less clear, especially when the ambient RH is just above the crystallization point. In this case, it is assumed that the aerosols within the boundary layer are deliquesced, and aerosols within elevated pollution layers and in the free troposphere are crystallized. Uncertainties associated with this assumption will be investigated subsequently. Organic carbon, elemental carbon, and mineral dust are considered nonhygroscopic, and are only present in the solid phase of the aerosol. This assumption is more likely to hold for elemental carbon and mineral dust, but not necessarily for many organic species likely to be present [60].

5.2.6 Calculation of Particle Density

At given RH and temperature, the aerosol density is calculated using the concentrations of both aqueous and solid phases of aerosol, which are provided by ISOR-

ROPIA. The density of the aqueous phase is calculated based on partial molar volumes,

$$\rho_a = \frac{1000 + \sum_i c_i M_i}{\frac{1000}{\rho_0} + \sum_i c_i \bar{V}_i^0 + V_{mix}^{ex}}, \tag{5.6}$$

where ρ_a is the density of the aqueous phase, ρ_0 the density of pure water, c_i the molality of each solute, M_i the molecular weight, $\bar{V}_i^0$ the partial molar volume, and V_{mix}^{ex} the excess molal volume. In our calculation, it is assumed that no volume change associated with mixing of water and the solutes occurs, i.e., $V_{mix}^{ex} = 0$. The error in calculated density by assuming $V_{mix}^{ex} = 0$ does not exceed 5% over the concentration range of NaCl droplets. This suggests that the assumption should not introduce significant error in the analysis since the density calculation only affects the interpretation of APS data. For the size range measured by the APS, the aqueous aerosol phase, if any, is generally dominated by NaCl.

The solid phase is assumed potentially to consist of 11 components, 8 of which are inorganic salts, and the other 3 are nonhygroscopic species: OC, EC, and mineral dust. The density of the inorganic salts are available from CRC (1970) [20], and the densities of OC, EC, and mineral dust are assumed to be 1.2 [74], 2.0 [22], and 2.5 g/cm^3 [76], respectively. Once the densities of the aqueous phase and each component within the solid phase are determined, the calculation of aerosol density can be carried out.

Through the calculation described above, data from the DMA and APS were used to determine the corresponding size distributions under ambient conditions. The agreement between ambient distributions derived from DMA and APS measurements usually fell within 20% in the size range within which the two instruments overlap. Figure 5.4 shows an example of ambient size distributions derived from DMA and APS measurements at 450 m during Research Flight 17 from UTC 1:38 to 2:09 on April 27, 2001. For the size distribution in the overlap range of the DMA and APS, a simple average of the DMA and APS distributions was used.

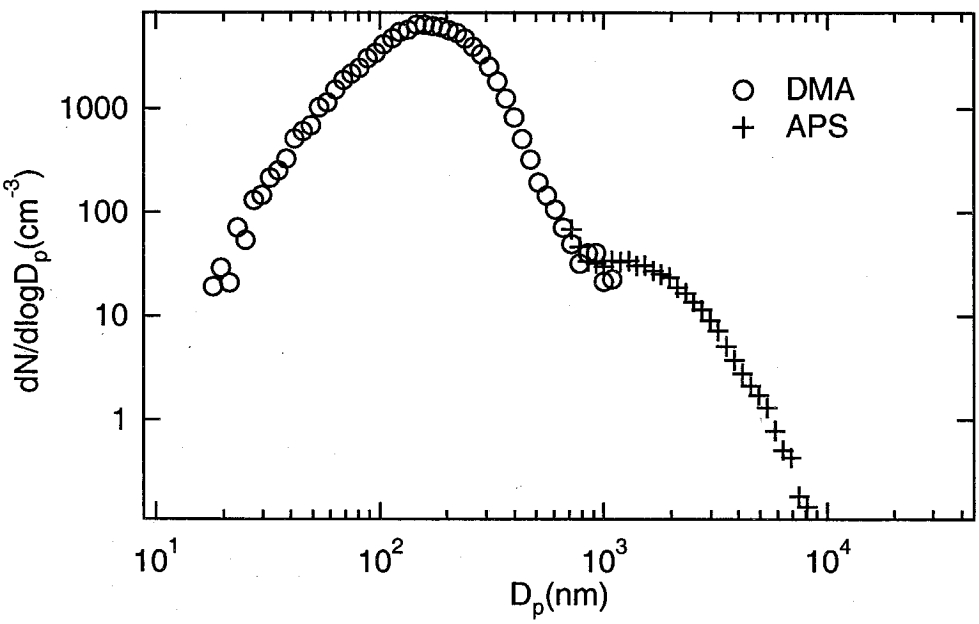

Figure 5.4: Ambient size distributions derived from DMA and APS measurements in a layer at 450 m altitude during Research Flight 17 on April 27, 2001 .

5.2.7 Effective Particle Refractive Index

Given the chemical composition of an internally mixed particle, the optical properties are often calculated through the effective refractive index approach, assuming an equivalent homogeneous sphere with an effective, or average, refractive index, which is derived from the refractive index of each component within the aerosol. In our analysis, the refractive index of the aerosol is averaged over the aqueous phase and each component in the solid phase using the Bruggeman mixing rule [8],

$$\sum_{i=1}^{n} f_{vi} \frac{m_i^2 - m_{av}^2}{m_i^2 + 2m_{av}^2} = 0, \tag{5.7}$$

where i indicate the aqueous phase or the different components of the solid phase within the aerosol, f_{vi} is the volume fraction, m_i the refractive index of component i, and m_{av} is the average aerosol refractive index that is being sought . With the aqueous phase composition given by ISORROPIA, the refractive index of the liquid phase can be obtained through the partial molal refraction approach [49]. The refractive indices of the 8 inorganic salts of the solid phase are taken from CRC (1970) [20], and OC and EC are assumed to have refractive indices of $1.55 + 0i$ [44] and $1.99 + 0.66i$ [64], respectively. With no available data on the refractive index of East Asia mineral dust, the refractive index of central Asia dust, $1.5 + 0.003i$ [67], was used. The refractive index of each component is assumed constant within the AATS-14 wavelength range (363 nm–1558 nm). Both experimental [13] and modelling studies [75] demonstrate that the Bruggeman mixing rule predicts aerosol extinction well for composite particles. The aerosol extinction was also calculated using volume-averaged refractive indices to estimate the uncertainties introduced by the average method.

5.2.8 Optical Measurements and Calculation

The 14-wavelength NASA Ames Airborne Tracking Sunphotometer (AATS-14) was deployed on the Twin Otter. The AATS-14 continuously measured the optical depth of the column of air between the aircraft and the top of atmosphere. By subtracting from this value the optical depth due to Rayleigh scattering of gas molecules and absorption by O_3, NO_2, H_2O, and O_2-O_2 (see Schmid et al., 2002, [62]), the aerosol optical depth (AOD) throughout the column of air between the altitude of the aircraft and the top of the atmosphere is calculated. The derivative of AOD with respect to altitude gives the aerosol extinction σ_{ext} at different altitudes,

$$\sigma_{ext}(z,\lambda) = \frac{d\tau(z,\lambda)}{dz}, \tag{5.8}$$

where $\tau(z,\lambda)$ is the aerosol optical depth (AOD) at wavelength λ, and z is the distance between the instrument and top of atmosphere. Prior to differentiation, $\tau(z,\lambda)$ is smoothed (in a non-biased manner) to reduce effects of horizontal and temporal variations of AOD on the photometer-to-sun path at a given altitude (see, e.g., Schmid et al., 2000 [61]). Uncertainties in derived aerosol extinction introduced by the smoothing procedure are estimated as 0.005 km^{-1} [61].

To compare with extinction derived from the AATS-14 data, aerosol extinction is calculated using ambient aerosol size distributions together with effective refractive indices based on aerosol chemical compositions. For each particle diameter, the extinction crosssection is calculated using Mie theory at the 13 wavelengths measured by the sunphotometer (one of the 14 wavelengths was used for the measurement of water vapor concentration). The aerosol extinction is an integration over the measured size range,

$$\sigma_{\rm ext}(z,\lambda) = \int_{D_{\rm p1}}^{D_{\rm p2}} \frac{\pi}{4} D_{\rm p}^2 Q_{\rm ext}(D_{\rm p},\lambda,m(D_{\rm p},{\rm RH},z)) n(D_{\rm p},z) dlog D_{\rm p}, \tag{5.9}$$

where $D_{\rm p}$ is the particle diameter over which the integral is performed. $D_{\rm p1}$ and $D_{\rm p2}$

are the minimum and maximum diameters of measurement, respectively. Q_{ext} is the extinction cross section based on Mie theory, $m(D_{\text{p}}, \text{RH}, z)$ the effective refractive index of the particle, which is a function of the particle's size, composition, and (implicitly) ambient relative humidity. $n(D_{\text{p}}, z)$ is the particle size distribution at ambient conditions.

5.2.9 Uncertainty Analysis

The degree to which clear column radiative closure is achieved is judged by the closeness with which measured and calculated extinctions agree. To understand discrepancies between the calculated and measured σ_{ext}, the uncertainties associated with the calculated aerosol extinction need to be addressed. The uncertainty sources, which are grouped into 7 categories, are listed in Table 5.3, together with the uncertainty levels assumed in the analysis. Many of the entries in Table 5.3 have been discussed above. To examine the uncertainty associated with aerosol mixing state, we carried out a complete calculation based on an externally mixed aerosol, in which 8 types of aerosol were assumed: $(NH_4)_2SO_4$, NH_4HSO_4, H_2SO_4, NH_4NO_3, OC, EC, sea salt, and dust. For this externally mixed aerosol, the water content of hygroscopic aerosol and its density were calculated using data of Tang and Munkelwitz (1994) [71], Tang (1996) [70], and Tang et al. (1997) [72]. The aerosol extinction is the summation of the contribution from each type of aerosol. The organic molecular weight per carbon weight, $m_{\text{oc}}/m_{\text{c}}$, value of 2.1 ± 0.2 was used in our study [74]. $m_{\text{ions}}/m_{\text{carbon}}$ is the mass ratio of fine mode ions (NH_4^+, SO_4^{2-}, and NO_3^-) from the MOUDI sample to total carbon from the denuder filter samples. The $\pm 30\%$ uncertainty assumed for this ratio accounts for the different cut sizes and uncertainties in the analysis of the MOUDI and denuder filter samples. The results of the uncertainty analysis are presented with each of the four cases studied.

Table 5.3: Assumed levels of uncertainty associated with properties required for calculation of aerosol extinction from aerosol size distribution and composition measurements.

Uncertainty source	Base value	Uncertainty
Deliquescence and efflorescence		
Deliquesced?	N/A	N/A
Mixing state		
Mixing state	Internal	External
RH measurements and ram heating		
Ambient RH	N/A	±1%
RH inside DMA	N/A	±3%
APS ram heating	1.2°C	1°C,2°C
Accuracy of size and conc. measurement		
DMA size	N/A	±5%
DMA concentration	N/A	±10%
APS size	N/A	±10%
APS concentration	N/A	±20% ($< 5\mu$m),±50% ($\geq 5\mu$m)
APS data mask	Custom	TSI carbon
Chemical composition		
$NH_4^+/(2{\cdot}SO_4^{2-}+NO_3^-)$	0.75	±0.25
m_{oc}/m_c	2.1	±0.2
m_{ions}/m_{carbon}	N/A	±30%
m_{dust}/m_{coarse}	N/A	±0.2
D_{p0} in Eqn. 5.5	N/A	×1.5,/1.5
α in Eqn. 5.5	3.3	2.7,4.3
Particle density		
Dust density	2.5	±30%
OC density	1.2	±20%
EC density	2.0	1.9,2.1
Effective refractive index		
Eff. refractive index	Bruggeman	Volume average

5.3 Radiative Closure

During ACE-Asia, 19 Twin Otter research flights were conducted out of Iwakuni Japan [33]. Among those 19 missions, four flights sampling different air masses presented conditions ideal for detailed analysis of clear-column radiative closure.

5.3.1 Research Flight 14, April 23, 2001

During Research Flight 14, the Twin Otter flew to 33°N and 134°E, southeast of Shikoku Island; the flight track is shown in the top two panels of Figure 5.5. Three layers were sampled in detail. Two layers were within the marine boundary layer (MBL), and centered at 30 m and 600 m. The third layer was within the free troposphere and centered at an altitude of 1900 m.

The total particle number concentration showed little variation within each layer, except for occasional spikes, which may represent small regions in which recent nucleation events occurred. The total particle number concentrations were about 2200 and 500 cm^{-3} for the two MBL layers and the free troposphere layer, respectively. As discussed above, the MOUDI and denuder sampler data were used to construct the size-resolved chemical compositions of the layers, which are shown in Figure 5.5. Unlike other flights, the MOUDI sample taken in the free troposphere contained little Ca and Si, suggesting no significant mineral dust present. All three layers contained significant OC in the submicron size range, while only the layer at 600 m altitude contained significant EC.

The size distributions, together with the aerosol extinction distributions at 525 nm, were averaged for each layer (Figure 5.5). The aerosol extinction distributions are calculated at 525 nm since that wavelength is close to the peak solar irradiance wave-

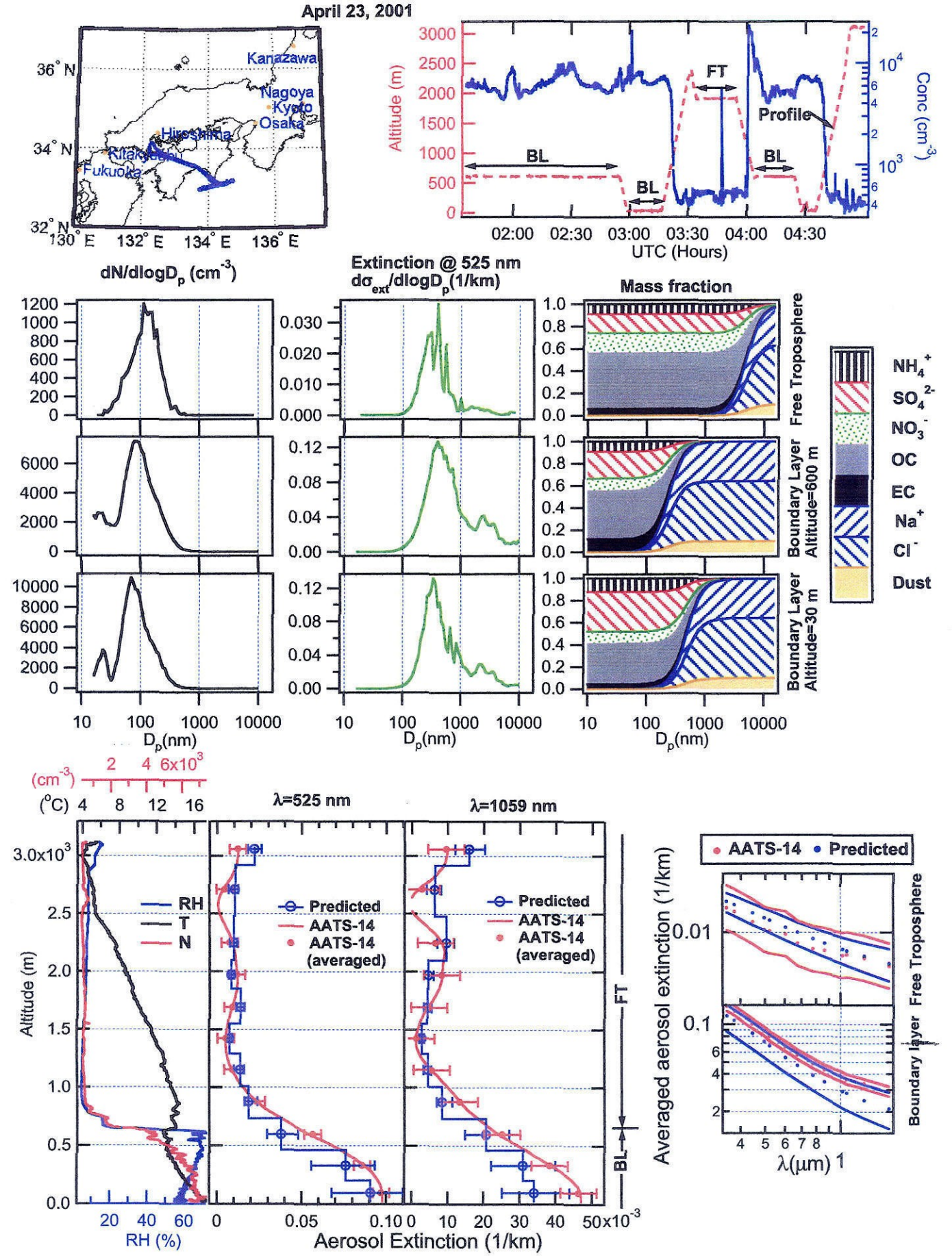
April 23, 2001
Kanazawa
Nagoya
Kyoto
Osaka
Hiroshima
Kitakyushu
Fukuoka
36° N
34° N
32° N
130° E
132° E
134° E
136° E
Altitude (m)
FT
Profile
BL
BL
BL
Conc (cm-3)
02:00
02:30
03:00
03:30
04:00
04:30
UTC (Hours)
dN/dlogDp (cm-3)
Extinction @ 525 nm
dσext/dlogDp(1/km)
Mass fraction
Free Troposphere
Boundary Layer Altitude=600 m
Boundary Layer Altitude=30 m
NH4+
SO42-
NO3-
OC
EC
Na+
Cl-
Dust
Dp(nm)
Dp(nm)
Dp(nm)
(cm-3)
(°C)
λ=525 nm
λ=1059 nm
RH
T
N
Predicted
AATS-14
AATS-14 (averaged)
Predicted
AATS-14
AATS-14 (averaged)
Altitude (m)
RH (%)
Aerosol Extinction (1/km)
FT
BL
AATS-14
Predicted
Averaged aerosol extinction (1/km)
Free Troposphere
Boundary layer
λ(μm)

Figure 5.5: Size distributions, chemical compositions, and aerosol extinction comparison for Research Flight 14 on April 23, 2001. The panels are flight track, total particle number concentration, and flight altitude. Ambient size distributions, aerosol extinction size distributions averaged over the indicated layers (BL=Boundary layer, PL=Pollution layer, and FT=Free troposphere), size resolved chemical compositions. RH, temperature, and total number concentration profiles during the spiral. Comparison of observed and predicted vertical profiles of aerosol extinction at 525 and 1059 nm. The comparison of aerosol extinction is averaged over each layer as a function of wavelength. Uncertainty limits of derived and observed aerosol extinction are blue and red, respectively.

length and is one of those measured by AATS-14. All distributions shown correspond to aerosol at ambient conditions. Within the boundary layer, size distributions at both altitudes are bimodal, with the major mode occurring at 70–80 nm, and the smaller mode at 20 nm, which may reflect result of recent nucleation events. The size distribution in the free troposphere layer was monomodal, with peak concentration at 140 nm. The aerosol extinction distributions indicate that submicron particles dominated total aerosol extinctions of all three layers at 525 nm.

The bottom panels in Figure 5.5 compare calculated aerosol extinctions using size distributions with those derived from the sunphotometer measurements, as well as showing vertical profiles of temperature, RH, and total particle concentration during the spiral. To facilitate comparison, the sunphotometer-derived aerosol extinction has been averaged to correspond to the DMA measurement interval. Comparison of vertical profiles of aerosol extinction at wavelengths 525 nm and 1059 nm are presented. As noted earlier, the uncertainty in aerosol extinction derived from AATS-14 measurement is ± 0.005 km^{-1}, which is introduced by the AOD smoothing procedure [61]. The uncertainty, σ, in the predicted aerosol extinction based on the aerosol size distribution can be estimated by

$$\sigma = \sqrt{\sum_i \sigma_i^2}, \tag{5.10}$$

where σ_i is the uncertainty in predicted aerosol extinction associated with each individual uncertainty (Table 5.3). Except for the point near 600 m altitude (near the boundary of the free troposphere and marine boundary layer), the discrepancies between the aerosol extinctions lie within the estimated uncertainties. The disagreement near 600 m is likely a result of low vertical resolution of the DMA measurement. Aerosol extinctions are also averaged over the boundary layer and the free troposphere, and the results are presented in Figure 5.5 as a function of wavelength. In both layers, the aerosol extinction calculated from the size distributions successfully

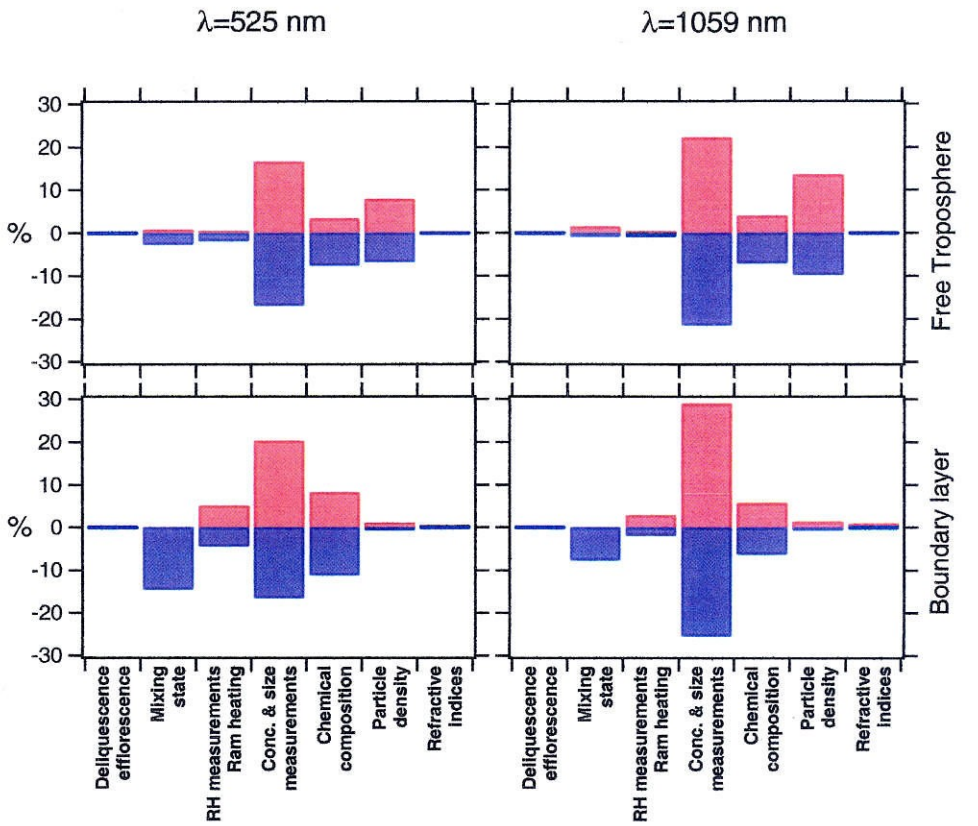

Figure 5.6: Estimated uncertainties in the aerosol extinction calculation based on measured size distribution and chemical composition for Research Flight 14 on April 23, 2001.

reproduces the wavelength dependence from the AATS-14.

Figure 5.6 shows the estimated uncertainties in the aerosol extinction calculation associated with each uncertainty category at 525 nm and 1059 nm. At both wavelengths and in both layers, the estimated uncertainty associated with the accuracy of aerosol size and concentration measurements dominates the overall uncertainty. Uncertainties introduced by assumptions concerning aerosol chemical composition are estimated to be generally within 10%. Estimated uncertainties for radiative closure calculated at 1059 nm are significantly larger than those at 525 nm. This is due to

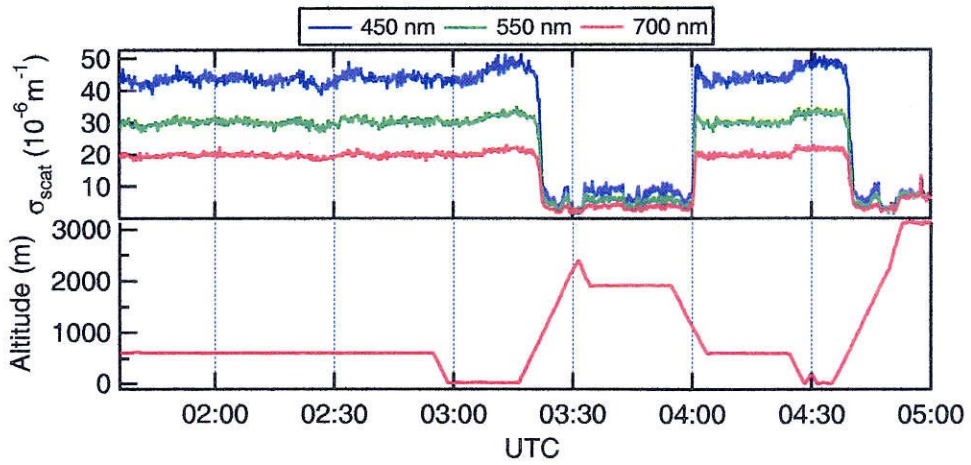

Figure 5.7: Scattering coefficients measured by on-board TSI 3-color nephelometer (model 3563) during Research Flight 14 on April 23, 2001. The wavelengths are 450 nm, 550 nm, and 700 nm.

the uncertainties associated with APS measurement of supermicron particles, which contribute proportionately more to the total extinction at longer wavelength. The uncertainty due to the aerosol state, deliquesced vs. crystallized, is negligible for this profile, since in both layers the aerosol state can be accurately identified by comparing dry and "ambient" size distributions measured by the DMA system, that is, deliquesced at boundary layer and crystallized in free troposphere. The uncertainty arising from the method used to compute the particle refractive indices is negligible, and this will hold also in the other three cases.

The derivation of aerosol extinction from AATS-14 data is based on the assumption that the path between the sun and the sunphotometer passes through horizontally homogeneous layers. The scattering coefficients measured by the on-board TSI 3-color nephelometer (model 3563) within each layer are used as an assessment of the layer homogeneity. Figure 5.7 shows that the variation of scattering coefficients is small within each layer, suggesting that the assumption of horizontally homogeneous

layers is supported for this flight, at least for layers sampled by the Twin Otter's horizontal legs. (As noted by Russell et al.(1999) [59] and Schmid et al.(2000) [61], horizontal and temporal variations of any attenuating layers above the aircraft can affect sunphotometer-derived extinction, but that does not appear to have occurred in this example.)

5.3.2 Research Flight 12, April 19, 2001

Unlike the flight on April 23, a pollution layer with high aerosol extinction was observed between the boundary layer and free troposphere during Research Flight 12 along 133°E to 38°N on April 19, 2001 (Figure 5.8). The Twin Otter flew one-hour legs at 30 m (boundary layer) and 2000 m (pollution layer). The chemical composition of the pollution layer shows an enhanced contribution from nitrate, OC, and EC in the submicron size range, while the boundary layer is dominated by sulfate. The size distributions are monomodal except in the pollution layer. The size distribution of aerosol in the free tropospheric layer is similar to that of Research Flight 14, while in the boundary layer, the peak concentration size, 160 nm, is significantly larger than that of the previous case. Since neither MOUDI nor denuder filter samples were taken for the free tropospheric leg, the chemical composition from the previous flight on April 17 is used. Aerosol extinction during the spiral from UTC 2:37 to UTC 3:02 was calculated for the closure study. Agreement between observed and predicted aerosol extinction is not quite as close as for Research Flight 14. In the boundary layer, the aerosol extinction calculated from the measured size distribution is larger than that derived from sunphotometer measurement at an altitude of 50 m, while smaller than that derived from sunphotometer measurement at 550 m. The discrepancies exceed the estimated uncertainties. While it is not possible to pinpoint the exact reason, the discrepancies in the boundary layer could result from the differentiation of AOD data, the vertical resolution of the DMA measurement, and horizontally

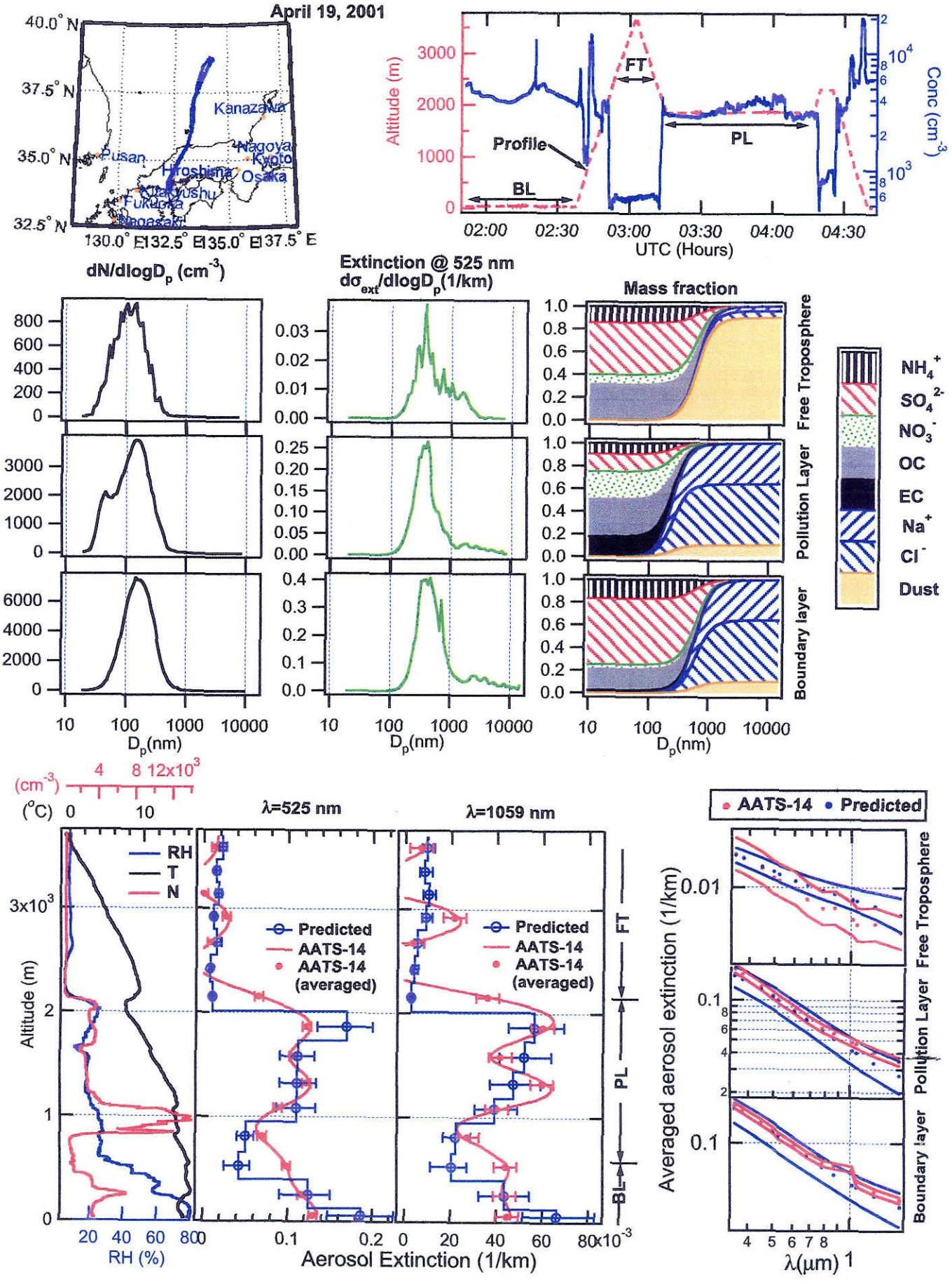
April 19, 2001
40.0° N
37.5° N
35.0° N
32.5° N
130.0° E
132.5° E
135.0° E
137.5° E
Kanazawa
Nagoya
Kyoto
Osaka
Pusan
Hiroshima
Okayushu
Fukuoka
Nagasaki
Altitude (m)
Conc (cm-3)
FT
PL
Profile
BL
02:00
02:30
03:00
03:30
04:00
04:30
UTC (Hours)
dN/dlogDp (cm-3)
Extinction @ 525 nm
dσext/dlogDp(1/km)
Mass fraction
Free Troposphere
Pollution Layer
Boundary layer
NH4+
SO4 2-
NO3-
OC
EC
Na+
Cl-
Dust
Dp(nm)
(cm-3)
(°C)
λ=525 nm
λ=1059 nm
RH
T
N
Predicted
AATS-14
AATS-14 (averaged)
RH (%)
Aerosol Extinction (1/km)
AATS-14
Predicted
Averaged aerosol extinction (1/km)
λ(μm) 1

Figure 5.8: Same format as Figure 5.5. Data and aerosol extinction comparison of Research Flight 12 on April 19, 2001.

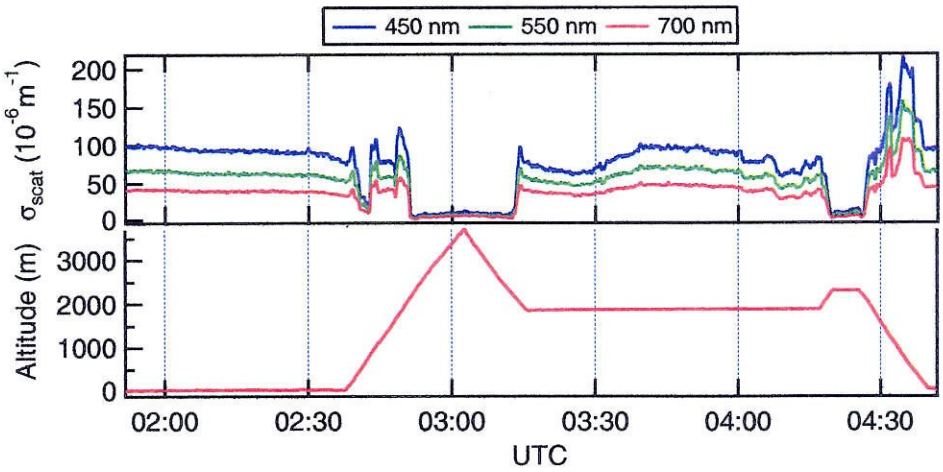

Figure 5.9: Scattering coefficients measured by on-board TSI 3-color nephelometer (model 3563) during Research Flight 12 on April 19, 2001. The wavelengths are 450 nm, 550 nm, and 700 nm.

inhomogeneous layers, as indicated by the variation in aerosol scattering coefficients (Figure 5.9). The oscillations of AATS-14 derived extinctions with respect to the predicted extinction is caused by spatial variability of the overlying AOD. Counting statistics of the size distribution measurements could account for the somewhat different extinction spectra in the free troposphere. To avoid oversmoothing of the AOD, the aerosol extinction is occasionally allowed to become negative, as seen in Figure 5.8. The observed and predicted aerosol extinctions are averaged over each layer, and in good agreement at 13 wavelengths measured by the AATS-14.

Figure 5.10 shows the estimated uncertainties in the aerosol extinction calculation. Similar to Research Flight 14, the uncertainties associated with the accuracies of size and concentration measurements dominate the overall uncertainties in all calculations except in the free troposphere, where uncertainties introduced by the particle density become significant, especially at $\lambda = 1059$ nm. This is mainly a result of uncertainty in the mineral dust density, which is needed to interpret APS measurements for

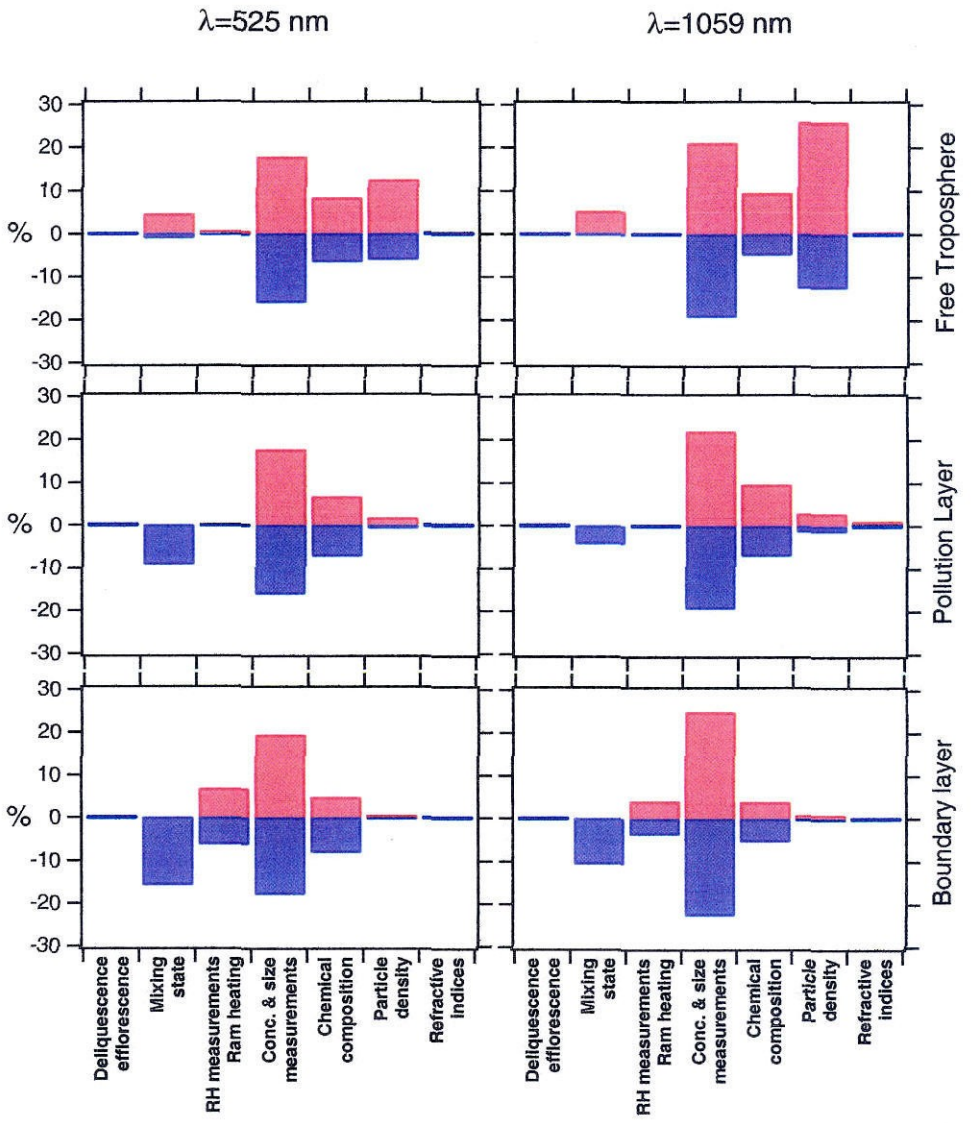

Figure 5.10: Estimated uncertainties in the aerosol extinction calculation based on measured size distribution and chemical composition for Research Flight 12 on April 19, 2001.

size distributions. Uncertainties due to the RH measurement and ram heating are negligible in both the pollution layer and free troposphere, because the ambient RH in each layer was very low, and the uncertainty in RH measurements does not encompass a change in size and calculated aerosol extinction of the crystallized aerosols.

5.3.3 Research Flight 11, April 17, 2001

One focus of Research Flight 11 was to perform intercomparisons with R/V Ron Brown and the SeaWiFS satellite (Figure 5.11). The Twin Otter ferried to 33°N, 128°E, east of Cheju island. The Twin Otter performed one spiral at the time of the SeaWiFS overpass (UTC 5:52). A pollution layer was found between the boundary layer and the free troposphere. A back-trajectory calculation indicated that the pollution layer originated from mainland China. Unlike Research Flights 12 and 14, a dust layer was found in the free troposphere exhibiting significant aerosol extinction. MOUDI and denuder samples were taken at altitudes of 40, 1380, and 2810 m, and the resulting data were used to construct aerosol chemical composition in the boundary layer, pollution layer, and free troposphere. Total particle number concentrations in these three layers were about 5000, 2000, and 500 cm^{-3}, respectively. Aerosol number-vs-size distributions in all layers were monomodal to within the resolution of the linear y-axes shown in Figure 5.11. Compared to the boundary layer, the particle sizes at which the peak aerosol concentration were observed in the pollution layer and free troposphere were larger, suggesting more aged particles aloft. Aerosol extinction shows an increased contribution from supermicron particles to the total extinction at increasing altitude. In the pollution layer the extinction mode at diameter 2000 nm results from a surface area-vs-size mode not resolved in the $dN/dlogD_p$ plot.

Radiative closure is addressed for the aircraft spiral at the time of SeaWiFS overpass at UTC 5:52. As shown in Figure 5.11, the size distribution-derived aerosol extinction is significantly smaller than that derived from the near-surface AATS-14

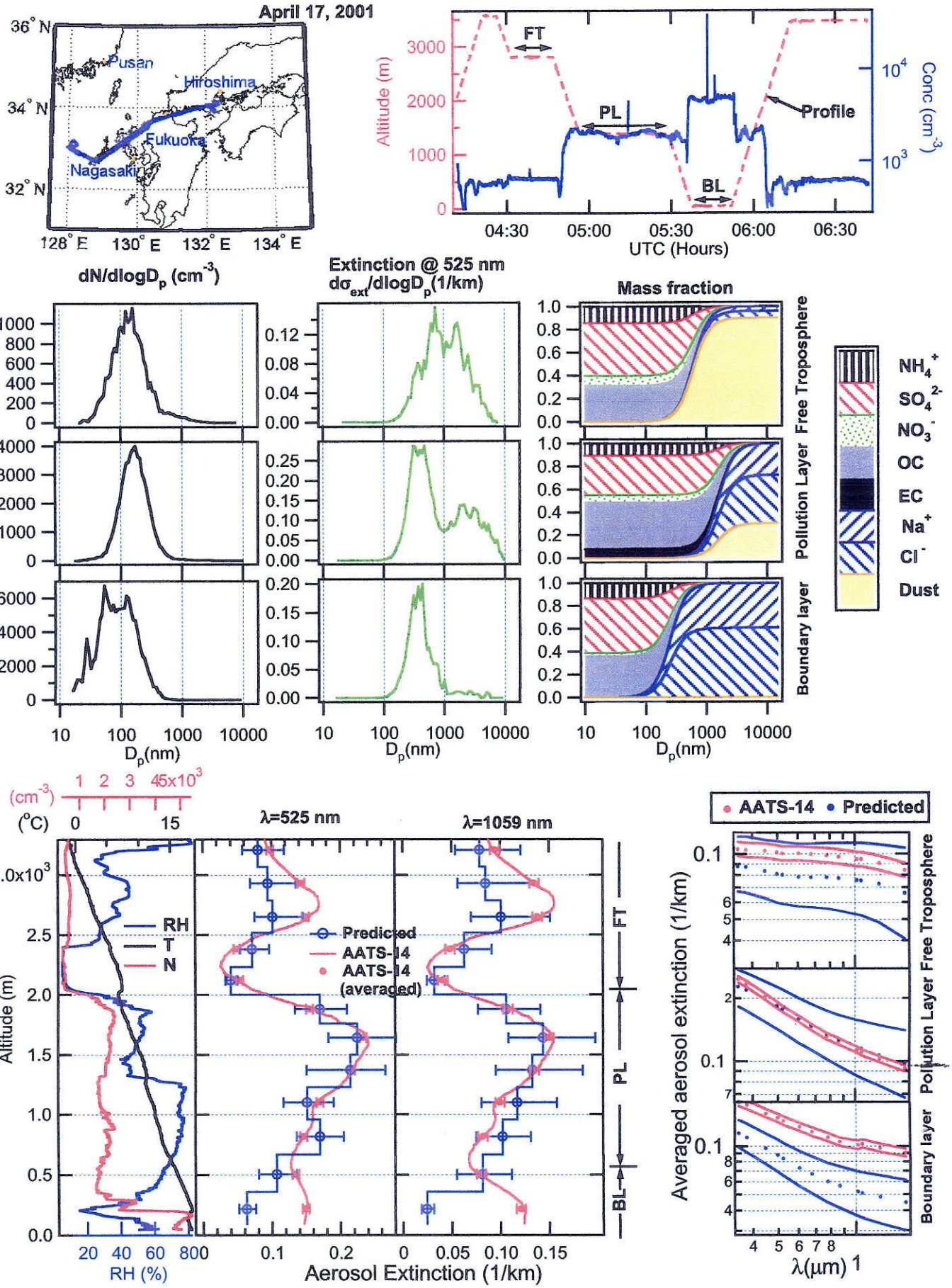
April 17, 2001
36° N
34° N
32° N
128° E
130° E
132° E
134° E
Pusan
Hiroshima
Fukuoka
Nagasaki
FT
PL
BL
Profile
Altitude (m)
Conc (cm-3)
UTC (Hours)
dN/dlogDp (cm-3)
Extinction @ 525 nm
dσext/dlogDp(1/km)
Mass fraction
Free Troposphere
Pollution Layer
Boundary layer
NH4+
SO42-
NO3-
OC
EC
Na+
Cl-
Dust
Dp(nm)
(cm-3)
(°C)
λ=525 nm
λ=1059 nm
RH
T
N
Predicted
AATS-14
AATS-14 (averaged)
RH (%)
Aerosol Extinction (1/km)
AATS-14
Predicted
Averaged aerosol extinction (1/km)
λ(μm)

Figure 5.11: Same format as Figure 5.5. Data and aerosol extinction comparison of Research Flight 11 on April 17, 2001.

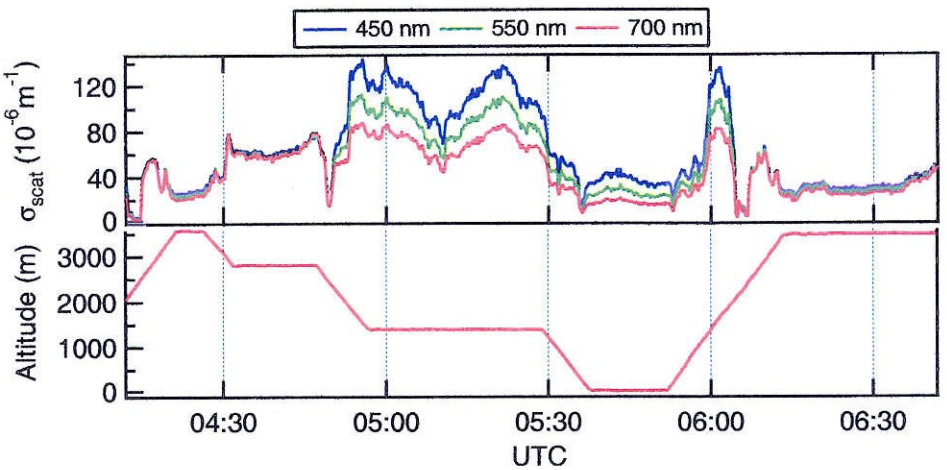

Figure 5.12: Scattering coefficients measured by on-board TSI 3-color nephelometer (model 3563) during Research Flight 11 on April 17, 2001. The wavelengths are 450 nm, 550 nm, and 700 nm.

AOD measurement. Scattering coefficients measured during the flight are shown in Figure 5.12. Among all four cases that we consider here, the in-layer scattering coefficients displayed the most variability for this flight, especially within the pollution layer. The aerosol extinction calculated from the on-board measured size distribution is also supported by aerosol extinction derived from lidar measurement on R/V Ron Brown at the time of spiral (Figure 5.13), which shows a similar aerosol extinction and profile near the surface. Thus, the larger value of extinction obtained from AATS-14 is probably the result of temporal-horizontal variations of AOD on the photometer-to-sun path during the Twin Otter ascent from minimum altitude to 300 m.

For the pollution layer and free troposphere, the discrepancies between observed and calculated aerosol extinctions lie within the calculated uncertainties except for one point in the free troposphere (Figure 5.11). However, the aerosol extinctions calculated from measured size distributions are systematically smaller than those

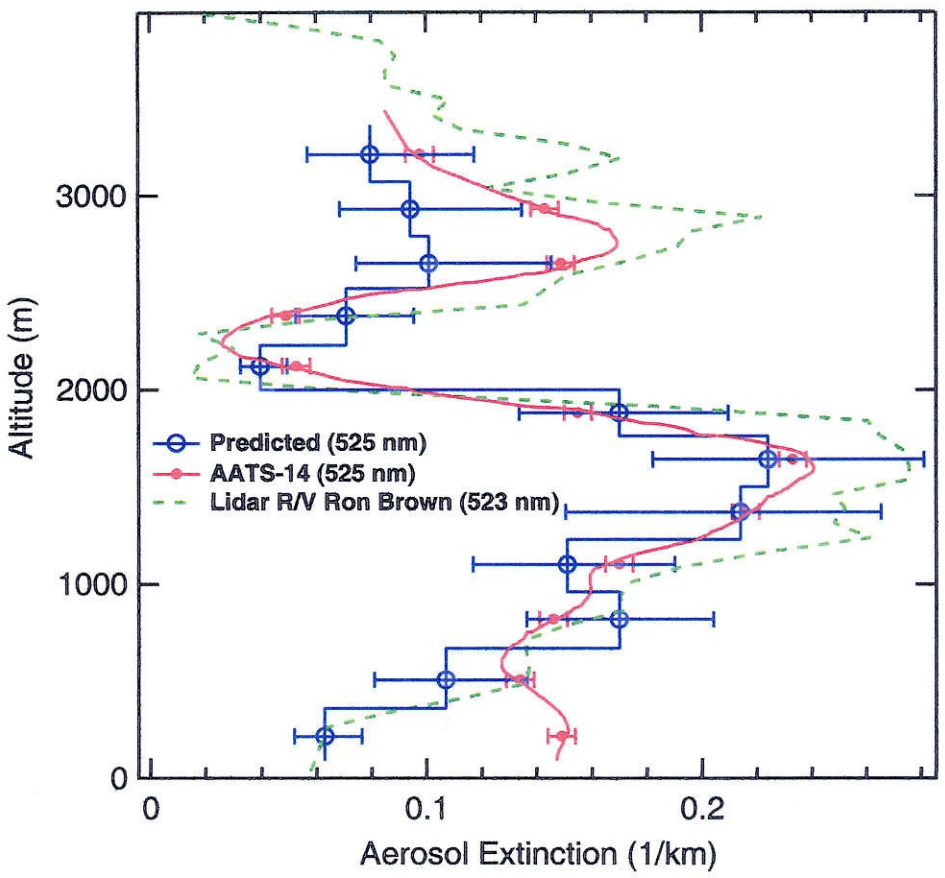

Figure 5.13: Comparison of aerosol extinction derived from AATS-14 measurement, aerosol size distributions, and Lidar measurements on R/V Ron Brown during the spiral of Research flight 11 on April 17, 2001.

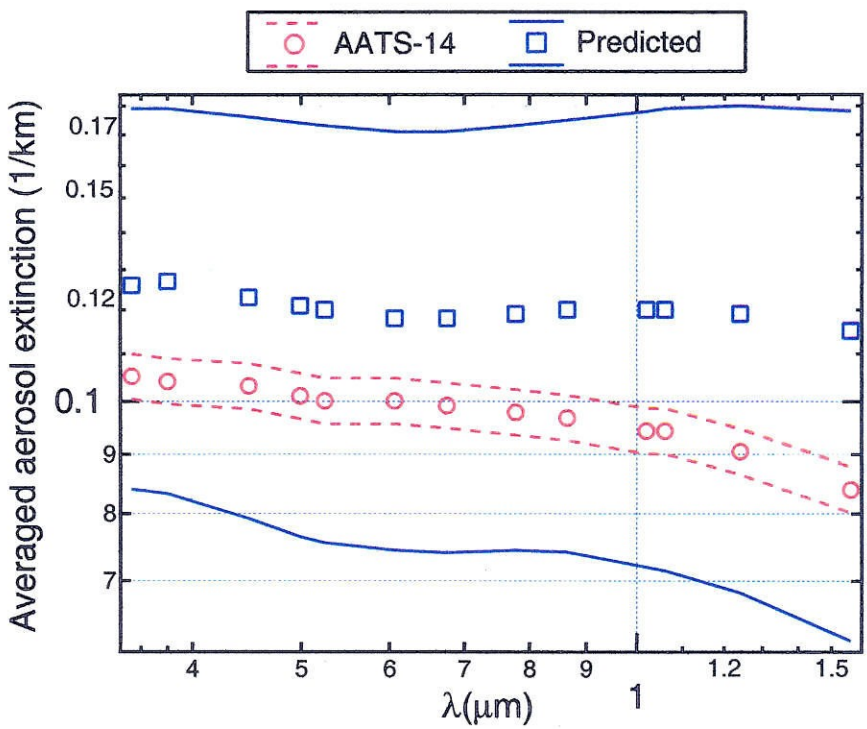

Figure 5.14: Aerosol extinctions averaged over the dust layer of Research Flight 11 on April 17, 2001. The calculation of aerosol extinction is based on a doublet agglomerate particle shape. The dashed and solid lines are the estimated uncertainties in measured and predicted extinctions, respectively.

derived from AATS-14 measurements in the free troposphere. One possible cause is the error in the extrapolation of APS counting efficiency, which could significantly affect the aerosol extinction due to the large mineral dust particles.

That mineral dust particles are spherical is also physically unlikely. Without knowledge of the shape, dynamic shape factor, and ultra-Stokesian correction factor of the mineral dust, the aerosol extinction of nonspherical dust is estimated using the data of doublet agglomerate particles from Cheng et al. (1993) [11]. For doublet agglomerate particles consisting of two spheres, $\kappa = 1.142$, and the ultra-Stokesian correction factor is $1 + 0.1998\mathrm{Re}_\mathrm{p}^{0.6773}$. The aerosol extinction calculation of doublet agglomerates is based on the finding of Mishchenko et al. (1997) [48] that the extinction of large nonspherical particles can be accurately predicted by that of spherical particles with the same surface-equivalent diameter. The calculated aerosol extinction is averaged over the mineral dust layer (Figure 5.14). By assuming a doublet agglomerate shape, the aerosol extinction calculated from the size distribution data is significantly larger than that assuming simply spherical particles. As a result, the calculated aerosol extinction is closer to, although somewhat larger than, that derived from the AATS-14. The increase is 49% at 525 nm and 60% at 1059 nm. The significant increase in aerosol extinction is due to two factors. First, for the same APS response, the volume-equivalent size derived by assuming a doublet agglomerate shape is larger than that derived assuming a spherical shape; second, for the same volume-equivalent size, nonspherical particles have a larger extinction cross-section because of larger surface-equivalent diameters.

The uncertainties in derived aerosol extinction are depicted in Figure 5.15. The uncertainties associated with the accuracy of the aerosol size and concentration measurements dominate the overall uncertainty except in the mineral dust layer, where the uncertainty from particle density, mainly the mineral dust, becomes comparable. Note that Figure 5.15 excludes the uncertainties in dust particle shape discussed in the above paragraph.

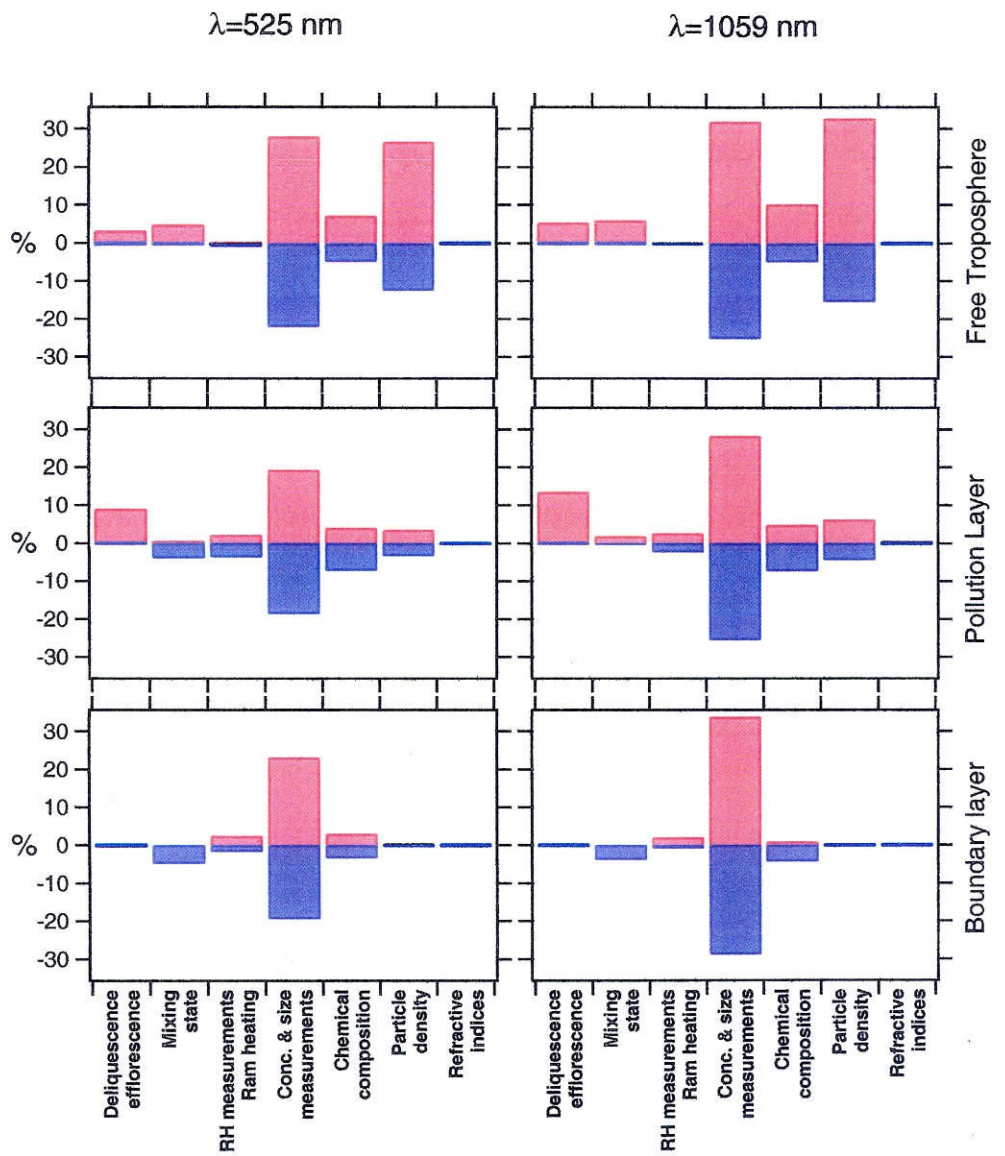

Figure 5.15: Estimated uncertainties in the aerosol extinction calculation based on measured size distribution and chemical composition for Research Flight 11 on April 17, 2001.

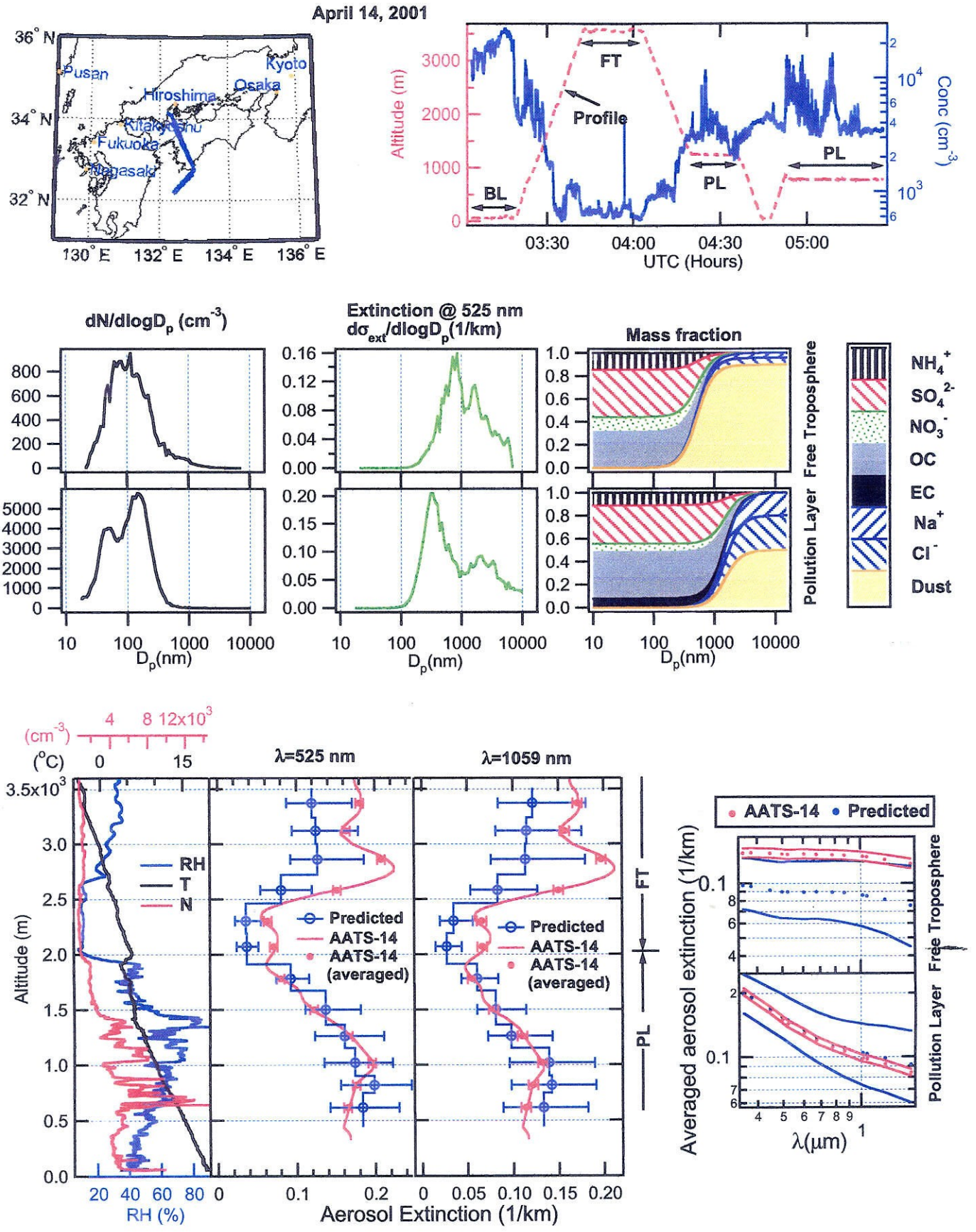
April 14, 2001
36° N
34° N
32° N
130° E
132° E
134° E
136° E
Pusan
Kyoto
Osaka
Hiroshima
Fukuoka
Nagasaki
Altitude (m)
Conc (cm-3)
FT
Profile
BL
PL
PL
03:30
04:00
04:30
05:00
UTC (Hours)
dN/dlogDp (cm-3)
Extinction @ 525 nm
dσext/dlogDp(1/km)
Mass fraction
Free Troposphere
Pollution Layer
NH4+
SO42-
NO3-
OC
EC
Na+
Cl-
Dust
Dp(nm)
(cm-3)
(°C)
λ=525 nm
λ=1059 nm
RH
T
N
Predicted
AATS-14
AATS-14 (averaged)
RH (%)
Aerosol Extinction (1/km)
AATS-14
Predicted
Averaged aerosol extinction (1/km)
λ(μm)-1

Figure 5.16: Same format as Figure 5.5. Data and aerosol extinction comparison of Research Flight 9 on April 14, 2001.

5.3.4 Research Flight 9, April 14, 2001

The fourth of the cases studied focuses on the characterization of a mineral dust layer in free troposphere. The mineral dust layer during Research Flight 9 on April 14 exhibited the largest aerosol extinction among all cases studied. The Twin Otter flight track, to 32.5°N, 132.5°E, south of Shikoku Island, the sampling of different layers, and the spiral for the radiative closure study are shown in Figure 5.16. APS data were not available during the sampling of the boundary layer and the beginning of the spiral; therefore, the analysis focuses on the pollution layer and the mineral dust layer in the free troposphere. Unlike previous cases, the total aerosol number concentration exhibits large variations within each layer. This could be a result of an ongoing mixing process of two different air masses, one of which is a polluted air mass with high particle number concentration. The mixing process is also evidenced by the RH profile during the spiral, which shows substantial vertical variation in the pollution layer. Aerosol extinction distributions are similar to those of Research Flight 11, on April 17, with a bimodal distribution in the pollution layer and a significant contribution of supermicron particles to the total aerosol extinction in the mineral dust layer.

Aerosol extinction closure is achieved again in the pollution layer on this flight. Similar to Research Flight 11 on April 17, aerosol extinctions calculated from the measured size distributions are systematically smaller than those derived from sunphotometer measurements. The discrepancy is probably a combined result of horizontally inhomogeneous aerosol layers during the spiral, which is shown by the large variation of scattering coefficients during level flight in free troposphere (Figure 5.18), and inaccurate interpretation of APS data. The aerosol extinction is also calculated assuming a doublet agglomerate shape as described in the previous case, and the calculated aerosol extinction in the mineral dust layer is presented in Figure 5.17. The data suggest that the discrepancy could potentially be explained by the shape of the

dust particles. The uncertainties in derived aerosol extinction are similar to those of Research Flight 11.

5.3.5 Summary of Measured and Calculated Aerosol Extinctions

Figure 5.19 shows measured and calculated aerosol extinctions over all four cases studied. (One data point near the surface during Research Flight 11 is excluded, where the aerosol extinction derived from AATS-14 measurement was probably corrupted as a result of horizontally inhomogeneous layers during the spiral.) The results show generally good agreement between aerosol extinction calculated from measured aerosol size distribution and chemical composition and those derived from sunphotometer measurements in boundary and pollution layers, where the slopes of the best fit are 0.96 and 1.03 at 525 nm and 0.94 and 1.04 at 1059 nm. For layers in the free troposphere, the slopes are 0.65 and 0.66 for 525 nm and 1059 nm, respectively. Possible reasons for underestimation of aerosol extinction from the size distribution data have been discussed above.

5.4 Summary

As part of the Aerosol Characterization Experiment-Asia from March to May 2001, aerosol size distributions were measured using differential mobility analyzer and aerodynamic particle sizer systems on-board the Twin Otter aircraft during 19 research flights. During the 19 missions, the atmosphere was often observed to be vertically layered, and a pollution layer with high aerosol extinction was frequently located between the boundary layer and free troposphere. Clear-column aerosol extinctions predicted using in situ aerosol size distribution and chemical composition

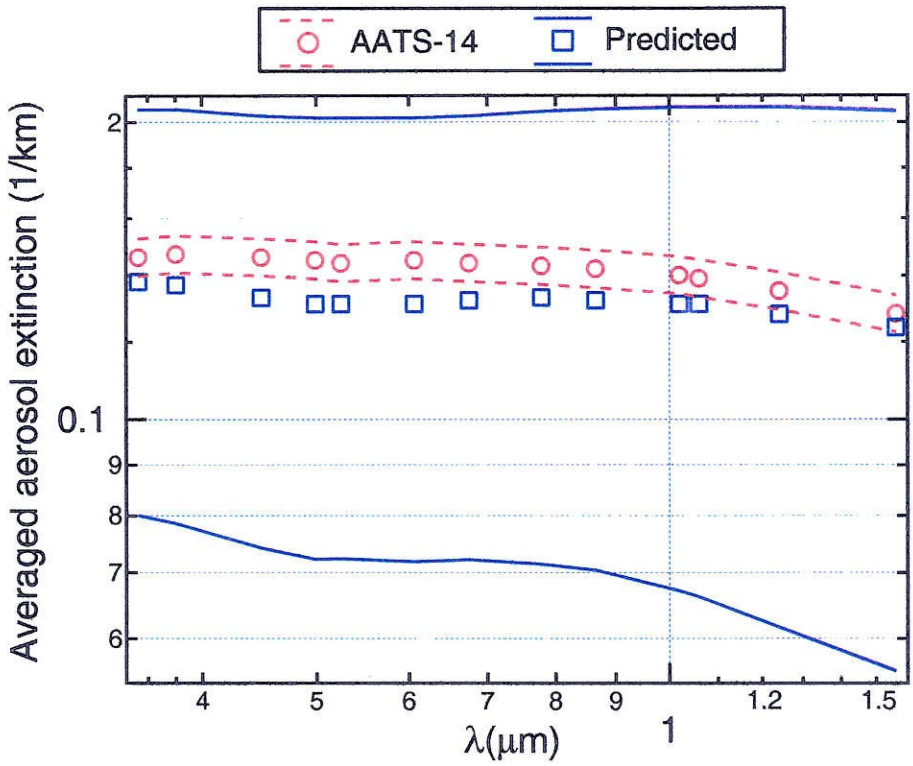

Figure 5.17: Aerosol extinctions averaged over the dust layer of Research Flight 9 on April 14, 2001. The calculation of aerosol extinction is based on a doublet agglomerate particle shape. The dashed and solid lines are the estimated uncertainties in measured and predicted extinctions, respectively.

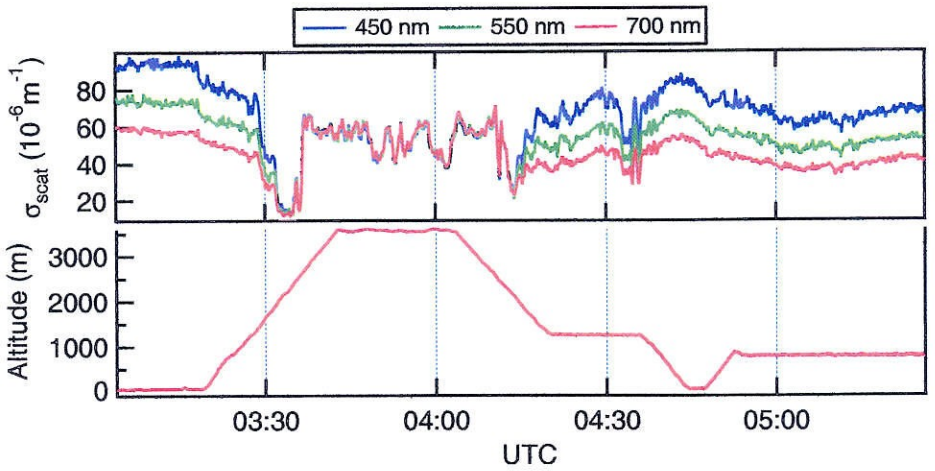

Figure 5.18: Scattering coefficients measured by on-board TSI 3-color nephelometer (model 3563) during Research Flight 9 on April 14, 2001. The wavelengths are 450 nm, 550 nm, and 700 nm.

measurements were compared to those derived from the 14-wavelength NASA Ames Airborne Tracking Sunphotometer (AATS-14). The uncertainties associated with predicted aerosol extinction are studied. In the boundary layer, pollution layers, and free troposphere with no significant mineral dust present, extinction closure was achieved within the estimated uncertainties over the full range of wavelengths of AATS-14. The aerosol extinctions predicted based on measured size distributions also reproduce the wavelength dependence derived from AATS-14 data. In free troposphere dust layers, the aerosol extinctions predicted from the measured size distributions were generally smaller than those derived from the AATS-14 data. The uncertainty analysis suggests that the discrepancy is likely a result of the lack of the knowledge of mineral dust shape, as well as variations in aerosol extinction derived from AATS-14 data when viewing through horizontally inhomogeneous layers. For all four research flights studied, the uncertainty in predicted aerosol extinction associated with the aerosol size and concentration measurement accuracy dominates the overall uncertainty except

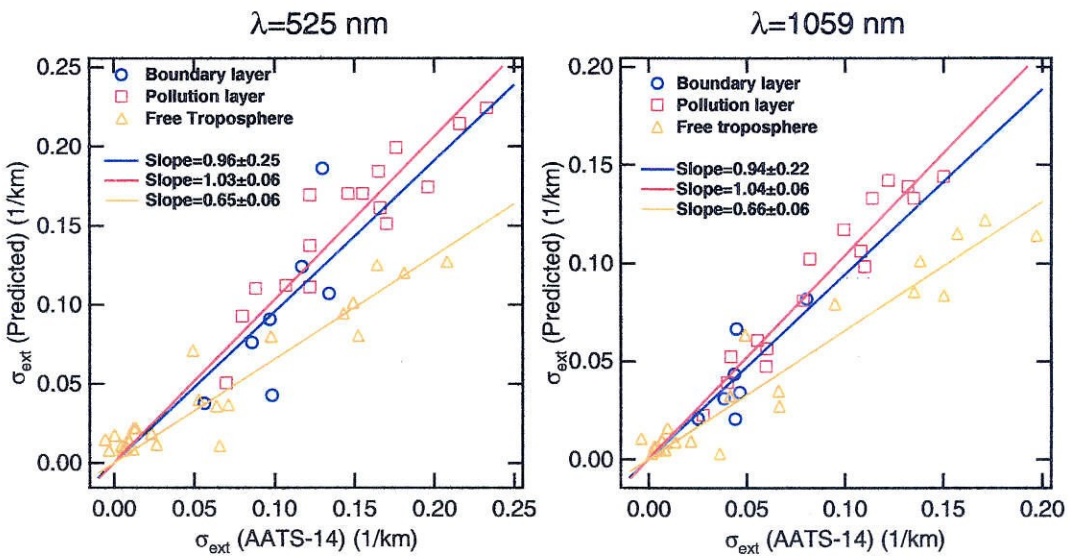

Figure 5.19: Comparison of measured and predicted aerosol extinctions and best-fit lines of calculation/measurement. The data are from the four flights analyzed.

in the dust layer, where the uncertainty introduced by lack of knowledge of dust density and shape becomes comparable. Considering all four cases, the best-fit lines yield predicted/observed ratios in boundary and pollution layers of 0.96 and 1.03 at $\lambda = 525$ nm, and 0.94 and 1.04 at $\lambda = 1059$ nm, respectively. For free tropospheric layers, the ratio is 0.65 and 0.66 at 525 nm and 1059 nm, respectively, when dust particles are modelled as spheres. A nonspherical model of dust (doublet agglomerates) can produce agreement between predicted and observed extinction, via the combined effect of larger APS-derived particle size and larger extinction-to-volume ratios.

Continued development of aerosol instruments, especially those capable of accurately characterizing the size and the shape of large particles, and size-resolved chemical composition will improve the ability to perform radiative closure of atmospheric aerosol.

5.5 Acknowledgement

We thank Brian Mader, Jose Jimenez, and Roya Bahreini for sharing their data. This work was supported by National Science Foundation Grant ATM-0001934, Office of Naval Research Grants N00014-96-1-0119 and N00014-01-F-0404, National Aeronautics and Space Administration Program Codes 622-44-75-10 and 291-01-91-45, and National Oceanographic and Atmospheric Administration Order NAO2AANRG0129.

Chapter 6

Conclusion

Predicting and mitigating the effect of aerosols require understanding of the spatial and temporal distributions as well as the source and governing processes of atmospheric aerosol. Due to the short lifetime of aerosol, its spatial and temporal distributions are highly nonuniform and variable, which can only be characterized through long-term and widespread measurements. In recent years, aircraft have increasingly been used to study atmospheric aerosols. The benefit of such an approach is obvious: spatially-resolved characterization of the aerosol over a large domain and the ability to probe the 3-dimensional distribution and vertical profile of aerosol properties that elude traditional ground and ship based measurements. However, aircraft-based measurements have inherent limitations. In addition to the obvious constraints on weight, space, and power, aircraft-based measurements must be more highly time-resolved than ground or ship based measurements, since even a one-minute measurement will represents an integration over several kilometers. Aircraft-based measurements also suffer from biases that result from modifications occurring in the sampling system that brings atmospheric aerosol to the instruments. While these bias are common to sampling from other platforms, they are often times more extreme for aircraft-based measurements.

The development of the fast response mixing condensation nucleus counter (MCNC) significantly increases the speed of submicron aerosol size distribution measurements. Differential mobility analyzers (DMA) coupled with developed MCNC can measure submicron aerosol size distribution in as little as 2 s, which corresponds to a spatial resolution of 100 m for aircraft-based measurements. To reduce the artifacts associated with the difference between the ambient relative humidity (RH) and those inside the instruments, the first airborne DMA system that measures aerosol size distributions at ambient RH has been developed. The RH of the aerosol sample is controlled through an active RH controller, which adds or removes water vapor from the aerosol sample to compensate the RH change resulting from the ram heating and

heat transfer between aerosol sample flow and the duct surrounding it. While these developments have significantly improved the temporal and spatial resolution, and the accuracy of the aircraft-based size distribution measurements, there still exists potentials for improvement. One of them is the counting statistics of size distribution measurements. While the fast response MCNC enables measurements as fast as 2 s, the low atmospheric aerosol concentration (e.g., unpolluted marine boundary layer) often requires average of many fast measurements to achieve statistically significant results. The approach to increase the measurement counting statistics can be based on either improvement of the sample flow rates of both DMA and MCNC or development of an aerosol charger with higher charging efficiencies.

Radiative closure analysis was performed using the data from ACE-Asia. In the marine boundary layer, pollution layer, and free troposphere with no significant dust present, closure was achieved, and the discrepancies between predicted and measured aerosol extinction were largely within the estimated uncertainties. For the free troposphere with significant dust, the aerosol extinctions predicted from in situ size distributions were smaller than those derived from simultaneous sunphotometer measurements. Uncertainty analysis indicated the underestimation of aerosol extinction in the dust layer was likely a result of the lack of the dust shape information and the uncertainty in APS measurement of nonspherical dust size distributions. Future closure studies can be improved by the development of instruments capable of accurate characterization of size, concentration, and shape of large particles. The development of instrumentation for size-resolved chemical composition measurements will further reduce the uncertainty in calculated aerosol extinctions. In addition to aerosol extinction, closure studies of other aerosol radiative properties, such as the radiative forcing at top of the atmosphere, will be necessary to further assess the ability of models to predict aerosol climate effects.

Bibliography

[1] M. Alonso, Y. Kousaka, T. Hashimoto, and N. Hashimoto. Penetration of nanometer-sized aerosol particles through wire screen and laminar flow tube. *Aerosol Sci. Technol.*, 27(4):471–480, 1997.

[2] A. J. Armendariz and D. Leith. Concentration measurement and counting efficiency for the aerodynamic particle sizer 3320. *J. Aerosol Sci.*, 33(1):133–148, 2002.

[3] R. Bahreini, J. L. Jimenez, Flagan R. C., J. H. Seinfeld, J. T. Jayne, and D. R. Worsnop. Aircraft-based aerosol size and composition measurements during ACE-Asia using an aerodyne aerosol mass spectrometer. *J. Geophys. Res.*, 2002.

[4] P. A. Baron. *Aerosols.* (B. Y. H. Liu, D. Y. H. Pui, and H. J. Fissan, eds.), Elsevier, New York, 1984.

[5] H. Bartz, H. Fissan, and B. Y. H. Liu. A new generator for ultrafine aerosols below 10 nm. *Aerosol Sci. Technol.*, 6(2):163–171, 1987.

[6] R. T. Bluth, P. A. Durkee, J. H. Seinfeld, R. C. Flagan, L. M. Russell, P. A. Crowley, and P. Finn. Center for interdisciplinary remotely piloted aircraft studies (CIRPAS). *B. Am. Meterolo. Soc.*, 77(11):2691–2699, (1996).

[7] C. A. Brock, L. F. Radke, J. H. Lyons, and P. V. Hobbs. Arctic hazes in summer over Greenland and the North-American arctic. 1. Incidence and origins. *J. Atmos. Chem.*, 9(1-3):129–148, (1989).

[8] D. A. G. Bruggeman. Berechnung verschiedener physikalischer Konstanten von heterogenen Substanzen. I. Dielektrizitätskonstanten und Leitfähigkeiten der Mischkörper aus isotropen Substanzen. *Ann. Phys. (Leipzig)*, 24:636–679, 1935.

[9] R. Y. Chen and R. A. Comparin. Deposition of aerosols in the entrance of a tube. *J. Aerosol Sci.*, 7:335–341, 1976.

[10] Y. S. Cheng, B. T. Chen, and H. C. Yeh. Behavior of isometric nonspherical aerosol particles in the aerodynamic particle sizer. *J. Aerosol Sci.*, 21(5):701–710, 1990.

[11] Y. S. Cheng, B. T. Chen, H. C. Yeh, I. A. Marshall, J. P. Mitchell, and W. D. Griffiths. Behavior of compact nonspherical particles in the TSI aerodynamic particle sizer model APS33B — Ultra-stokesian drag forces. *Aerosol Sci. Technol.*, 19(3):255–267, 1993.

[12] J.C. Choi, M. Lee, Y. Chun, J. Kim, and S. Oh. Chemical composition and source signature of spring aerosol in Seoul, Korea. *J. Geophys. Res.*, 106(D16):18067–18074, 2001.

[13] P. Chylek, V. Srivastava, R.G. Pinnick, and R.T. Wang. Scattering of electromagnetic waves by composite spherical particles — Experiment and effective medium approximations. *Appl. Opt.*, 27(12):2396–2404, 1988.

[14] A. D. Clarke, J. N. Porter, F. P. J. Valero, and P. Pilewskie. Vertical profiles, aerosol microphysics, and optical closure during the Atlantic Stratocumulus Transition Experiment: Measured and modeled column optical properties. *J. Geophys. Res.*, 101(D2):4443–4453, 1996.

[15] D. R. Collins. *Characterization of the physical properties of atmospheric aerosol through airborne sampling.* Ph.D. thesis, California Institute of Technology, 2000.

[16] D. R. Collins, R. C. Flagan, and J. H. Seinfeld. Improved inversion of scanning DMA data. *Aerosol Sci. Technol.*, 36(1):1–9, 2002a.

[17] D. R. Collins, H. H. Jonsson, J. H. Seinfeld, R. C. Flagan, S. Gasso, D. A. Hegg, P. B. Russell, B. Schmid, J. M. Livingston, E. Ostrom, K. J. Noone, L. M. Russell, and J. P. Putaud. In situ aerosol-size distributions and clear-column radiative closure during ACE-2. *Tellus*, 52B(2):498–525, 2000.

[18] Collins, D., et al. Aerosol hygroscopic property closure during ACE-Asia. *J. Geophys. Res.*, 2002b.

[19] S. Corrsin. A simple theory for a turbulent mixer. *A.I.Ch.E.J.*, 3:329–331, 1957.

[20] CRC. *Handbook of Chemistry and Physics.* CRC Press, Cleveland, Ohio, 1970.

[21] A. J. Ede. The effect of a right-angled bend on heat transfer in a pipe. *Int. Dev. Heat Transfer*, pages 634–642, 1961.

[22] K. A. Fuller, W. C. Malm, and S. M. Kreidenweis. Effects of mixing on extinction by carbonaceous particles. *J. Geophys. Res.*, 104(D13):15941–15954, 1999.

[23] M. Gamero-Castaño and J.F. de la Mora. A condensation nucleus counter (CNC) sensitive to singly charged subnanometer particles. *J. Aerosol Sci.*, 31:757–772, 2000.

[24] Gao, S., et al. Airborne measurements of chemical species during ACE-Asia: Their identification and spatial distribution. *J. Geophys. Res.*, 2002.

[25] P. G. Gormley and M. Kennedy. Diffusion from a stream flowing through a cylindrical tube. *Proceedings of the Royal Irish Academy*, 52A:163–169, 1949.

[26] W. D. Griffiths, P.J. Iles, and N. P. Vaughan. The behavior of liquid droplet aerosols in an APS- 3300. *J. Aerosol Sci.*, 17(6):921–930, 1986.

[27] K. B. He, F. M. Yang, Y. L. Ma, Q. Zhang, X. H. Yao, C. K. Chan, S. Cadle, T. Chan, and P. Mulawa. The characteristics of PM2.5 in Beijing, China. *Atmos. Environ.*, 35(29):4959–4970, 2001.

[28] D. A. Hegg, R. J. Ferek, and P. V. Hobbs. Aerosol size distributions in the cloudy atmospheric boundary-layer of the North-Atlantic ocean. *J. Geophys. Res.*, 98(D5):8841–8846, (1993).

[29] D. A. Hegg, J. Livingston, P. V. Hobbs, T. Novakov, and P. Russell. Chemical apportionment of acrosol column optical depth off the mid-Atlantic coast of the United States. *J. Geophys. Res.*, 102(D21):25293–25303, 1997.

[30] R. M. Hoff, L. GuiseBagley, R. M. Staebler, H. A. Wiebe, J. Brook, B. Georgi, and T. Dusterdiek. Lidar, nephelometer, and in situ aerosol experiments in southern Ontario. *J. Geophys. Res.*, 101(D14):19199–19209, 1996.

[31] S. G. Howell and B. J. Huebert. Determining marine aerosol scattering characteristics at ambient humidity from size-resolved chemical composition. *J. Geophys. Res.*, 103(D1):1391–1404, 1998.

[32] J. G. Hudson and A. D. Clarke. Aerosol and cloud condensation nuclei measurements in the Kuwait plume. *J. Geophys. Res.*, 97(D13):14533–14536, (1992).

[33] Huebert B., et al. The Aerosol Characterization Experiment-Asia (ACE-Asia). *J. Geophys. Res.*, 2002.

[34] J. A. C. Humphrey, H. Iacovides, and B. E. Launder. Some numerical experiments on developing laminar flow in circular-sectioned bends. *J. Fluid Mech.*, 154:357–376, 1985.

[35] F. P. Incropera and D. P. DeWitt. *Fundamentals of Heat and Mass Transfer.* John Wiley & Sons, 1996

[36] D. B. Ingham. Diffusion of aerosols from a stream flowing through a cylindrical tube. *J.Aerosol Sci.*, 6:125–132, 1975.

[37] W. M. Kays and M. E. Crawford. *Convective Heat and Mass Transfer.* McGraw-Hill, New York, 1980.

[38] J. Kesten, A. Reineking, and J. Porstendorfer. Calibration of a TSI model 3025 condensation particle counter. *Aerosol Sci. Technol.*, 15:107–111, 1991.

[39] Y. P. Kim, J. H. Lee, N. J. Baik, J. Y. Kim, S. G. Shim, and C. H. Kang. Summertime characteristics of aerosol composition at Cheju Island, Korea. *Atmos. Environ.*, 32(22):3905–3915, 1998.

[40] P. D. Kinney and D. Y. H. Pui. Inlet efficiency study for the TSI aerodynamic particle sizer. *Particle and Particle Systems Characterization*, 12(4):188–193, 1995.

[41] Y. I. Kogan and Burnasheva Z. A. Growth and measurement of condensation nuclei in a continuous stream. *Rus. J. Phys. Chem.*, 34:1240–1243, 1960.

[42] Y. Kousaka, T. Niida, K. Okuyama, and H. Tanaka. Development of a mixing type condensation nucleus counter. *J. Aerosol Sci.*, 13(3):231–240, 1982.

[43] Y. Kousaka, K. Okuyama, and M. Adachi. Determination of particle-size distribution of ultrafine aerosols using a differential mobility analyzer. *Aerosol Sci. Technol.*, 4(2):209–225, 1985.

[44] S. M. Larson, G. R. Cass, K. J. Hussey, and F. Luce. Verification of image-processing based visibility models. *Environ. Sci. Technol.*, 22(6):629–637, 1988.

[45] B. T. Mader, R. C. Flagan, and J. H. Seinfeld. Aircraft measurements of atmospheric carbonaceous aerosols during ACE-Asia. *J. Geophys. Res.*, Submitted, 2002.

[46] N. D. Mehta and K. J. Bell. Laminar flow heat transfer in a tube preceded by a 180° bend. *Heat Transfer—Soviet Research*, 13(6):71–80, 1981.

[47] S. Mertes, F. Schroder, and A. Wiedensohler. The particle-detection efficiency curve of the TSI-3010 CPC as a function of the temperature difference between saturator and condenser. *Aerosol Sci. Technol.*, 23:257–261, 1995.

[48] M. I. Mishchenko, L. D. Travis, R. A. Kahn, and R. A. West. Modeling phase functions for dustlike tropospheric aerosols using a shape mixture of randomly oriented polydisperse spheroids. *J. Geophys. Res.*, 102(D14):16831–16847, 1997.

[49] E. A. Moelwyn-Hughes. *Physical Chemistry.* Pergamon, New York, 1961.

[50] A. Nenes, S. N. Pandis, and C. Pilinis. ISORROPIA: A new thermodynamic equilibrium model for multiphase multicomponent inorganic aerosols. *Aquat. Geochem.*, 4(1):123–152, 1998.

[51] K. Okuyama, Y. Kousaka, and T. Motouchi. Condensational growth of ultrafine aerosol particles in a new particle-size magnifier. *Aerosol Sci. Technol.*, 3(4):353–366, 1984.

[52] R. Paul and S. J. Paddison. A statistical mechanical model for the calculation of the permittivity of water in hydrated polymer electrolyte membrane pores. *J Chem. Phys.*, 115(16):7762–7771, 2001.

[53] D. Y. H. Pui, F. Romay-Novas, and B. Y. H. Liu. Experimental study of particle deposition in bends of circular cross section. *Aerosol Sci. Technol.*, 7:301–315, 1987.

[54] F. R. Quant, R. Caldow, G. J. Sem, and Addison T. J. Performance of condensation particle counters with three continuous-flow designs. *J. Aerosol Sci.*, 23:S405–S408, 1992.

[55] J. Redemann, R. P. Turco, R. F. Pueschel, M. A. Fenn, E. V. Browell, and W. B. Grant. A multi-instrument approach for characterizing the vertical structure of aerosol properties: Case studies in the Pacific Basin troposphere. *J. Geophys. Res.*, 103(D18):23287–23298, 1998.

[56] L. M. Russell. *The physics and chemistry of marine aerosols.* Ph.D. thesis, California Institute of Technology, 1995.

[57] L. M. Russell, R. C. Flagan, and J. H. Seinfeld. Asymmetric instrument response resulting from mixing effects in accelerated dma-cpc measurements. *Aerosol Sci. Technol.*, 23(4):491–509, 1995.

[58] L. M. Russell, S. H. Zhang, R. C. Flagan, J. H. Seinfeld, M. R. Stolzenburg, and R. Caldow. Radially classified aerosol detector for aircraft-based submicron aerosol measurements. *J. Atmos. Ocean Technol.*, 13(3):598–609, (1996).

[59] P. B. Russell, J. M. Livingston, P. Hignett, S. Kinne, J. Wong, A. Chien, R. Bergstrom, P. Durkee, and P. V. Hobbs. Aerosol-induced radiative flux changes off the United States mid-Atlantic coast: Comparison of values calculated from sunphotometer and in situ data with those measured by airborne pyranometer. *J. Geophys. Res.*, 104(D2):2289–2307, 1999.

[60] P. Saxena, L. M. Hildemann, P. H. McMurry, and J. H. Seinfeld. Organics alter hygroscopic behavior of atmospheric particles. *J. Geophys. Res.*, 100(D9):18755–18770, 1995.

[61] B. Schmid, J. M. Livingston, P. B. Russell, P. A. Durkee, H. H. Jonsson, D. R. Collins, R. C. Flagan, J. H. Seinfeld, S. Gasso, D. A. Hegg, E. Ostrom, K. J. Noone, E. J. Welton, K. J. Voss, H. R. Gordon, P. Formenti, and M. O. Andreae. Clear-sky closure studies of lower tropospheric aerosol and water vapor during ACE-2 using airborne sunphotometer, airborne in-situ, space-borne, and ground-based measurements. *Tellus*, 52B(2):568–593, 2000.

[62] B. Schmid, J. Redemann, P. B. Russell, P. V Hobbs, D. L. Hlavka, M. J. McGill, B. N. Holben, E. J. Welton, J. Campbell, O. Torres, R. A. Kahn, D. J. Diner, M. C. Helmlinger, D. A. Chu, C. Robles Gonzalez, and G. de Leeuw. Coordinated airborne, spaceborne, and ground-based measurements of massive, thick aerosol layers during the dry season in Southern Africa. *J. Geophys. Res.*, Submitted, 2002.

[63] S. Schwyn, E. Garwin, and A. Schmidt-Ott. Aerosol generation by spark discharge. *J. Aerosol Sci.*, 19:639–642, 1988.

[64] J. H. Seinfeld and S. N. Pandis. *Atmospheric chemistry and physics.* Wiley-Interscience, New York, 1998.

[65] J. R. Sellars, M. Tribus, and J. S. Klein. Heat transfer to laminar flow in a round tube or flat conduit—the graetz problem extended. *Trans. ASME*, 78:441–448, 1956.

[66] T. Seto, K. Okuyama, L. de Juan, and J. F. de la mora. Condensation of supersaturated vapors on monovalent and divalent ions on varying size. *J. Chem. Phys.*, 107(5):1576–1585, 1997.

[67] I. Sokolik, A. Andronova, and T. C. Johnson. Complex refractive-index of atmospheric dust aerosols. *Atmos. Environ.*, 27A(16):2495–2502, 1993.

[68] M. R. Stolzenburg and P. H. McMurray. In ultrafine aerosol condensation nucleus counter. *Aerosol Sci. Technol.*, 14(1):48–65, 1991.

[69] C. W. Tan and C. J. Hsu. Diffusion of aerosols in laminar flow in a cylindrical tube. *J. Aerosol Sci.*, 2:117–124, 1971.

[70] I. N. Tang. Chemical and size effects of hygroscopic aerosols on light scattering coefficients. *J. Geophys. Res.*, 101(D14):19245–19250, 1996.

[71] I. N. Tang and H. R. Munkelwitz. Water activities, densities, and refractive-indexes of aqueous sulfates and sodium-nitrate droplets of atmospheric importance. *J. Geophys. Res.*, 99(D9):18801–18808, 1994.

[72] I. N. Tang, A. C. Tridico, and K. H. Fung. Thermodynamic and optical properties of sea salt aerosols. *J. Geophys. Res.*, 102(D19):23269–23275, 1997.

[73] C. J. Tsai and D. Y. H. Pui. Numerical study of particle deposition in bends of a circular cross-section laminar flow regime. *Aerosol. Sci. Technol.*, 12:813–831, 1990.

[74] B. J. Turpin and H. J. Lim. Species contributions to PM2.5 mass concentrations: Revisiting common assumptions for estimating organic mass. *Aerosol Sci. Technol.*, 35(1):602–610, 2001.

[75] G. Videen and P. Chylek. Scattering by a composite sphere with an absorbing inclusion and effective medium approximations. *Opt. Commun*, 158(1-6):1–6, 1998.

[76] F. E. Volz. Infrared optical constants of ammonium sulfate, sahara dust, volcanic pumice and flyash. *Appl. Opt.*, 12(3):564–568, 1973.

[77] H. C. Wang and W. John. Particle density correction for the aerodynamic particle sizer. *Aerosol Sci. Technol.*, 6(2):191–198, 1987.

[78] J. Wang, R. C. Flagan, and J. H. Seinfeld. A differential mobility analyzer (DMA) system for submicron aerosol measurements at ambient relative humidity. *Aerosol Sci. Technol.*, In press, 2002.

[79] S. C. Wang and R. C. Flagan. Scanning electrical mobility spectrometer. *J. Aerosol Sci.*, 20(8):1485–1488, (1989).

[80] J. C. Wilson and B. Y. H. Liu. Aerodynamic particle-size measurement by laser-doppler velocimetry. *J. Aersol Sci.*, 11(2):139–150, 1980.

[81] S. H. Zhang, Y. Akutsu, L. M. Russell, R. C. Flagan, and J. H. Seinfeld. Radial differential mobility analyzer. *Aerosol Sci. Technol.*, 23(3):357–372, 1995.